TRENDS IN GEOMETRY AND ENERGY OF METAL AND METAL OXIDE CLUSTERS CALCULATED BY DENSITY FUNCTIONAL THEORY

HARNEET KAUR DHILLON,

A DISSERTATION SUBMITTED TO THE FACULTY OF GRADUATE STUDIES IN PARTIAL FULFILMENT OF THE REQUIREMENTS FOR THE DEGREE OF

DOCTOR OF PHILOSOPHY

GRADUATE PROGRAM IN PHYSICS AND ASTRONOMY

YORK UNIVERSITY

TORONTO, ONTARIO

JANUARY 2020

Abstract

We have studied the structural and electronic properties for different groups of atomic clusters by doing a global search on the potential energy surface using a modified version of the Tabu search in descriptor space method. The geometry optimizations and calculation of energies were carried out using Density Functional Theory implemented in the Gaussian 09 and Gaussian 16 software.

For Ag_n, $(n = 4 - 20)$, Ag_nCl_2, $(n = 3 - 10, 12)$ and Ag_nHg_m, $(n = 5, 6$ and $m = 1 - 4)$ clusters, we have found that the change from planar to 3 dimensional geometry occurs at cluster size $n > 6$. Binding of Cl atoms to Ag atoms causes greater distortion in shape as compared to binding of Hg atoms to Ag atoms. For Li, Mg, Al clusters, we studied 130 binary and ternary clusters such that A_mB_n $(5 \leq m+n \leq 8)$ with A,B = Li,Mg,Al and $A_pB_qC_r$ $(5 \leq p + q + r \leq 8)$, with A,B,C = Li,Mg,Al. We analyzed trends in atomization energies with a sequence of linear regressions of increasing complexity. For Al_xO_y, $(x + y < 17)$ clusters, the most stable cluster is non-stoichiometric$(x/y \neq 2/3)$; Al_6O_8. Analysis of relative stability and energies of reaction for Al_xO_y clusters suggests that non-stoichiometry could play a role in early stages of growth of group 13 oxides. The structures for most stable clusters for Si_xO_y,

$(x = 1 - 4)$, $(y = 2x, 2x \pm 1)$ and Si_3O_y,$(y = 1 - 9)$ clusters are diverse and do not follow a simple growth principle. We analyzed the geometry, asphericity and shape descriptors for metal oxides (M_xO_y) such that $(x + y \leq 12)$, where M= Li, Mg, K, Zn, Cu, Ag, Si, and Al. This analysis suggests a preference for prolate geometries for $(SiO)_n$ clusters, oblate geometries for $(ZnO)_n$ clusters and no obvious pattern in shape for all other clusters. In every case, the favored structures have very few M-M bonds and O-O bonds.

Acknowlegdements

I would like to express my sincere gratitude to my supervisor, Professor René Fournier for the continuous support of my Ph.D study and related research, for his patience, motivation, and immense knowledge. I will always be thankful for his wisdom, knowledge, especially for his clear, pedagogical and detailed explanations which have developed in me a deeper appreciation for the beauty of computational chemical physics. His guidance helped me in all the time of research and writing of this thesis. I could not have imagined having a better supervisor and mentor for my Ph.D study.

I also would like to thank my supervisory committee: Prof. Tom Kirchner and Prof. Marko Horbatsch, for their insightful comments and encouragement, for their detailed and constructive comments about my research which incented me to widen my research from various perspectives.

Last but not the least, I would like to thank my family: my in-laws and my parents for supporting me throughout my Ph.D and writing this thesis. My special thanks goes to my husband for his unconditional support and encouragement and without whose support, this work would have simply been not possible. I would like to dedicate this dissertation to my husband Jag and my daughter Amreen.

This work was made possible by the facilities of the Shared Hierarchical Academic Research Computing Network (SHARCNET: www.sharcnet.ca) and funding by the Natural Sciences and Engineering Research Council of Canada

List of Acronyms

AE	Atomization energy
AEA	Adiabatic electron affinity
B3LYP	Three parameter Becke, Lee-Yang-Parr exchange correlation
BPW91	Becke, Perdew-Wang 1991
DE	Dissociation energy
DFT	Density functional theory
EA	Electron affinity
EJM	Ellipsoidal jellium model
FCC	Face centred cubic
GGA	Generalized gradient approximation
GM	Global minimum
HOMO	Highest occupied molecular orbital
HCP	Hexagonal close packing

HK	Hohenberg-Kohn
IP	Ionization potential
KS DFT	Kohn-Sham Density Functional theory
LUMO	Lowest unoccupied molecular orbital
LDA	Local density approximation
LJ	Lennard -Jones
LSDA	Local spin density approximation
LANL2DZ	Los Alamos National laboratory 2-double-z (density functional theory)
MHP	Maximum hardness principle
NBO	Natural bond orbital
PES	Photoelectron spectroscopy
PBE	Perdew-Burke-Ernzerhof
PBP	Pentagonal bipyramid
PES	Photoelectron spectroscopy
RITS	Relative Index of thermodynamic stability
RMSD	Root Mean square deviation
TSDS	Tabu search in descriptor space
VEA	Vertical electron affinity

VIP	Vertical ionization potential
VASP	Vienna ab-initio simulation package
VSEPR	Valence shell electron pair repulsion theory
VWN	Vosko-Wilk-Nusair
XC	Exchange correlation

List of Tables

List of Figures

Contents

Chapter 1

Introduction

1.1 Clusters

Clusters are aggregates of atoms and molecules ranging in size from two to tens of thousands of monomer units. They can be formed by interactions ranging from very weak Van der Waals contacts to strong ionic or covalent bonds. An n-monomer cluster "M_n" has the same properties as the bulk solid when n is huge ($n \gtrsim 10^6$). But when $n \lesssim 100$, clusters often display properties different from those of bulk materials in structural, electronic and magnetic aspects [1, 2]. For example, clusters of nonmagnetic elements may be magnetic [3, 4], semiconducting materials may exhibit metallic properties and the color may change with size. This is because clusters have a large fraction of atoms on the surface while that fraction is negligible in case of a macroscopic solid. For example, Table 1.1 shows the fraction of atoms on surface 'f_{surface}' for n^{th} shell of quasi-spherical clusters, using Mackay's icosahedral shell model [5]. The number of atoms N_a is a function of number of complete atomic shells

K: $N_a\ (K) = \ (10/3)K^3 - 5K^2 + \ (11/3)K - 1$; $K \geq 1$. The fraction of atoms at the surface of a K-shell cluster is $f_{\text{surface}} = 1 - N_a\ (K-1)/N_a\ (K)$.

Table 1.1: Surface atoms

K	N_a	f_{surface}
2	13	92%
3	55	76%
4	147	63%
5	309	52%
10	2869	28%
50	404349	6%
100	3283699	3%
860	2116491776	0.3%

Also, the energy gap between the highest occupied molecular orbital (HOMO) and the lowest unoccupied molecular orbital (LUMO) varies with cluster size. The way these orbitals are filled determines to some extent the stability and properties of the clusters [5, 6]. The magnitude of the HOMO-LUMO gap varies with both composition and size of cluster and is one of many indicators of stability of the cluster. These properties make clusters particularly interesting from both the theoretical and practical viewpoints. For example, clusters with very special stability and structure

have inspired the search for new materials. C_{60} and other fullerenes, in particular, led to carbon nanotubes [7] and sparked interest in the search for clusters with cage-like structures [8, 9, 10].

Clusters with high stability are particularly interesting because they could potentially be made in large quantities and used as building blocks for new materials [11, 12, 13]. The concept of *superatom*, first proposed by Khanna and Jena [14], is attractive. A superatom is any sufficiently stable, high-symmetry, quasi-spherical cluster whose valence electron count, ionization energy, and electron affinity, mimic those of a ground - state atom of some element. If it can be synthesized, such a cluster could be viewed as a new man-made element. Khanna and Jena suggested that superatoms could be arranged into a kind of three dimensional periodic table, where cluster size "n" is the third dimension. If the superatoms themselves are stable, their physics and chemistry should follow the trends of elements in the corresponding column of the periodic table. Some of the examples of superatoms are $W@Au_{12}$ predicted by Pykkö and Runeberg [15], Al_{13} [16], Li_3O [17] and $M@Si_{16}$ [18, 19, 20, 21, 22].

The jellium model of metal cluster electronic structure (explained in chapter 3) predicts shell closings, and relative stability, when the valence electron count is $2, 8, 20, 34, 40, 54 \ldots$. These clusters are relatively stable within their respective series. But the vast majority of magic clusters are not truly stable. They will react or coalesce under normal conditions and cannot be isolated or used in chemical synthesis. However, their studies could help find stability criteria. In addition to the 'magic clusters', intensity distribution of metallic clusters by Knight *et al.* [23] showed that clusters with even number of electrons are more stable than the clusters with odd

number of atoms [23]. Some energy variations cannot be explained by the spherical jellium model and this suggests that the geometries of clusters do not conform to the simple jellium model and may be deformed. Although the jellium model has been very successful in explaining the stability of clusters of free electron metals, it could not account for the structural properties of clusters, such as their geometry and atomic arrangements. To get such information, exhaustive molecular based calculations relying on quantum-chemical and density-functional techniques are necesssary [24]. In such calculations both the electronic and nuclear degrees of freedom are taken into account.

Electronic structure of clusters and properties such as binding energies, ionization potentials, magnetic moments and chemical reactivities etc. have been measured experimentally. Gas phase molecular clusters are generated by pulsed supersonic jet expansion techniques [25, 26, 27, 28]. A dilute mixture of gas under study is mixed with an inert gas and is allowed to expand through a slit-jet source, forming clusters of variable sizes. This gas expansion can be combined with a variety of experimental techniques, such as infrared (IR), microwave (MW), and photoelectron spectroscopy for probing the molecular clusters. IR spectroscopy is used to study the vibrational modes [29]. IR absorption occurs when the frequency of the IR beam is the same as a normal mode vibrational frequency of the cluster. These resonant frequencies depend on a number of factors such as geometry of molecules and masses of atoms, etc. By comparing the experimental IR spectrum with the calculated one, the geometric structure can be assigned. IR spectroscopy can provide information on the geometry of neutral as well as charged clusters. In many studies, IR spectroscopy combined

with density functional theory (DFT) has been used to determine the preferred geometry of monoatomic and heteroatomic clusters. Recently, Truong *et al.* [30] studied the structure of Si_nB_m $(n = 3-8, m = 1-2)$ clusters. Meijer and coworkers [31] studied the structures of neutral Nb_n $(n = 5-20)$ clusters, charged Tb_n^+ $(n = 5-9)$ clusters [32] and hydrated bisulphate anion clusters HSO_4^- $(H_2O)_{1-16}$ [33]. Bakker *et al.* [34] studied C_{60}, neutral and cationic niobium clusters [35], and the ferrimagnetic cage-like Fe_4O_6 cluster [36].

Photoelectron spectroscopies is very useful to provide information on the geometry of anions [37, 38, 39]. The material irradiated with ultraviolet light or X rays can emit electrons called the photoelectrons. The binding energy of the photoelectron is the energy difference between its measured kinetic energy and the photon energy. Any change in the geometry following electron ejection can be inferred by studying the sharpness of the photoemission peaks.

Gas phase ion mobility measurements provide geometric information about molecular ions in the gas phase [40]. It involves the measurement of the time taken by an ion to drift through a gas-filled cell guided by a static electrical field. For ions of a given mass, larger clusters have larger collision cross sections, thus their drift time is longer than for the more compact ions. This cross section allows one to determine the structures of cluster ions by comparing to cross-section predictions from theory.

Trapped ion electron diffraction techniques enable structural determination through comparison to trial structures derived from theory [41, 42, 43, 44]. The cluster ions are generated and injected into a quadrupole ion trap for mass selection and thermalization. These trapped ions are then irradiated with an electron beam. The resulting

diffraction pattern is integrated with an external charge-coupled device detector, followed by comparison to a theoretically simulated scattering function.

Magnetic properties of clusters are determined by Stern-Gerlach deflection experiments. Clusters interact with an applied inhomogenous magnetic field and are deflected from the original trajectory, this deflection reveals the cluster magnetization [45, 46].

Knowledge of the geometric structure of clusters is needed in order to make sense of the observed properties. However, determining cluster geometries from theory is a nontrivial task. This is due to the fact that the number of isomers increases exponentially with cluster size [47]. For a cluster with N atoms, the potential energy surface, as a function of position of these N atoms will have thousands or even millions of possible local minima when $N > 20$. Amongst these local minima, the global minimum corresponds to the ground state geometry of the cluster. Thus a reliable and efficient method is needed to do a global search among configurations and minimize the total energy. The next section will outline the goals of our study and methods we used for global optimization.

1.2 Goals and Computational methods

Our focus is on finding and quantifying trends among a very large number of computational results obtained by a combination of DFT electronic structure calculations and global optimization for different series of metal clusters and metal oxide clusters. We studied Ag_n without and with adsorbed Cl and Hg atoms; bi- and tri-metallic

clusters of Li, Mg and Al; stoichiometric oxides of Li, Mg, K, Zn, and K; and stoichiometric and non-stoichiometric oxides of Al, Si, Ag and Cu (Ag_n with Cl and Hg, $Li_xMg_yAl_z$, Al_xO_y, and $MO_x, M = Si, Zn, Mg, Ag, Cu$).

For global optimizations, we used the Taboo search in descriptor space (TSDS) and a modified version of TSDS [48], where all energies are calculated by first principles Kohn-Sham Density functional theory (KS-DFT) implemented in programs like Gaussian09 [49] and Gaussian16 [50]. TSDS performs many cycles for calculating the global energy minimum structure of atomic clusters. In each cycle TSDS generates many cluster structures randomly and modifies them by symmetrization of interatomic distances. The structural descriptors are then calculated for these clusters. Clusters are then screened according to a model energy obtained by interpolation over descriptor space. Only one best cluster is retained for energy evaluation. This cycle is repeated many times and clusters are arranged in increasing order. Local optimization is then performed for 15 or 20 lowest energy clusters obtained by TSDS. In modified version of TSDS, the clusters are ranked in order of increasing value of an objective function obtained by a combination of measure of relative thermodynamic stability and a property of interest (details in chapter 4).

These clusters have been analyzed using various descriptors of stability and structure. The stability descriptors we used include: a Relative Index of thermodynamic stability, RITS (thermodynamic stability); HOMO-LUMO gap, ionization energy and electron affinity (electronic stability); and vibrational frequencies (mechanical stability). The structural descriptors we used include: asphericity and shape defined as simple functions of the moments of inertia; compactness; strain (fluctuation in

the values of nearest neighbor distances); and mixing (a function of the numbers of AA, BB and AB nearest neighbors in a A_xB_y cluster). When comparing with experimental results, we study the balance between competing structural principles during the formation of different groups of global minima, which illustrate the trends in cluster structure and properties.

Chapter 2

Kohn-Sham Density Functional Theory

2.1 Density Functional theory (DFT)

DFT is perhaps the most popular approach for electronic structure calculations. It gives a good compromise between computational cost and accuracy. The most important quantity in DFT is the electron density $\rho(\vec{r})$. A key element of DFT is the functional connecting electron density with energy [51]. The term 'functional' means 'function of a function'. A *functional* is a rule for going from function to a number. For example, $\int_0^{2\pi} dx$ is a functional defined when acting on functions of x that are well behaved in $x = [0, 2\pi]$. In pure DFT, all properties are expressed in terms of functionals of $\rho(\vec{r})$. In general, one only needs the knowledge of the electron density to calculate the ground - state energy of a system.

The following is an overview of Density Functional theory [53, 54]

The nonrelativistic Hamiltonian for a molecule, in atomic units, is :

$$\hat{H}_m = \sum_{i=1}^{N} \frac{-1}{2} \nabla_i^2 + \sum_{\alpha=1}^{M} \frac{-1}{2m_\alpha} \nabla_\alpha^2 + \sum_{i=2}^{N} \sum_{j=1}^{i-1} \frac{1}{|\vec{r_i} - \vec{r_j}|} + \sum_{\alpha=2}^{M} \sum_{\beta=1}^{\alpha-1} \frac{Z_\alpha Z_\beta}{|\vec{R_\alpha} - \vec{R_\beta}|} + \sum_{\alpha=1}^{M} \sum_{i=1}^{N} \frac{-Z_\alpha}{|\vec{R_\alpha} - \vec{r_i}|} \tag{2.1}$$

where $\vec{R_\alpha}$ is the position vector of nucleus α, $\vec{r_i}$ is the position vector of electron i, ∇_α^2 is the kinetic energy operator for nucleus α and ∇_i^2 is the kinetic energy operator for electron i. In Born-Oppenheimer approximation, the nuclei of the molecule can be assumed to be fixed considering that the electrons move much faster than nuclei, which allows deriving the electronic Hamiltonian $\hat{H}$ for N electrons moving in the field of M nuclei at fixed positions from eq.(2.1).

$$\hat{H} = \sum_{i=1}^{N} \frac{-1}{2} \nabla_i^2 + \sum_{i=2}^{N} \sum_{j=1}^{i-1} \frac{1}{|\vec{r_i} - \vec{r_j}|} + \sum_{\alpha=1}^{M} \sum_{i=1}^{N} \frac{-Z_\alpha}{|\vec{R_\alpha} - \vec{r_i}|} \tag{2.2}$$

$$\hat{H} = \hat{T}_e + \hat{V}_{ee} + \hat{V}_{eN} \tag{2.3}$$

Using $\Psi(\vec{r}, \sigma)$, where $\vec{r}$ represent the space coordinates and σ represent the spin coordinates, as the exact N-electron ground state wave function for the Hamiltonian above, the energy of the electronic ground state will be:

$$W_0 = \langle \Psi | \hat{H} | \Psi \rangle \tag{2.4}$$

$$= \int d\vec{x} \Psi^*(\vec{x}) \hat{H} \Psi(\vec{x}) \tag{2.5}$$

$$= \int d\vec{x} \Psi^*(\vec{x}) \left(\sum_{i=1}^{N} \left[\frac{-1}{2} \nabla_i^2 + \sum_{\alpha=1}^{M} \frac{-Z_\alpha}{|\vec{R_\alpha} - \vec{r_i}|} \right] + \frac{1}{2} \sum_{i=2}^{N} \sum_{j=1}^{i-1} \frac{1}{|\vec{r_i} - \vec{r_j}|} \right) \Psi(\vec{x}) \tag{2.6}$$

2.2 The Hohenberg-Kohn theorem

Assuming that $\hat{H}$ is the true Hamiltonian of a N-electron system, Ψ_0 is the exact ground state wavefunction, ρ_0 is the exact ground state density and E_0 is the exact ground state energy, Hohenberg-Kohn [55] proved that for molecules with a nondegenerate ground state, the ground state molecular energy, wave function, and all other molecular electronic properties are uniquely determined by the ground state electron density.

The first Hohenberg-Kohn theorem establishess that it is possible to calculate all the ground-state molecular properties from ρ_0. This indicates that all of the information for the Hamiltonian operator of a ground electronic state is included in the electron density [56].

$$E = E[\rho(\vec{r})] \tag{2.7}$$

$$E = T_e + V_{ee} + V_{eN} \tag{2.8}$$

Since V_{eN} and E are both functionals of $\rho\ (\vec{r})$, the sum $(T_e + V_{ee})$ must also be a functional of ρ. We define this quantity as $F[\rho(\vec{r})]$,

$$F[\rho\ (\vec{r})] = T_e[\rho\ (\vec{r})] + V_{ee}[\rho\ (\vec{r})] \tag{2.9}$$

The second Hohenberg-Kohn theorem states that the energy minimum is obtained when we use the ground state density in equations (2.7) and (2.9). It is a variational theorem for the energy with respect to the electron density.

According to first Hohenberg-Kohn theorem, $\rho_0(\vec{r})$ determines all properties of the ground state, for instance the potential energy, the kinetic energy and the total energy. In practice, one cannot find $\Psi[\rho]$ just by knowing ρ. Also the functional $F[\rho]$ in eq (2.9) is defined independently of the external potential $V(\vec{r})$. So one has to use physical models and devise approximate functionals $T_e[\rho]$ and $V_{ee}[\rho]$. This indicates that universal density functionals of the kinetic and electron-electron interaction operators are required, independent of the nuclear coordinates. There is no simple connection between an electron density and kinetic energy. Kohn and Sham devised an accurate and practical method for calculating the kinetic energy by writing the electron density as a sum of occupied orbital contributions.

2.3 Kohn-Sham equations

The energy in DFT without orbitals is,

$$E[\rho] = T[\rho] + E_{eN}[\rho] + V_{ee}[\rho] \tag{2.10}$$

The Kohn-Sham (KS) DFT energy expression (with orbitals) can be written as [52],

$$E_{[}\rho] = T_s[\rho] + E_{eN}[\rho] + J[\rho] + (V_{ee}[\rho] - J[\rho]) + (T[\rho] - T_s[\rho]) \tag{2.11}$$

$$E_{xc}[\rho] = V_{ee}[\rho] - J[\rho] + T[\rho] - T_s[\rho] \tag{2.12}$$

$$E[\rho] = T_s[\rho] + E_{eN}[\rho] + J[\rho] + E_{xc}[\rho] \tag{2.13}$$

where E_{eN} is the electron-nuclear attraction, J is the Coulomb part of the electron-electron repulsion, and E_{xc} is the electron exchange correlation. T_s is the kinetic

energy of the N electrons for a fictitious system that has the same density as the true system but where there is no electron- electron repulsion

$$T_s[\rho] = \sum_{i}^{occ} n_i |\phi_i|^2 \tag{2.14}$$

where ϕ_i are the orbitals and without which $T_s[\rho]$ cannot be defined. The E_{xc} term should be universal and practical, but unfortunately it is not known and has to be approximated.

Kohn and Sham [57] invented an indirect approach to calculate the kinetic energy functional, $T[\rho]$, thereby turning DFT into a practical tool for calculations. They considered a fictitious system of N non-interacting electrons, such that each electron experiences the same external potential. Also, the ground-state electron density of the fictitious system is exactly the same as in the real system.

$$\hat{H}' = \sum_{i=1}^{N} [\frac{-1}{2}\nabla_i^2 + \ (\sum_{\alpha=1}^{M} \frac{-Z_\alpha}{|\vec{R}_\alpha - \vec{r}_i|} + V_i''(\vec{r})] \tag{2.15}$$

$$\hat{H}' = \sum_{i=1}^{N} [\frac{-1}{2}\nabla_i^2 + V_i'(r)] \tag{2.16}$$

$$\hat{H}'\Psi' = \hat{E}'\Psi'; \Psi' \rightarrow \rho(\vec{r}) \tag{2.17}$$

The assumption that $\rho(\vec{r})$ is the ground state density of both a real Hamiltonian and a fictitious Hamiltonian does not conflict with the HK theorem.

According to KS theory, the Hamiltonian in (2.17) is used to set up a 1-electron Schrödinger equation:

$$\hat{H}'(\vec{r_1})\phi_k(\vec{r_1}) = \epsilon_k\phi_k(\vec{r_1}) \tag{2.18}$$

where $\hat{H}'(\vec{r_1})$ is the first term in the sum in equation (2.16), and the solutions ϕ_k ($k = 1, 2, 3, \ldots$) are the so-called spin orbitals.

For non-interacting electrons, the kinetic energy term can be written exactly as:

$$T_s = \int d\vec{r_1}\phi_k^*(\vec{r_1})(\frac{-1}{2}\nabla_1^2)\phi_k(\vec{r_1}) \tag{2.19}$$

Let ΔT be equal to the difference in the ground state kinetic energy of the real system and the fictitious system:

$$\Delta T = T_s - T_e \tag{2.20}$$

We assumed at the beginning that $\rho(\vec{r})$ is the ground state density for both the real and the fictitious Hamiltonian. This implies that they must have the same electron-nucleus term in the energy and in the potential. So one part of $\hat{V}'(\vec{r})$ must be the potential corresponding to V_{eN},

$$v_{eN}(\vec{r_1}) = \sum_{\alpha=1}^{M} \frac{-Z_\alpha}{|\vec{R_\alpha} - \vec{r_1}|} \tag{2.21}$$

A first-order approximation to the electron-electron repulsion term V_{ee} of the real system is:

$$V_{ee} \approx \frac{1}{2}\iint d\vec{r}_1 d\vec{r}_2 \frac{\rho\ (\vec{r_1})\rho\ (\vec{r_2})}{|\vec{r_1} - \vec{r_2}|} \tag{2.22}$$

The right-hand side of eq. (2.22) is the $J[\rho]$ of equations (2.2), (2.3) and (2.4). The corresponding approximate 1-electron potential is $\tilde{v}_{ee}(\vec{r}_1)$:

$$\tilde{v}_{ee}(\vec{r}_1) = \int d\vec{r}_2 \frac{\rho\ (\vec{r}_2)}{|\vec{r}_1 - \vec{r}_2|} \tag{2.23}$$

We define the exchange-correlation potential as:

$$v_{xc}(\vec{r}_1) \equiv V'(\vec{r}_1) - v_{eN}(\vec{r}_1) - \tilde{v}_{ee}(\vec{r}_1) \tag{2.24}$$

So with eq.(2.20) to eq.(2.24), eq.(2.16) and eq.(2.17) become the Kohn-Sham equations for electron "1":

$$\hat{H}^{KS}(\vec{r}_1) = \frac{-1}{2}\nabla_1^2 + \sum_{\alpha=1}^{M} \frac{-Z_\alpha}{|\vec{R}_\alpha - \vec{r}_i|} + \int d\vec{r}_2 \frac{\rho(\vec{r}_2)}{|\vec{r}_1 - \vec{r}_2|} + v_{xc}(\vec{r}_1) \tag{2.25}$$

$$\hat{H}^{KS}(\vec{r}_1)\phi_k(\vec{r}_1) = \epsilon_k \phi_k(\vec{r}_1) \tag{2.26}$$

$$\rho(\vec{r}_1) = \sum_{k=1}^{N} |\phi_k(\vec{r}_1)|^2 \tag{2.27}$$

$$E^{KS} = T_s + V_{eN} + J + E_{xc} \tag{2.28}$$

According to the HK theorems, E_{xc} is a unique functional of the density; so $E_{xc} \equiv E_{xc}[\rho(\vec{r})]$. Then $v_{xc}(\vec{r})$ is the functional derivative of E_{xc}:

$$v_{xc}(\vec{r}) = \frac{\delta E_{xc}[\rho(\vec{r})]}{\delta \rho(\vec{r})} \tag{2.29}$$

Electron spin is treated approximately by having equations of the form (2.29) for both up and down spin. Consequently, each of the equations (2.25) to (2.27) will

have two spin components. The exact functional $E_{xc}[\rho(\vec{r})]$ is not known. However, several approximate functionals $E_{xc}[\rho(\vec{r})]$ have been developed over the years. For example, Local density approximation (LDA) (e.g. VWN [58]), Generalized gradient approximation (GGA) (e.g. PBE [59]), meta-GGA (e.g TPSS [60]), and hybrid (BP86 [61]).

In practice the exchange-correlation functional is represented by,

$$E_{xc}[\rho(\vec{r})] = \int d\vec{r}\, e_{xc}(\vec{r}) \tag{2.30}$$

LDA assumes,

$$e_{xc}(\vec{r}) = e_{xc}(\rho(\vec{r})) \tag{2.31}$$

In GGA, $e_{xc}(\vec{r})$ is a function of both the electron density and its gradient:

$$e_{xc}(\vec{r}) = e_{xc}(\rho\ (\vec{r}), |\vec{\nabla}\rho(\vec{r})|) \tag{2.32}$$

Following GGA's are the *meta-GGA's* that depend on electron density, as well as, its first and second gradient. Another class of exchange correlation functionals are the *hybrid* functionals. Hybrid functionals are energy functionals that contain both a DFT exchange (LDA part or a GGA part) and a Hartree-Fock type exchange calculated from the orbitals.

LDA is known to underestimate the lattice constants, overestimate bulk moduli, and considerably overestimate cohesive energies in most situations. GGA functionals retain most of the correct features of the LDA and greatly advance the accuracy [63], especially for molecular binding energies. GGA's significantly improve

upon calculating the cohesive energy and give more accurate bond lengths. However, they show a tendency towards underbinding [64, 65, 66, 67, 68, 69, 70]. While some meta-GGAs predict cohesive properties with reasonable accuracy for specific systems [65, 66, 67, 68, 69, 71, 72, 73], improvements in the lattice constant are often accompanied by a worsening of the bulk modulus or the cohesive energy, or both. Hybrid functionals often show superior performance over LDA, GGA, and meta-GGA in describing some bulk properties, including lattice constants and band gaps, however both bulk moduli and cohesive energy can be worse than those of GGA [64].

Tran *et al.* [74] tested and compared the performance of numerous DFT functionals (LDA,GGA, meta-GGA and hybrid) for the calculation of lattice constant, bulk modulus, and cohesive energy in solids. Results are summarized in Table 2.1 for some of the most commonly used functionals: Perdew-Burke-Ernzerhof (PBE) [59] from GGA, Tao-Perdew-Staroverov-Scuseria (TPSS) [60] from meta-GGA and Becke-3parameter-Lee-Yang-Parr (B3LYP) [62] from hybrid functionals. GGA and meta-GGA give the most accurate results for calculations of molecular geometry and energetics.

Table 2.1: A comparison of the mean absolute error (MAE,%) and mean absolute percentage error (MARE,%)in lattice constants $a_0(\mathring{A})$, cohesive energies $E_{coh}(eV/atom)$ and bulk moduli B_0 (GPa) of bulk crystals using different density functional approximations reported from literature benchmarks [64, 74]

.

		LDA	PBE	TPSS	B3LYP
a_0	MAE	0.071	0.061	0.054	0.084
	MARE	1.5	1.2	1.1	1.7
E_0	MAE	0.77	0.19	0.20	0.84
	MARE	17.2	5.0	4.9	22.9
B_0	MAE	11.5	12.2	9.6	14.5
	MARE	9.4	11.0	10.3	13.1

Chapter 3

Theoretical Models

3.1 Jellium model

Over the last three decades, electronic shell models played a central role in understanding the properties and stability of alkali, alkaline earth and coinage metal clusters [23]. The spherical jellium model has been greatly successful for understanding the electronic properties of many metal clusters and account for their stability. The Jellium model is defined by a Hamiltonian that treats the electrons as usual but replaces the ionic cores with a uniform positively charged background. Core electrons are ignored, nuclear charges are replaced by a homogeneous positive charge of density $\rho^+ = N/V$ confined to a sphere of volume V. The N valence electrons are subjected to the external potential of that jellium. This leads to a description of the electron density in terms of single-particle wave functions that extend over the entire cluster. Solutions to the one-electron Schrödinger equation for the spherical jellium display a shell structure with electrons arranged in states of increasing energy with the pattern

$1s^2, 1p^6, 1d^{10}, 2s^2, 1f^{14}, 2p^6 1g^{18} \ldots$. The jellium model reproduces the drops associated with the closing of electronic shell in the experimental ionization energies for Li, Na and K clusters [77]. In mass spectrometry experiments of Na clusters with cluster size $M = 2 - 100$, large peaks were observed for clusters having $8, 20, 40, 58$, and 92 atoms [23]. This indicated that clusters having a number of valence electrons corresponding to shell closing numbers $(N = 8, 20, 40, 58, \ldots)$ of spherical potential were produced more abundantly. This observation was further supported by Choy *et al.* [77] who in their study on Li, Na and K clusters compared the electronic properties of these clusters to the spherical jellium model. Similar to the experiment by Knight *et al.* [23], they also found peaks in the relative binding energy and discontinuities in total energy as a function of cluster size matching the shell closing numbers. This observation was explained by Knight *et al.* [23] in terms of a model spherical potential for 3s valence electrons for Na clusters. Clusters having just enough valence electrons to fill the shells of bound electron states are more stable as compared to other cluster sizes. In terms of atomic and molecular physics, the closed shell electronic configurations have enhanced stability because of the existence of energy gaps between the electronic shells. Larger gaps between the electronic shells increase stability and correspond to the observed magic numbers.

However, assuming that the geometry of small clusters is spherical can only be justified for closed-shell clusters. According to the Jahn-Teller theorem, open-shell clusters must be distorted [78]. Clemenger further developed the jellium model by introducing a deformable potential well to account for the distortion effect . Clemenger's ellipsoidal jellium model (EJM) makes predictions about the overall shape of the clus-

ters as a function of N that generally agree with the geometries obtained by more rigorous calculations such as KS-DFT. For instance, the KS-DFT optimized geometries of Ag_n [79] using TPSS functional and LANL2DZ basis set were found to be quasi-spherical for $n = 8, 18$ and 20, prolate for $n = 4, 9, ..., 13$ and oblate for $n = 5, 6, 7, 14, ..., 17$ in very good agreement with the EJM [23].

3.2 Atomic shell model

In addition to electronic shell structure, atomic shells (also called geometric shells) are also useful to understand trends in the stability of clusters. According to the atomic shell model, the surface energy of clusters should be minimized and the number of nearest-neighbour pairs should be maximized. With increasing size, the clusters grow by adding on layers or shells on the polyhedral surface. Fig. 3.1 (a) shows the number of new bonds formed with increasing cluster size (number of atoms). Fig. 3.1 (b) shows the variation of ratio of number of surface atoms to interior atoms as a function of cluster size. Surface-to-volume ratio decreases with increasing cluster size, thereby decreasing the surface energy with increasing cluster size.

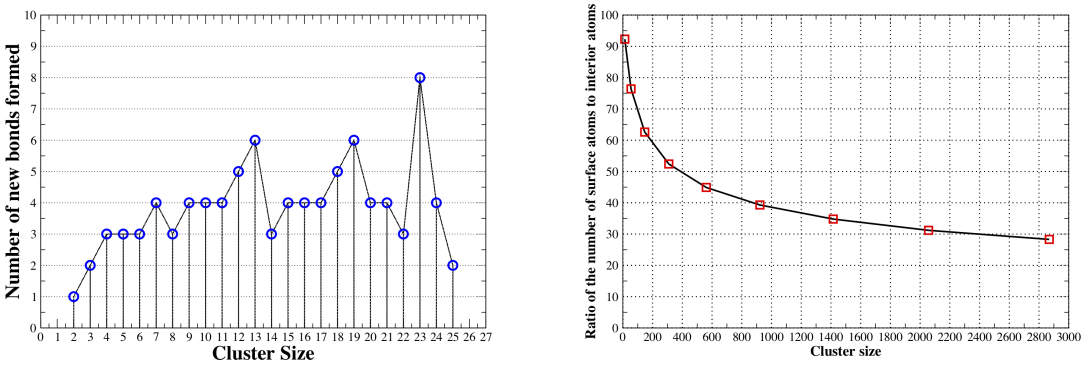

(a) **(b)**

Fig. 3.1. (a) Number of new bonds formed with increase in cluster size for Lennard Jones (LJ) global minima and (b) Ratio of number of atoms on surface to interior atoms, using Mackay's formula [5], for the first 9 shells.

Clusters of noble gas atoms form closed packed structures, and most stable clusters are formed when the atomic shells are closed. The number of atoms in the more stable species is referred to as "magic number", the origin of which has been attributed to electronic shell structure [23]. For a given geometric shape (cubic, tetrahedral, octahedral, icosahedral etc.) a specific number of atoms is required to form a closed geometry. For example, icosahedral clusters exhibit K closed-atomic shells when the number of atoms $N_a = (10/3)K^3 - 5K^2 + (11/3)K - 1$ $(N_a = 13, 55, 147 \ldots)$ for $(K = 2, 3, 4 \ldots)$.

13 atom **55 atom**

Fig. 3.2. Global Minima for Lennard Jones clusters

Mackay [5] suggested that the number of atoms required to make a closed icosahedral geometry can be determined as $S_n = 10n^2+2$, where S_n represents the surface atoms of the n^{th} shell. Thus, clusters with $13, 55, 147, 309, 561..$ atoms correspond to closed atomic shells. It leads to shell closing at $n = 13$ for poly-tetrahedral global minima. Fig.3.2 shows the 13 and 55 atoms icosahedron for LJ-clusters [81]. Recknagel *et. al.* [82] in their experiment on Xe clusters, experimentally observed the existence of magic numbers for cluster size $n = 13, 55, 147$.Charkin [84] *et al.* found icosahedron to be the most stable structure for doped aluminium clusters XAl_{12}. Earlier studies by Doye [83] and Sun et al. [85] showed that the I_h like structures are most stable for Al_{13}, Al_{55} and Al_{147}. Aguadoa [86], and Rao and Jena [87] found the most stable structure for Al_{13} to be a distorted icosahedron. Fournier *et al.* [88], in their study of 26 metal elements, found 13-atom icosahedron to be the most stable structure in 7 cases out of 26. For other 19 elements, the icosahedron was unstable.

3.3 Maximum hardness principle

The Maximum hardness principle (MHP) states that under certain conditions, larger values of chemical hardness $(I - A)$ correlate with lower values of total energy [6, 89, 90, 91, 92] where I is the ionization potential and A is the electron affinity. An important idea of the MHP is that the electronic systems always evolve to the equilibrium state with the highest possible hardness value. Instead of total energy, hardness correlates with kinetic stability. Therefore the stability of clusters with "magic numbers", can be understood as a manifestation of the MHP [93]. In practical applications, the HOMO-LUMO gap is used instead of $(I - A)$. A *hard molecule* has a large value of energy gap and a *soft molecule* has a small gap [6]. Knickelbein *et al.* and Rayner *et al.* in their experiment with Niobium clusters and Niobium oxide clusters, correlated ionization potential with reactivity [94, 95]. Koopmans theorem [96] for closed shells in Hartree-Fock theory states that the energies ϵ_i of the occupied orbitals ϕ_i approximate the corresponding vertical ionization potentials (VIPs) I_i,

$$\epsilon_i \approx -I_i \tag{3.1}$$

The KS-DFT analogue of Koopmans theorem gives that, for the true exchange-correlation functional, the ionization energy ϵ_i is equal to the highest occupied molecular orbital (HOMO) [97, 98, 99, 100, 101, 102, 103]

$$\epsilon_H^{KS} = -I_H \tag{3.2}$$

With the proper choice of exchange correlation functional, Kohn-Sham HOMO energies very closely approximate the negative of the corresponding vertical ionization potential [104, 105, 106].

Chapter 4

Computational Methods

4.1 Global optimization

Global optimization (GO) of geometry is a central problem in computational studies of clusters. The lowest-energy structures are usually the most abundant in experiments on clusters. Therefore, discovering the lowest energy cluster isomers is critical for the relevance of theoretical studies [108, 109]. However, structural optimization of clusters is a difficult problem because of the huge number of possible isomers. For example, for a 13-atom Lennard Jones clusters or LJ clusters (N-particle system interacting through the Lennard- Jones pair potential; $v_{LJ}\ (r) \approx r^{-12} - 2r^{-6}$), there are at least 1506 distinct local minima [110]. The number of distinct minima on potential energy surface of cluster A_n grows exponentially with n [47, 110]. For example, for n = 13 - 15, the number of minima of n-atom clusters should be in thousands and probably on the order of $10^4 - 10^6$ for $15 < n < 25$. The computer cost of one energy evaluation is large as compared to all other operations in global optimization,

such as generation of random numbers, calculations of interatomic distances etc. For reducing computational costs, cluster structure global optimizations are often done with empirical potentials, sometimes followed by local optimizations with more accurate methods such as DFT. Cheng and Fournier [48] devised a computationally efficient algorithm for searching the global energy minimum structure of atomic clusters. They called this algorithm, Taboo search in Descriptor space (TSDS). This algorithm screens the cluster by interpolation over descriptor space calculating the structural descriptors and retaining only few (10% or less) for energy evaluations. This way, between 10 and a 100 times fewer energy evaluations than a good genetic algorithm, are required for locating the global minimum of n-atom clusters (n$<$ 35) described by a LJ potential.

Our global optimization (GO) strategy has similarities to TSDS, but it has new features as well. We devised a global optimization strategy that optimizes molecular property with respect to both nuclear configuration X (geometry) and chemical composition C. We limit the range of possible compositions by specifying: (a) a list of allowed elements $Z_1, Z_2, \ldots, Z_k$; (b) minimum and maximum numbers of atoms for each element, $N_{min,1}$, $N_{max,1}$, $N_{min,2}$, $N_{max,2}$, $\ldots$, $N_{min,k}$, $N_{max,k}$; and (c) minimum and maximum numbers of total atoms, N_{min} and N_{max} Taking small Li_mAl_n clusters as an example, we could have, for instance: (a) $Z_1 = 3$ and $Z_2 = 13$; (b) $N_{min,1} = 0$, $N_{max,1} = 12$, $N_{min,2} = 0$, $N_{max,2} = 12$; and (c) $N_{min} = 3$ and $N_{max} = 12$. With these constraints, $13 + 12 + ... + 4 = 85$ chemical species are possible.

Our GO proceeds as follows: In the first stage, algorithm generates M random geometric structures or "*candidate*" structures. Each time, it randomly selects a

chemical composition that satisfies the constraints. Then it generates a random nuclear configuration as follows. It puts the first atom at the origin. The second atom is placed a distance $r_{ij} = (r(Z_i) + r(Z_j))$ away from the first atom at random position on the sphere centered about the first atom, where $r\ (Z_i)$ and $r\ (Z_j)$ are the atomic radii of atoms i and j. For every subsequent atom j, an atom i is randomly selected among the n previous atoms, and atom j is put randomly on the sphere of radius $r(Z_i) + r(Z_j)$ centered about atom i. Their energies $U_j = U(C_j, X_j)$ are calculated, usually by a DFT method. The configurations and their energies U_j are saved to disk.

In the second stage, algorithm performs K iterations. At each of these iterations, one new configuration is generated, its DFT energy is calculated, and the information is written on disk. The method to create a new configuration starts with calculating the RITS (explained in section 4.3) of the $M + K$ molecules in the dataset. The objective function F_j is calculated for every j in the database. A selection probability W_j is assigned to every j:

$$W_j = \exp[((F_{min} - F_j)/\alpha(F_{min} - F_{med}))]/\sum_k w_k \tag{4.1}$$

$$w_k = exp[(F_{min} - F_k)/\alpha(F_{min} - F_{med})] \tag{4.2}$$

where F_{min} is the minimum value of F in the database, F_{med} is the median value, and α varies between a high value of 1.00 at $k = 1$ and a low value typically equal to 0.04 at the last iteration. By varying α this way, the importance given to energy in the selection process is gradually changed, with a weak emphasis during the first few iterations, to favor exploration of the search space, and a strong emphasis during the

last few iterations, to exploit the knowledge gained about good solutions.

Next, a random operation O_i with probability p_i is selected, and either two parents A and B (for operations 1 and 2) are selected or a single parent A (for the other operations) is selected. Following the operation, the "repair" algorithm is applied to improve the atomic configuration. With these steps, a candidate molecule is created.

Newly created structures normally have one or more unphysical interatomic distances, for instance, a Ag-Ag distance of 1.0 Angstrom. To fix this problem, we use a special "repair" algorithm that works like this: (1) a list of nearest-neighbor (NN) is established using sums of atomic radii as a criterion to decide if two atoms are NN; (2) an empirical interatomic distance (target distance) is assigned to every NN pair. Then, a distance-geometry algorithm is used to generate a set of atomic coordinates that most closely reproduce all of the NN target distances, and has interatomic distances for non-NN pairs greater than the sum of their atomic radii.

Each candidate structure is assigned a score S_j. The score S_j is made up of three terms.

$$S_j = -S_{j,F} + S_{j,s} + S_{j,r} \tag{4.3}$$

$$S_{j,F} = exp[(F_{min} - \tilde{F}_j)/\alpha(F_{min} - F_{med})] \tag{4.4}$$

where $\tilde{F}_j$ is an estimate of the objective function for candidate j obtained by interpolating over the F_k values of molecules with the same composition (but different configurations). The term $S_{j,s}$ is a penalty for a configuration that is similar to earlier

configurations.

$$S_{j,s} = \sum_{k} exp(-\Delta_{j,k}^2/\beta^2) \tag{4.5}$$

$$\Delta_{j,k} = (1/N_d) \sum_{m}^{N_d} [\ (D_{j,m} - D_{k,m})/(D_{max,m} - D_{min,m})]^2 \tag{4.6}$$

Here, $D_{j,m}$ is the m'th geometric descriptor of molecule j, $(D_{max,m} - D_{min,m})$ is the range of descriptor m, and N_d is the number of descriptors. The sum over k is over configurations of molecules with the same chemical composition as j; $\Delta_{j,k}$ can be thought of as a kind of distance between the configurations j and k of a same chemical species. Finally, β is a parameter that varies from a high value (typically 0.25) at the beginning of the optimization, to a low value (typically 0.08) near the end of the optimization. For a given distance $\Delta_{j,k}$, higher β produces a bigger penalty term. So, a high β favors the creation of highly dissimilar structures early on (exploration). The small value of β near the end of the optimization allows a finer search in the vicinity of the best solutions (exploitation).

Finally, $S_{j,r}$ is just a random number chosen in [0, 1] at the beginning of the optimization (a high random term favoring exploration), and chosen in [0, 0.01] near the end of the optimization (favors a deterministic search).

The candidate with the lowest score S_j is singled out, its DFT energy and objective function $F(C, X)$ are evaluated, and it gets added to the dataset.

After a preset number of iterations, the second stage is complete. At this point, we have a set of N molecules or clusters whose configurations were designed in a such a way that they are near a local minimum of the potential energy surface. An alternative would be to carry a full local minimization of the DFT energy as part of

the 'repair' algorithm. This would bring each of the N molecules to a local minimum, which is desirable, but it would come at a very high computational cost (a factor of 50 increase, roughly, for molecules and clusters of moderate size). Instead, we carry local optimization of the DFT energy for a small number $N_{opt.}$ ($N_{opt} < N$) of molecules, only those that look the most promising. This constitutes the third stage of the optimization. We calculate the RITS and the objective function F one last time and rank the N molecules by order of increasing F. We perform local geometry optimization for the molecules with the lowest F, using the geometric descriptors $D_{j,m}$ to avoid repeating calculations for molecules that are essentially identical to any of the higher ranked molecules.

In the final step, local optimization of the DFT energy is performed for L best solutions. In a parallel GO of geometry, we typically set L between 10 and 20.

4.2 Descriptors

TSDS [48] uses structural descriptors such as "mean atomic coordination" and "mean nearest neighbor interatomic distance" to describe cluster structure, in addition to atomic coordinates. Descriptors are useful because they give a better insight into the structure as compared to atomic cartesian coordinates. Also only fewer descriptors are needed as compared to $3n$ cartesian coordinates to describe the molecular structure. These descriptors are used to implement the rules for avoiding previous structures, and also as interpolation variables for calculating a model energy from those of previously visited structures.

The six descriptors used in TSDS [48] are as follows.

Four descriptors are derived from coordination number, c_k, defined as the number of atoms within the sphere of d_{max} (maximum allowable distance between bonded pair of atoms) around atom k. These descriptors are the mean, root-mean-square (rms) scatter, minimum, and maximum of atomic coordinations.

$$Mean\ (c) = (1/n) \sum_{k=1}^{n} c_k \tag{4.7}$$

$$Rms\ (c) = \left(\sum_{k=1}^{n} [c_k - Mean(c)^2 \right)^{1/2} \tag{4.8}$$

$$c_- = min\ c_k \tag{4.9}$$

$$c^+ = max\ c_k \tag{4.10}$$

Two descriptors are derived from moments of inertia $I_a \geq I_b \geq I_c$: the asphericity (ζ) and shape (η).

$$\zeta = \frac{(I_a - I_b)^2 + (I_b - I_c)^2 + (I_c - I_a)^2}{I_a^2 + I_b^2 + I_c^2} \tag{4.11}$$

$$\eta = (2I_b - I_a - I_c)/I_a \tag{4.12}$$

These descriptors quantify the departure from spherical shape towards a more oblate ($\zeta < 0$) or more prolate structure ($\eta > 0$).

4.3 Geometric operations

Our GO uses a variety of simple operators to explore the possible geometries of a molecule or cluster. The operations we use are the following.

1. Put the center of mass of molecule A at the origin, and give a random orientation to A; keep atoms of A with a positive x coordinate; repeat for molecule B to make a fragment X_b by keeping the atoms with a negative x coordinate; put the two fragments X_a and X_b together; keep this molecule if it satisfies all constraints, otherwise, try again.

2. Like the previous operation, except that now we select at random two bonded atoms i and j in parent A, we put the midpoint $(\vec{r_i} + \vec{r_j})/2$ at the origin, we put atoms i and j on the x axis, we define the plane perpendicular to $\vec{r_i} - \vec{r_j}$ that contains the midpoint $(\vec{r_i} + \vec{r_j})/2$, and we keep atoms of A that have a positive x coordinate in that frame of reference; we repeat for B, keeping atoms with a negative x coordinate; and we assemble the two fragments as before.

3. Relocate a randomly selected atom i to a new position on a sphere of radius $r(Z_i) + r(Z_j)$ centered about a randomly selected atom j.

4. Choose an atom j at random, and give random displacements $(\delta x_i, \delta y_i, \delta z_i)$ to every atom i, where the magnitude of the displacement vector is a decreasing function of the distance to atom j.

5. Interchange the positions of two randomly selected atoms i and j, with $Z_i \neq Z_j$

6. Delete a randomly chosen atom i.

7. Choose an element Z_{new} at random, choose an atom i at random, and add an atom of element Z_{new} somewhere on the sphere of radius $r(Z_i) + r(Z_{new})$ centered about atom i.

8. Transmutation: choose an atom i at random, and change its atomic number from Z_i to $Z_{new} \neq Z_i$.

9. A typical choice of probabilities for these operations is $p_1 + p_2 = 0.8$ and $p_3 = p_4 = p_5 = p_6 = p_7 = p_8 = 0.033$. The probability is assigned in a way so as to give more importance to binary operations 1 and 2 and lesser importance to mutation operations. This is because genetic algorithms (GA) work better when binary operations are used most of the time.

4.4 Relative Index of Thermodynamic stability

This sections contains contents from the paper "Optimizing molecular properties using a relative index of thermodynamic stability and global optimization techniques" by René Fournier and Amir Mohareb [111]

The Relative Index of Thermodynamic Stability (RITS) allows stability comparison between different chemical species. RITS can be used by itself or in combination with other property F to create an objective function. This objective function can be used to optimize the property of interest, at the same time ensuring that the predicted species are thermodynamically stable. Consider that we wish to minimize property P for a chemical composition C and nuclear configuration X. For example, we choose P to be negative of the magnitude of the HOMO-LUMO gap. We also limit the range of possible chemical compositions C by putting constraints on the maximum and minimum number of atoms and number of total atoms in cluster. To avoid getting completely meaningless compositions, one must include energy, somehow, into the

definition of the objective function to be minimized. But the usual energy functions such as the atomization energy (AE), cohesive energy, etc. do not allow direct comparison between molecules of different compositions. RITS, however, allows direct comparisons between molecules of varying sizes and chemical compositions. This, in turn, allows to construct an objective function whose minima are chemical species with low P values and some degree of thermodynamic stability, which makes them chemically relevant.

We define $R\ (C, X)$, RITS, as

$$R(C_j, X_j) = AE(C_j, X_j) - AE_{fit}(C_j) \tag{4.13}$$

where $AE\ (C_j, X_j)$ is the energy of a N-atom molecule with chemical composition C_j and geometry X_j relative to the N separated ground state atoms, and $AE_{fit}(C_j)$ is a model energy independent of geometry and fitted to the set of atomization energies as explained below.

$$AE(C_j, X_j) = U(C_j, X_j) - \sum_i N_{j,i} U_i \tag{4.14}$$

$U(C_j, X_j)$, is the energy of the j^{th} configuration, U_i is the energy of an atom of the i^{th} element and $N_{j,i}$ is the number of atoms of element i in molecule j. The set of atomization energies AE_j is fitted to a simple equation.

$$AE_{fit}(C_j) = \sum_i N_{j,i} U_c(Z_i) \tag{4.15}$$

The adjustable parameters of the fit, $U_c(Z_i)$, are obtained by ordinary least-squares and can be interpreted as the mean energies of atoms-in-molecules of element i for that particular data set of molecular energies.

Hence, $R(C_j, X_j)$ is an implicit comparison of the atomization energy of molecule j to the atomization energies of all other molecules in the data set. It is an energy difference measured in eV.

The RITS, R, has two desirable properties. Its average over the data set is roughly zero, and energies of reactions equal sums and differences of RITS values. It can also be noted that R expresses stability only in relation to a set of configurations. But the RITS has a potential flaw in that it is size extensive property. So with R, large molecules would be deemed more stable. For instance, the R values of the dimer $(N_2)_2$ and linear alkane $CH_3(CH_2)_8CH_3$ are about twice as large as those of N_2 and $CH_3(CH_2)_3CH_3$, respectively. So R does not give meaningful comparisons of stability between molecules of different sizes. Therefore, we also define a 'dimensionless' stability index $S(C_j, X_j)$.

$$S(C_j, X_j) = R(C_j, X_j)/AE_{fit}(C_j) \tag{4.16}$$

In optimization of molecules with a number of atoms ranging between N_{min} and N_{max}, those with N_{max} atoms will be systematically favored (when using R) over those with fewer atoms. In such a case the dimensionless index S may be more appropriate.

We can combine the RITS with a molecular property "P" to create an objective function by using the means of R and P, Mean (R) and Mean (P), the standard deviations (SDs) of R and P, SD (R) and SD (P), and a coefficient c $(0 \leq c \leq 1)$,

$$F_{ob}(C, X) = c[(R(C, X) - Mean(R))/SD(R)] + (1 - c)][P(C, X) - Mean(P))/SD(P)] \tag{4.17}$$

With this definition, F(C, X) usually varies between between -3 and +3. The constant c can be chosen in such a way, so as to give the weight to the property being chosen or stability. Optimizing with $c = 1$ amounts to searching the space of chemical composition and nuclear configurations for thermodynamically stable species.

4.5 Errors in calculations

There are many sources of errors in the calculations that we report in the next chapters. Firstly, there might be errors directly associated with the computational or numerical methods, for example, termination criteria for convergence of orbitals or geometries. These type of errors can be assessed by repeating the calculations with slightly varying the input parameters. However, these errors are very small on the order of 0.01 eV or less. Another type of errors which are much larger, can be associated with the approximate ways by which the KS equations are represented. DFT utilizes exchange correlation functionals, used to approximate electron - electron interactions. There is no exact closed form exchange correlation functional that perfectly predicts electron exchange and electron correlation for all materials. These errors are not breakdowns of the theory itself but they occur due to the deficiencies of the currently used approximate exchange-correlation functionals. The prediction of low band gaps, low reaction barriers, low stability of molecular anions, etc., by KS density functional methods are often attributed to the incomplete cancellation of many-electron self interaction [112, 114]. However, these errors are absolute, thus not a big concern. The relative errors are much more difficult to assess.

In an exhaustive study performed by Mardirossian *et al.* [115], 200 density functionals on a molecular database of about 5000 data points were compared. Root mean square deviation (RMSD) associated with PBE for isomerization energy was reported to be 1.15 kcal/mol, which is least compared to other GGA functionals as well as LDA, meta- GGA's and hybrid functionals considered (TPSS, B3LYP etc.). Mardirossian *et al.* [115] divided their dataset into subsets. One of them is called NCED (non-covalent easy dimers) and another NCEC (non-covalent easy clusters). The *easy* indicates that these cases are relatively easy for theory. The PBE functional gave RMSD on binding energies of 1.96 kcal/mol for the NCED subset, and 4.08 kcal/mol for the NCEC subset.

Table 2.1 summarizes the mean absolute error in calculations (eV/atom) using LDA, PBE (GGA), TPSS (meta-GGA) and HSE06 (hybrid) functionals. The absolute error with PBE is 0.19 eV/atom, therefore in our calculations we expect a mean absolute error of the order of 0.2 eV.

Chapter 5

Geometric structure of silver clusters with and without adsorbed Cl and Hg.

5.1 Introduction

Silver clusters have been the subject of numerous studies because of their interesting optical [116, 117, 118, 119, 120, 121] and chemical [122, 123, 124] properties and the possibilities they offer for novel materials [125, 126]. Studies of free silver clusters by various experimental [118, 127, 128, 129, 130, 131, 132] and theoretical methods [133, 134, 135, 136, 137, 138, 139, 140, 141] give us a basic understanding of their geometric and electronic structure and physical properties. The interaction of silver clusters with adsorbates reveals their chemistry and serves as a model for catalysts [122, 142, 143]. When bound to a support [144] or embedded in a matrix [145, 146], silver clusters

are stabilized and can be made into useful materials having chemical and physical properties that can be tuned with the choice of host or ligands. Silver clusters bound to DNA have sequence-tunable fluorescence wavelengths [147, 148] and can serve as biosensors [149, 150, 147]. Larger silver nanoparticles (roughly 20 to 100 nm in size) have shape-dependent antibacterial properties [151].

Knowing the geometric structure of silver clusters is important for understanding their properties and designing new materials. Most experiments give only scarce or indirect information about cluster geometry. Accordingly, a lot of effort went into computational predictions of the geometric structure of silver clusters [133, 134, 135, 136, 137, 138, 140, 141, 152, 153]. Such work has focussed mainly on pure clusters in their neutral or charged states, Ag_n, Ag_n^+, Ag_n^-. However, many interesting experiments, and the most promising avenues for materials, deal with silver clusters deposited on a substrate [144, 154] or interacting with ligands [118, 155], adsorbates [122], or a host matrix [146]. It is quite difficult to accurately model these complex systems [156]. A simplified method is to take the computed geometric structures of pure silver clusters combined with some assumed geometry for the host or adsorbates as starting points for local geometry optimizations. It would be useful to develop criteria to help decide when this approach can be used.

We performed a computational study of the geometric structure of Ag_n (n =4 to 20) and related clusters with two goals in mind. *First*, we wanted to verify earlier theoretical predictions of geometric structure. For this, we used a newer, and presumably better, exchange-correlation functional, and we performed a more exhaustive search of geometries. The most complete first-principles study of Ag_n geometric structure

to date is that of Yang *et al.* [138]. It used the PBE exchange-correlation functional. Here, we are using a meta-GGA functional, the one of Tao, Perdew, Staroverov and Scuseria (TPSS) [60, 75]. As for the atomic structure search method, Yang *et al.* used many low-energy isomers of Cu_n as initial guesses for carrying out local optimizations on Ag_n. They showed that relative energies of isomers are comparable between Cu_{10} and Ag_{10}, and that their search method works for Ag_{10}. But there remains a concern that, at large n, Cu_n and Ag_n cluster geometries may differ significantly. If so, the low-energy isomers of Cu_n may not constitute good starting points for Ag_n geometry optimization. So, in the present study, we performed unbiased global optimizations by TSDS [48] for every n from 4 to 20.

Second, we wanted to find out what the effect of interactions may be on the geometric structures of Ag_n. It was found that adsorption of NO_2 and NO_3 causes important structural relaxations of silver clusters [139]. We wanted to see if other adsorbates can also affect Ag_n structures. We chose to study the simple atomic adsorbates Cl and Hg because they do not bind too strongly to Ag and they represent two different types of interactions. Cl atoms give a model for moderate ionic interaction and Hg atoms give a model for non-ionic and nonspecific interaction with Ag_n. We did computations for the species Ag_nCl_2 ($n = 3$ to 10, and 12) because they are relevant for experiments where Cl_2 is reacted with silver clusters. We studied Ag_nHg_m (n =5,6 and m =1 to 4) to see the effect of increasing the number of weakly bound ligands, and because calculations on larger silver clusters would be too time consuming. We think that the geometric structures of these simple species can give insight into possible geometries of silver clusters interacting with more complicated adsorbates or

with specific sites on a surface or in a host crystal. As we will show in the following sections, our calculations reveal big changes in the geometry of Ag_n upon interaction with Cl and Hg in some cases, and only minor changes in other cases. Generally, the interpretation of experiments on Ag_n clusters on a support (e.g., Al_2O_3), in matrix, or bound to ligands should not rely on the assumption of pure Ag_n geometries.

5.2 Review of literature

We begin with a review of previous work on the geometric structure of Ag_n clusters. Huanga and Watts did high-accuracy coupled-cluster calculations on Ag_3 [159]. They obtained an atomization energy of 2.62 eV (we found 2.58 eV), an angle of 67.7° (we obtained 69.8°) and two equivalent Ag-Ag bond lengths of 2.616 Å (we found 2.647 Å). Resonance Raman spectroscopy indicates that Ag_5 in solid Ar is a planar trapezoid [160] like the one shown in Fig. 5.1, and that the structure of Ag_7 in solid Ar is a tricapped tetrahedron [161]. However, another study by electron spin resonance showed that Ag_7 in a solid Ne matrix forms a pentagonal bipyramid (PBP) [162].

Many authors derived information about geometric structure by comparing time dependent DFT (TD-DFT) simulated spectra to experimental absorption spectra. Pereiro and Baldomir [136] assigned the structure of Ag_8 as the D_{2d} symmetry dodecahedron. Another study [120] of Ag_n in an Ar matrix ($n = 4$ to 14) gave evidence for the geometric structures shown in Fig.5.1 for $n = 4$ (rhombus), 5 (trapezoid), 7 (PBP), 13 and 14, and gave evidence for the pentagonal pyramid at $n = 6$ and coexistence of two Ag_8 structures, the one we found as the global minimum (GM, a

tetracapped tetrahedron) and the isomer we found to be 0.05 eV higher (D_{2d} dodecahedron). The same study [120] did not give definitive assignments for $n = 9$, 10, 11, and 12 but suggested that those spectra could be superpositions of signals coming from two or more isomers. A recent study of Ag_n is solid neon [163] confirms the structural assignments of Harb *et al.* [120]. For Ag_9, there is good evidence for the coexistence of several isomers (one of which is the GM of Fig.5.1) in a cold Ar matrix [164]. For Ag_{11}, the comparison of TD-DFT [165, 166] to experimental absorption spectra [117, 167, 168] suggests that the experiments see a PBP with two capping atoms above, and two capping atoms below, the equatorial plane (123'4'-PBP, the same structure that we show in Fig.5.1).

Structural predictions based on empirical potentials of the Gupta and Sutton-Chen type [133, 137] are at odds with DFT results and the assignments of experimental spectra. They show a compact growth sequence that maximizes coordination, including an octahedron at $n = 6$, capped PBP geometries with all of the capping atoms on the same side of the equatorial plane for $n = 9$ to 12, an icosahedron at $n = 13$, and a double icosahedron at $n = 19$. The structural predictions from a tight-binding study [169] — which includes 3D structures for n =5 and 6, icosahedra-based structures for n =11, 12, 13, 15 and 16, and a double icosahedron at $n = 19$ — are also at odds with DFT.

DFT calculations with various exchange-correlation functionals — the local density approximation of Vosko, Wilk and Nusair (VWN, or, VWN5) [134], the GGA of Becke, Perdew and Wang (BPW) [170], and the GGA functional PBE [135] — predict flat structures for $n = 3$ to 6 and polytetrahedral structures for $n = 7$ to

14, but no icosahedron-derived structure at or around $n = 13$. A more extensive study of Ag_n ($n = 3$ to 20) using PBE [138] and a set of low-energy structures previously obtained for Cu_n also found polytetrahedral structures. Another study with the GGA functional PW91 [140], gave similar results for n =3 to 15 but significantly different structures from n =16 to 20, including a hollow cage at $n = 18$ and a T_d pyramidal fragment of FCC crystal at $n = 20$. A many-body perturbation theory and coupled-cluster study of Ag_n (n =2,9) [153] reported ground-state geometries that agree with the ones we show in Fig. 5.1 except for Ag_8 (a D_{2d} dodecahedron) and Ag_9 (a capped D_{2d} dodecahedron).

5.3 Methods and computational details

Energies were calculated by DFT, with the meta-GGA exchange-correlation functional TPSS [60] and the LANL2 double-zeta (LANL2DZ) [171] basis sets implemented in the Gaussian 03 software package [172]. The TPSS functional was thoroughly tested [75] and the LANL2DZ basis set was used with success in numerous cluster studies. However, the TPSS/LANL2DZ level of theory is probably not sufficient to get accurate energies or bond lengths for Hg, or even Cl, interacting with Ag_n. In particular, we note that the Cl_2 bond energy (D_e, experimental value 2.51 eV) is calculated to be 1.61 eV by TPSS/LANL2DZ and 2.59 eV by TPSS/cc-pVTZ (cc-pVTZ is the correlation consistent triple zeta plus polarization basis set). But that does not matter for our study. We are only interested in qualitative changes in the geometry of Ag_n clusters upon binding to generic "ligands": (a) an ionic ligand

(Cl), and (b) a weakly interacting nonpolar ligand (Hg). For our purpose, Cl and Hg are only model systems that bind to Ag_n. The bond energies we obtained with the TPSS/LANL2DZ approximation are roughly 3.0 eV for Cl-Ag_n and 0.25 eV for Hg-Ag_n, and this is adequate for illustrating differences in geometries of Ag_n in cases of ionic, and weak, interactions.

Global optimization was done using TSDS [48] for singlet or doublet states for all species. The number of geometric structures and DFT energy evaluations for Ag_n in the global optimization stage was 30 $(n + 1)$. We used a sorting algorithm, based on energy and structural dissimilarity, to select the N_{best} best of those 30 $(n + 1)$ structures, with $N_{best} = 15$ or 20. Then we carried out local optimization for those N_{best} structures.

We used the following geometric descriptors for TSDS optimization: the mean coordination of Ag atoms c, the root-mean square deviation from the mean of atomic coordinations, $rmsdc$, and two descriptors obtained from the moments of inertia; asphericity (ζ) and shape (η) Note that $\eta < 0$ for oblate clusters and $\eta > 0$ for prolate clusters (see page 32).

5.4 Results and discussion

5.4.1 Silver clusters: structures

The silver cluster GM structures that we found, using the TPSS functional, are displayed in Fig. 5.1. They generally agree with GM found in previous DFT com-

putational studies that used the VWN [134] and PBE [138] functionals. The GM structures are planar and grow by addition of triangles for $n = 3$ to $n = 6$ (Ag_3 forms a triangle with one angle equal to 70°). The GM for $n > 6$ are polytetrahedral but, unlike Lennard-Jones (LJ) clusters, they do not maximize the number of nearest-neighbour pairs (defined as the number of interatomic distances smaller than $1.2R_{NN}$, or, 3.47 Å for silver clusters) except for $n = 7$ which is a pentagonal bipyramid (PBP), and $n = 9$. In particular, the Ag_{13} GM has only 38 nearest-neighbours compared to 42 for the icosahedron (the GM of LJ_{13}). The first 13-atom icosahedral unit appears only at $n = 17$.

We rationalize the equilibrium structure of the GM of Ag_n as the result of two competing physical effects: (a) minimizing the surface tension, or, surface area, which tends to *maximize the number of nearest neighbours*; (b) achieving a nuclear framework with an *optimal shape* for a given valence electron count, as predicted by the ellipsoidal jellium model (EJM). There is, maybe, a third structural principle at play: geometries where *all, or most, of the atoms have nearly the same coordination* (ie, with a low *rmsdc*) seem to be favored [134]. Table 5.1 shows the number of nearest-neighbour pairs in the GM of Ag_n and of Lennard-Jones clusters. This number is lower in Ag_n, but it is never very far from what it is in LJ_n. Table 5.1 also shows the shape parameter η of the Ag_n GM, and the shape prediction of the EJM represented like this: 0 means spherical ($\eta \approx 0$), + means prolate ($\eta > 0$), and − means oblate ($\eta < 0$). Remarkably, the DFT optimized shapes and EJM predicted shapes agree in every case except $n = 5, 9, 13$. Further, the three nuclearities for which the EJM predicts a spherical shape (n =8, 19, 20) are those for which DFT calculations yield

the smallest absolute values of η (0.00, -0.05, 0.00) and the smallest ζ (0.000, 0.021 and 0.003, the next smallest ζ is for Ag_{18}, it is 0.043, and the average ζ for $n = 4$ to 20 is 0.176).

We will now briefly describe cluster isomers. The energy of the lowest isomers are given in Table 5.2, last column. A few comments are in order. We calculated free energies at 298 K in many cases. We compared the isomer relative energies to isomer relative *free* energies in 21 cases and found a mean absolute deviation of 0.020 eV between the two sets of numbers. So, free energies might give a different ordering and different GM predictions in some cases (e.g., Ag_9, Ag_{18}). Errors on relative energies due to approximations in the treatment of exchange-correlation are surely bigger than 0.02 eV. Further, the temperature of gas-phase clusters is often unknown. So, we chose to report zero Kelvin energies for simplicity. We consider that our predicted GM are only tentative in cases where isomers are found 0.1 eV or closer in energy ($n = 8, 9, 12, 16, 17, 18$), and generally, conclusions about trends and general aspects of structures and energies are more robust than any conclusion about the structure or energy of a specific cluster species.

The GM of Ag_3 has an angle of 70°: the first isomer has an angle of 113°. The first isomers for $n = 4$ to $n = 10$ are as follows: a Y-shaped structure for Ag_4; a D_{3h} trigonal bipyramid (TBP) for Ag_5; a C_{5v} pentagonal pyramid for Ag_6; a C_{3v} tricapped pyramid for Ag_7 (this structure was assigned to Ag_7 trapped in a cryogenic matrix by resonance Raman spectroscopy [161]); a D_{2d} distorted bicapped octahedron, or dodecahedron, for Ag_8; for Ag_9 we have a C_s bicapped PBP with capping atoms on either side of the equatorial plane of the PBP at 0.039 eV, and a C_s capped

dodecahedron at 0.054 eV; and, for Ag_{10}, a tricapped PBP with capping atoms at triangular sites 1, 2, and 3' (unprimed and primed numbers denote positions above and below the equatorial plane). An interesting other isomer of Ag_{10}, found at +0.296 eV, is the D_{4d} symmetry doubly capped square antiprism.

The first isomer (0.147 eV) of Ag_{11} is different from the rest: it has a D_{3h} symmetry 9-atom core made of a trigonal prism with three face-capping atoms and two additional capping atoms, with overall C_s symmetry. The GM of Ag_{12} is a 5-capped PBP which we denote 1234'5'-PBP: the first isomer of Ag_{12} is just a distorted version of that GM. The first isomers of Ag_{13}, Ag_{14}, and Ag_{15} are oblate and polytetrahedral, and similar to their respective GM. The two low isomers of Ag_{16}, like the GM of Ag_{16}, consist of an icosahedron with one missing peripheral atom, to which four capping atoms are attached. The GM and two isomers of Ag_{16} differ only in the positions of those four capping atoms. The first isomer of Ag_{17} is a 4-capped icosahedron. The first isomer of Ag_{18} is practically degenerate with the GM (+0.013 eV). It is a double icosahedron with a missing axial atom, the same structure as for the GM of a Lennard-Jones 18-atom cluster. Unlike the GM of Ag_{18}, it is strongly prolate. The first isomer of Ag_{19} is a quasispherical multiply capped icosahedron. The first isomer of Ag_{20} is like the GM, but with the two capping atoms further apart.

5.4.2 Silver clusters: energies

The atomization energies $AE\ (n)$ and cohesive energies $CE\ (n) = AE\ (n)/n$ of Ag_n are shown in Table 2. We fitted *cohesive energies* to this function:

$$CE_{fit}\ (n) \quad = \quad a + bn^{-1/3} \tag{5.1}$$

where a is the bulk cohesive energy and $bn^{-1/3}$ is a surface correction (the corresponding correction to the atomization energy is $bn^{2/3}$, and $n^{2/3}$ scales as the surface area). The fit yields $a = 2.9089$ eV/atom, which is very close to the experimental bulk cohesive energy of silver (2.95 eV/atom), $b = -2.8432$ eV $\mathrm{n}^{-2/3}$, and a root-mean square error of 0.034 eV/atom (3.4% of the range in cohesive energies).

Fig. 5.2 shows the differences $\Delta\ (n) = CE\ (n) - CE_{fit}\ (n)$. A positive value of $\Delta\ (n)$ indicates a cluster size that is stable *relative to other sizes in general*. Fig. 5.3 gives the second difference in energy $\Delta_2\ (n) = AE\ (n+1) + AE\ (n-1) - 2AE\ (n)$. A negative value of $\Delta_2\ (n)$ indicates a cluster that is stable *relative to the two clusters that are immediate neighbours in size*.

The relative stability of clusters as a function of size is often discussed on the basis of $\Delta_2\ (n)$. Here (Fig: 5.3), $\Delta_2\ (n)$ shows a clear pattern of even-odd oscillations in stability ($n = 16$ excepted), something that has been observed in every previous study of silver clusters. The reason is simple: spin subshell closing confers stability.

The $\Delta\ (n)$ curve (Fig. 5.2) is more interesting. It shows enhanced stability for three consecutive sizes, $n = 6$, 7, and 8, something that a $\Delta_2\ (n)$ curve could never show. We explain this pattern as follows. The stability of Ag_6 probably has to do with the fact that six electrons ($N_e = 6$) constitute a closed-shell for a 2D

cluster. Notice the large HOMO-LUMO gap of Ag_6, 2.29 eV (Table 5.2). Extra stability was also found for Au_6 [173]. The stability of Ag_7 can be understood from its geometric structure with many nearest neighbours ($n = 7$ is a minor magic number in polytetrahedral clusters). As for Ag_8, it has a closed electronic shell according to the 3D jellium model, and this is consistent with its very big HOMO-LUMO gap (2.403 eV, Table 5.2). To sum up, among all the clusters we studied, Ag_6, Ag_7, and Ag_8 stand out as particularly stable (Fig. 5.2), with Ag_6 and Ag_8 having by far the largest HOMO-LUMO gaps, and Ag_7 having a PBP structure that comes closest to what we might call a closed geometric shell.

The electron count, prolate shape, and D_{2d} symmetry of Ag_{10} suggest that it is a cluster analogue of the very stable N_2 molecule [174] and this may account for its relative stability (Fig.5.2). There is an anomaly in Δ (n) and Δ_2 (n) at $n = 16$. It is unclear whether this is a genuine result or a failure to locate the GM of Ag_{16}. But, interestingly, Ag_{16} stands out in experiments for having a large NH_3 binding enthalpy (15.9 $\pm$ 1.0 kcal/mol) and low (or no) NH_3 surface diffusion [175]. In contrast, the same experiments gave a binding enthalpy of 9.8 $\pm$ 1.0 kcal/mol for $Ag_{10}NH_3$ and strong evidence that NH_3 diffuses freely at room temperature on Ag_{10}. Our GM structure for Ag_{16} shows a 5-fold (or maybe 6-fold) coordination site (see Fig: 5.1, bottom part of the Ag_{16} structure), the site of the missing Ag atom that would complete an icosahedron. Among our GM, only Ag_{19} and Ag_{20} have such a site, but these clusters are comparatively more stable than Ag_{16} (Fig: 5.2) and have a bigger HOMO-LUMO gap than Ag_{16} (Table 5.2). It is tempting to conclude that the combination of a relatively high energy, low HOMO-LUMO gap, and presence of a

5-fold binding site explains the observed strong bonding in $Ag_{16}NH_3$. Note also that the surface of Ag_{10} (two fused PBP at right angles that share a tetrahedron) presents only 3-fold coordination sites: easy NH_3 diffusion on such a surface is plausible.

5.4.3 Ag_nCl_2 clusters: structures and energies

The GM that we found for n=3 to 10 and $n = 12$ are shown in Fig: 5.4. Comparing to Fig. 5.1, we see that binding Cl_2 to Ag_n preserves the GM structures in cases n =3, 4, and 9, and changes the structure in all other cases. Upon binding to the Ag_5 GM, the two Cl atoms transform it to an isomer that is 0.47 eV higher. We define the distortion energy, $E_{distortion}$, as the difference between the energy calculated for Ag_n in the geometry it has inside a complex Ag_n—X (X=Cl_2 or Hg_m), and the energy of the GM of Ag_n. For Ag_5Cl_2, $E_{distortion}$ is approximately 0.47 eV. For n = 6, 7, and 8, $E_{distortion} \approx$ 0.81, 0.88 and 0.19 eV, respectively. The binding energies of two Cl atoms to the various Ag_n clusters vary roughly between 6 and 7 eV (see Table 5.3). It is not surprising that such a strong interaction can induce distortion energies of up to 1 eV in some cases and that this is sufficient to change completely the Ag_n geometry.

We could not find any correlation between the shapes of Ag_nCl_2 GM structures and EJM predictions associated with electron counts of either n or $(n-2)$. In Ag_nCl_2, electronic shell closing effects are probably too small, in comparison to Cl-Ag interactions, to matter. What is clear from Fig. 5.4 is that Cl atoms always bind to two Ag atoms in a bridging geometry, and the Cl atoms are always far apart. There is

a simple explanation: there is an ionic contribution to the Ag-Cl interaction, Cl atoms acquire negative charges (the Mulliken charges on Cl atoms vary between -0.18 and -0.30 depending on the clusters), and coulombic repulsion favors geometries with large Cl-Cl distances.

There are strong variations in the calculated dipole moments of Ag_nCl_2. Cl atoms bear significant negative charges, so the dipole could be quite large if the two Cl were on the same side of the Ag_n cluster. The closest to that situation is Ag_4Cl_2 (dipole moment of 7.57 D). But coulombic repulsion of the Cl atoms often puts them far apart and on either side of the cluster. In a limit case, this could give a zero dipole. The closest to that is $Ag_{12}Cl_2$ which has a dipole of only 1.40 D.

The dissociation energies (DE in Table 5.3) are smallest for n =5, 6, 7, and 8. In the case of $n = 5$ this can be attributed to the large distortion energy in going from a 2D geometry to a 3D geometry. For n =6, 7, 8 we can also invoke the distortion energy or, more simply, the fact that Ag_6, Ag_7, and Ag_8 are, relatively speaking, the most stable clusters in the Ag_n series. The DEs of Table 5.3 are all much larger than the experimental bond energy of Cl_2, 2.48 eV, which suggests that Cl_2 should dissociate easily on Ag_n clusters.

5.4.4 Ag_nHg_m clusters: structures and energies

The GM structures are shown in Fig. 5.5. The Ag_5 structure is unchanged by the interaction with one Hg atom, and distorts slightly (it buckles) upon interaction with two or more Hg atoms. The Ag_6 structure changes qualitatively, from a 2D triangle

to a pentagonal pyramid, upon binding to one or more Hg atoms. Interestingly, there is evidence that Ag_6 adopts the pentagonal pyramid structure in an Ar matrix [120]. In our calculations for bare Ag_6, the pentagonal bipyramid is 0.18 eV higher than the GM (flat triangle), so 0.18 eV is a lower bound to the distortion energy of the Ag_6 unit in Ag_6Hg_m. The actual distortion energies are given in Table 5.4.

As expected, Hg-Ag interactions are much weaker than Cl-Ag interactions. The binding energy of additional Hg atoms is nearly constant, 0.25 eV for Hg—Ag_5Hg_{m-1} and 0.22 eV for Hg—Ag_6Hg_{m-1}, see Table 5.4. The exception is the bond energy of the highly coordinated Hg atom in Hg—Ag_6 which is double that, 0.465 eV. In fact, the two strongest Hg interactions, Hg—Ag_5Hg (0.305 eV) and Hg—Ag_6 (0.465 eV), are found for the two most highly coordinated Hg atoms. Yet, Hg atoms prefer to bind at singly coordinated ("atop") sites in many cases. Intuitively, distortion energies normally should not be larger than dissociation energies (although that is possible). This is what we observe.

The case of Ag_6Hg_m illustrates a possible pitfall when using the GM of a metal cluster like Ag_n as the initial guess for geometry optimization of some metal-ligand complex Ag_n—X. The present calculations, and previous studies [134], often show many isomers within a few tenths of eV of the GM. Therefore, even a weak Ag_n—X interaction (few tenths of eV) could lead to a complete structural reorganization as seen with Ag_6Hg_m. The distortion energies of Ag_6Hg_m are not very large, only 0.24 eV. However, since the flat triangle and the pentagonal pyramid are topologically very different, there is probably no low-energy pathway for rearranging one into the other. So, starting a local geometry optimization with Hg bound anywhere on a flat

triangular Ag_6 will almost surely not lead to the GM of Ag_6Hg. On the other hand, a hypothetical experiment where Ag_6 forms first and then interacts weakly with Hg would not lead to the GM of Ag_6Hg either and, trying to model such an experiment, it would make sense to do a local optimization where the initial guess has a Hg atom attached to a site of the flat triangular Ag_6 GM. Further, note that positioning one, two, three, or four Hg atoms at various sites of the rhombus Ag_5 GM might very well produce the true GM of Ag_5Hg_m of Fig. 5.5.

5.5 Concluding remarks

The predicted GM structures of Ag_n ($n = 3$ to 20) obtained here with a meta-GGA functional (TPSS) are in very close agreement with previous results obtained with the GGA functional PBE [138] and also agree well (for $n = 4$ to 12) with earlier work that used the local spin density functional VWN [134]. The Ag_n clusters are 2D for $n = 3$ to 6, polytetrahedra that nearly maximize the number of neighbours for $n > 6$, and they adopt (with the exception of n =5, 9, 13) a shape consistent with predictions from the simple ellipsoidal jellium model. The sizes $n = 6$, 7, and 8 stand out as relatively more stable than the rest. This is due to an electronic effect for $n = 6$ and 8 (Ag_6 and Ag_8 have big HOMO-LUMO gaps), and it is due to the coincidence of an optimal shape (oblate with 7 electrons) and an atomic closed shell at $n = 7$. We can see in Fig. 5.6 that the PBP ($n = 7$, $n^{-1/3} = 0.52$) has a large mean coordination compared to other clusters. On the other hand, Ag_{16} stands out as particularly *unstable* (see Fig. 5.2 and Fig. 5.3) and this, along with the presence

of a high-coordination site, may explain the experimentally observed strong bonding of NH_3 to Ag_{16} [175].

Low-lying isomers are predicted for Ag_3 (0.044 eV), Ag_8 (0.050 eV), Ag_9 (0.039 and 0.054 eV), Ag_{12} (0.044 eV), Ag_{16} (0.053 and 0.072 eV, both of which also possess the high-coordination site mentioned above), Ag_{17} (0.086 eV), and Ag_{18} (0.013 eV). Other isomers are found 0.10 eV or higer relative to the GM.

Cl atoms bind to Ag_n with a binding energy of roughly 3.0 eV. Upon binding to two Cl atoms, the geometry of Ag_n: (*i*) changes completely in some cases (n =5, 6, 7) with a distortion energy as large as 0.88 eV; (*ii*) changes somewhat in other cases (n =8, 10, 12), with distortion energies in the vicinity of 0.2 eV; and (*iii*) stays essentially unchanged for n =3, 4, and 9. The Hg atom-to-Ag_n cluster binding energy is roughly 0.25 eV. Upon binding to Hg atoms, the geometry of Ag_5 changes slightly, but the geometry of Ag_6 changes completely.

On the whole, our results illustrate a few things that one should consider before modeling a metal cluster-ligand complex. Obviously, first one should try to assess whether the experiment one attempts to model produces the GM of the cluster-ligand complex species, or whether it produces a simple association complex of the ligand with the cluster's GM. The latter case is simpler. In the former case, one could perform full global optimization of cluster-ligand species as we did here. Alternatively, one could adopt the following procedure. *First*, one would determine an approximate energy of cluster-ligand interaction (what we call DE in Tables 5.3 and 5.4) and then try to find a representative set of metal cluster isomers that fall roughly in that energy range. *Second*, one would examine the various binding sites on the various

isomers and determine, with a series of local optimizations, the type of sites that are energetically most favorable. *Finally*, guided by a few calculated site-dependent interaction energies, and the energies of isomers relative to the GM, one could set up a prioritized list of isomers and sites likely to yield the lowest energies upon optimization.

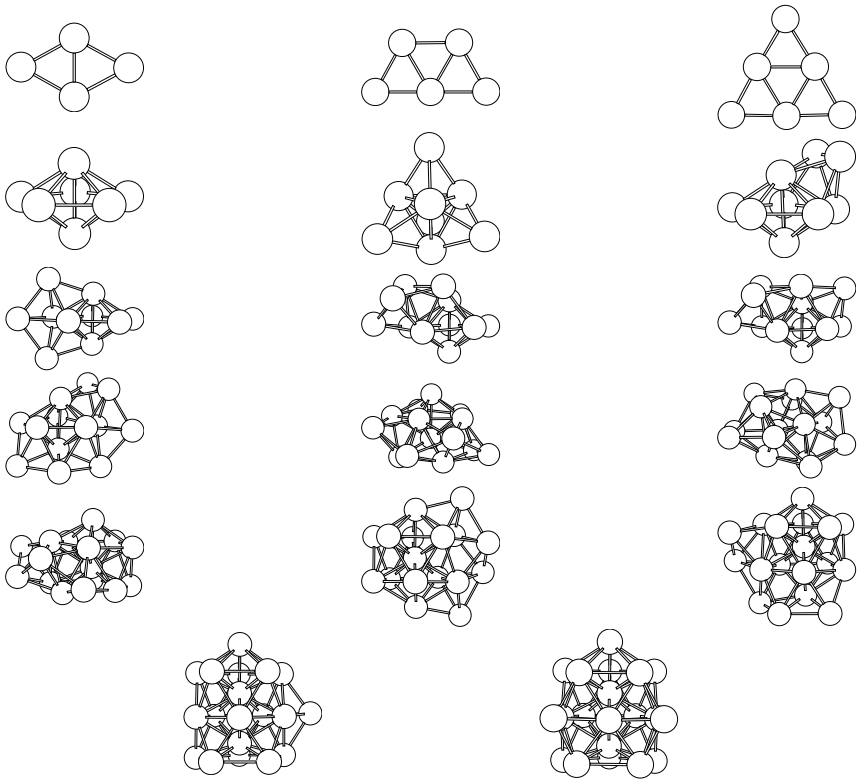

Fig. 5.1. Global minima of Ag_n clusters, n =4 to 10.

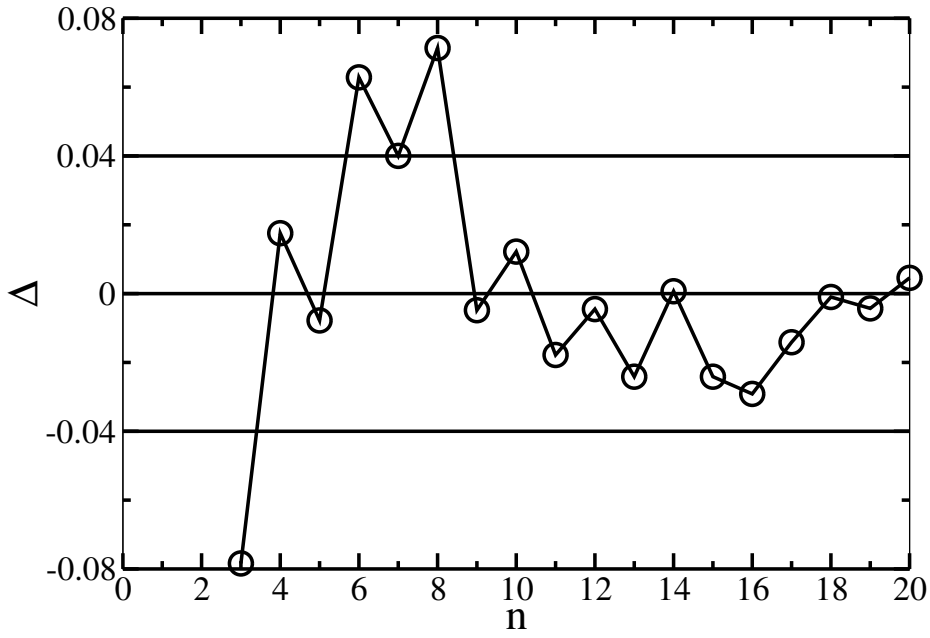

Fig. 5.2. Difference between DFT and fitted cohesive energies (in eV/atom) of Ag_n.

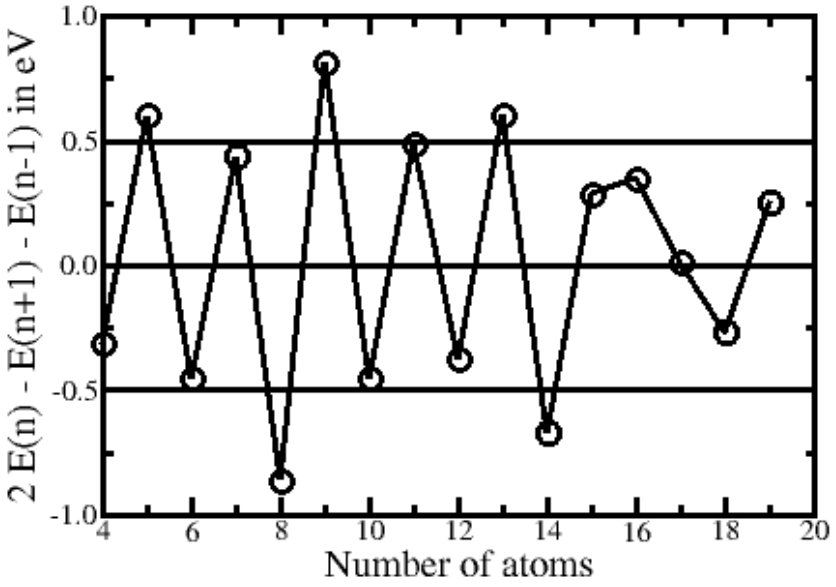

Fig. 5.3. Second difference in atomization energies (in eV) of Ag_n

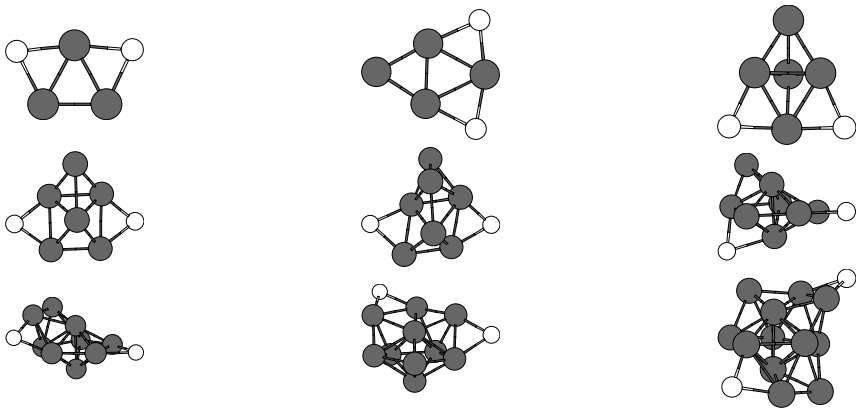

Fig. 5.4. Global minima of Ag_nCl_2 clusters for n =3 to 10 and $n = 12$.

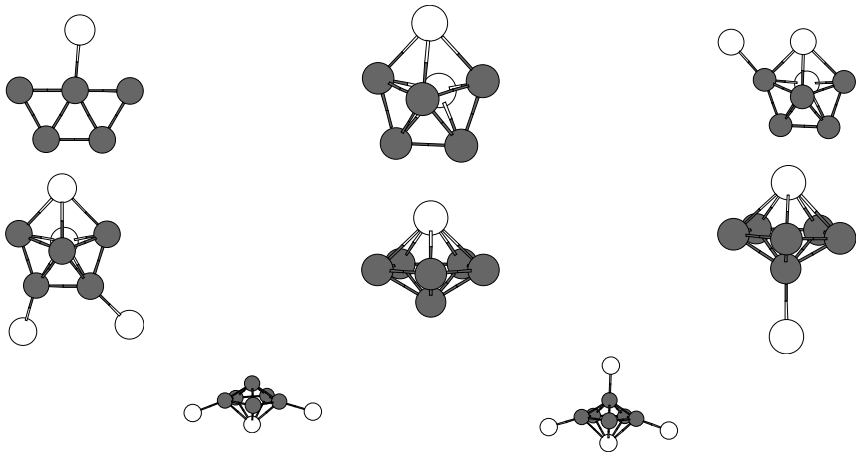

Fig. 5.5. Global minima of Ag_nHg_m clusters for n =5, 6 and m =1 to 4.

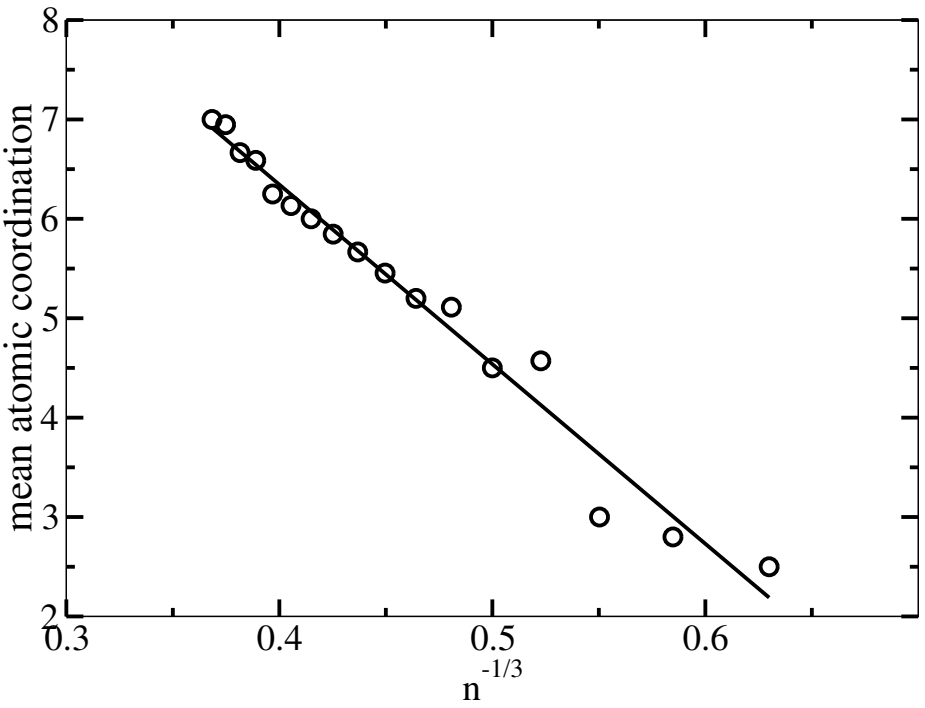

Fig. 5.6. Mean atomic coordination c of the Ag_n GM clusters as a function of $n^{-1/3}$.

The straight line is a fit: $c = c_0 + bn^{-1/3}$ $(c_0 = 13.6,\ b = -18.1)$

Table 5.1: Number of nearest-neighbours (NNN) for silver and Lennard-Jones clusters, shape parameter of the global minima of Ag_n, and shape predicted by the EJM (− means oblate, + means prolate, 0 means quasispherical).

n	NNN (Ag_n)	NNN (LJ_n)	η (Ag_n)	EJM
4	5	6	0.32	+
5	7	9	0.19	−
6	9	12	−0.50	−
7	16	16	−0.35	−
8	18	19	0.00	0
9	23	23	−0.07	+
10	26	27	0.47	+
11	30	31	0.22	+
12	34	36	0.09	+
13	38	42	−0.08	+
14	42	45	−0.36	−
15	46	49	−0.23	−
16	50	53	−0.16	−
17	56	57	−0.11	−
18	60	62	−0.19	−
19	66	68	−0.05	0
20	70	72	0.00	0

Table 5.2: Atomization energies and cohesive energies of the GM of Ag_n, their HOMO-LUMO gaps, and the energies of the lowest cluster isomers and any other isomer with a relative energy of 0.1 eV or less (all energies in eV).

n	$AE\ (n)$	$CE\ (n)$	HL gap	E_{isomer}
3	2.577	0.8591	0.382	0.044
4	4.541	1.1354	0.916	0.235
5	6.192	1.2384	1.303	0.474
6	8.442	1.4071	2.287	0.184
7	10.238	1.4626	1.285	0.183
8	12.469	1.5587	2.403	0.050
9	13.835	1.5372	0.457	0.039, 0.054
10	16.014	1.6014	1.037	0.198
11	17.739	1.6126	0.667	0.147
12	19.950	1.6625	0.920	0.044
13	21.783	1.6756	0.462	0.117
14	24.219	1.7299	1.147	0.098
15	25.979	1.7319	0.467	0.111
16	28.023	1.7514	0.409	0.053, 0.072
17	30.414	1.7890	0.371	0.086
18	32.814	1.8230	0.627	0.013
19	34.943	1.8391	0.600	0.158
20	37.321	1.8660	1.010	0.291

Table 5.3: Atomization energies of Ag_nCl_2 GM, dissociation energy (DE) for Ag_nCl_2 $\rightarrow$ Ag_n + Cl + Cl (all energies in eV), and dipole moment in Debye. The calculated binding energy (D_e) of Cl_2 is 1.607 eV.

n	$AE\ (n)$	$DE\ (n)$	dipole
3	9.006	6.43	4.63
4	11.581	7.04	7.57
5	12.481	6.29	6.69
6	14.733	6.29	5.02
7	16.330	6.09	1.66
8	18.611	6.14	1.79
9	20.430	6.60	4.97
10	22.908	6.89	4.40
12	26.542	6.59	1.40

Table 5.4: Atomization energies of Ag_nHg_m GM, dissociation energy (DE) and distortion energy ($E_{distortion}$) for $Ag_nHg_m \rightarrow Ag_n + m$ Hg (all energies in eV), and dipole moment in Debye. The calculated dimer bond energies (D_e) are: Ag_2, 1.730 eV; Hg_2, 0.0094 eV; and AgHg, 0.257 eV.

n	m	AE	DE	$E_{distortion}$	dipole
5	1	6.451	0.259	0.003	1.13
5	2	6.756	0.564	0.376	0.92
5	3	6.993	0.801	0.320	2.20
5	4	7.242	1.050	0.338	1.72
6	1	8.907	0.465	0.234	0.42
6	2	9.132	0.690	0.254	0.87
6	3	9.345	0.903	0.227	1.30
6	4	9.564	1.122	0.240	0.93

Chapter 6

Trends in Structure and Stability of Pure and Mixed Clusters $\mathbf{Li}_x\mathbf{Mg}_y\mathbf{Al}_z$ $(x+y+z \leq 8)$.

6.1 Introduction

There have been many studies of elemental clusters X_n, using experiment and theory. They show nontrivial size-dependent structural, chemical and spectroscopic properties [193, 194, 195]. Among theoretical studies of clusters of simple metals, we note, in particular those on Li_n [196, 197, 198, 199, 200], Al_n [201, 202, 203, 204], and Mg_n [205, 206, 207, 208], where n is varied. More recently, several mixed metal clusters have been studied [209, 210, 211, 212, 294, 214]. The size of the chemical space spanned by elemental clusters X_n is fairly small. With binary and ternary clusters, the chemical space is much bigger, and so are the chances of discovering important new cluster species. A range of properties may be accessible by varying the size, composition, and morphology of binary or ternary clusters [215, 216, 217, 218, 219, 220].

For instance, the optical absorption of Ag_xAu_y clusters varies with composition and morphology and can be tuned by laser irradiation annealing [221, 222, 223, 224].

Here we report a study, by DFT and GO, of all possible elemental, binary, and ternary clusters $Li_xMg_yAl_z$ in the size range from 5 to 8 atoms. Our goal is twofold. First, we wish to show the trends in the geometry and stability of these clusters and understand better physical factors that govern them. Second, we want to identify those clusters that are particularly stable or possess high symmetry. We look at two aspects of cluster stability. The first is thermodynamic stability as indicated, for instance, by a relatively large AE. However, AE's of clusters with different compositions can not be compared directly. In the next section we describe a methodology in which a fit to AE's is done and is used for making comparisons of cluster stability. The second aspect of stability is the highest occupied molecular orbital (HOMO) to lowest unoccupied molecular orbital (LUMO) gap E_g. A large E_g is often indicative of chemical stability. The maximum hardness principle (MHP) also implies that E_g correlates with conformational and thermodynamic stability [187, 189, 188].

The next section shows details of computational methods we used. Results are presented and discussed in section 6.3. The main findings are summarized in section 6.4.

6.2 Computational details

We applied Kohn-Sham density functional (KS-DFT) with the Gaussian09 [49] software with the non empirical gradient corrected exchange-correlation functional of

Perdew, Burke and Ernzerhof [59] (PBE) and the LANL2DZ effective core potential (ECP) and basis set [225, 226]. We performed GO by a modified version of TSDS [48] using a relative index of thermodynamic stability (RITS).

6.2.1 Relative Index of Thermodynamic stability

We fit the atomization energies of all 130 clusters using a geometry independent model. The fitted atomization energies, AE_{fit}, are obtained with a simple formula,

$$AE\ (C_j, X_j) = AE_{fit}\ (C_j) + e_j = \sum_i N_{j,i} U_c\ (Z_i) + e_j \tag{6.1}$$

where e_j is the fitted model error on the j^{th} energy. The adjustable parameters of the fit, $U_c\ (Z_i)$, are interpreted as mean cohesive energies of atoms-in-molecules for element i for a given data set. There is a simple physical interpretation for the species $Li_aMg_bAl_c$ with the lowest (most negative) RITS: of all the possible ways of arranging N_a atoms of Li, N_b atoms of Mg, and N_c atoms of Al into clusters chosen from the dataset of 130 clusters, the lowest energy way is N clusters of $Li_aMg_bAl_c$. In general, the RITS of a cluster $Li_xMg_yAl_z$ can be interpreted as the energy of that cluster relative to a weighted mean of all other cluster energies in the data set, where the weights are such that the mean number of Li, Mg and Al atoms are x, y and z, respectively. In this sense, the RITS gives a "fair comparison" of a cluster's energy to other cluster energies. This allows, among other things, to optimize both chemical composition and geometric structure in a single run.

6.2.2 Global optimization

We use an optimization strategy where many cluster species are optimized at once. One advantage of this strategy is that, once a stable cluster $Li_xMg_yAl_z$ is found, it can serve as a starting point for making several modified clusters of the same, or similar, chemical composition, by addition, or removal, or displacement of atoms. This is good because clusters with similar chemical compositions often have similar minimum energy geometries.

We limit the range of possible compositions by specifying: (a) a list of allowed elements $Z_1, Z_2, \ldots, Z_k$; (b) the minimum and maximum numbers of atoms for each element, $N_{min,1}, N_{max,1}, N_{min,2}, N_{max,2}, \ldots, N_{min,k}, N_{max,k}$; and (c) minimum and maximum total number of atoms, N_{min} and N_{max}. In this work, we did two separate runs. In the first run we considered only elemental A_x clusters and bimetallics A_xB_y. In the second run we allowed ternary clusters $Li_xMg_yAl_z$.

To avoid getting unphysical configurations we use standard values of atomic radius $r(Z)$ for the elements and calculate pseudo-distances between pairs of atoms: $d_{ij} = r_{ij}/(r(Z_i) + r(Z_j))$, where r_{ij} is the distance between the two atoms, $r(Z_i)$ and $r(Z_j)$ are the atomic radii of the two elements, and d_{ij} is dimensionless and near unity for nearest-neighbors. All the configurations generated in our optimization satisfy constraints of the form $d_{ij} \geqslant 1$. The objective function $F\ (C, X)$ that we minimized combines the RITS and the HOMO-LUMO gap:

$$F(C, X) \quad = \quad R(C, X) - E_g(C, X) \tag{6.2}$$

This way, the search for the global minimum (GM) structure is more thorough for

cluster species that have a smaller R and bigger E_g. A possible drawback of this method is that the search may be insufficient for some cluster species, particularly those with a relatively large F. There are two possible advantages. *First*, finding the GM gets increasingly difficult as the number of atoms N in clusters increase, so it is advisable to perform more optimization cycles as N increases. The larger clusters have a smaller surface-to-volume ratio and this almost invariably produces smaller (more negative) R. Therefore, by optimizing F we spend more optimization cycles on large clusters than on small ones, as we should. *Second*, minimizing F implies that the search for the GM of stable (low F) cluster species will be more thorough than for unstable clusters species, and the likelihood of missing the GM of stable cluster species will be smaller. This is desirable because we are primarily interested in clusters with exceptional stability.

More details can be found in chapter 4 and Ref. [111].

We did two optimization runs. The first run was for elemental and binary clusters only. It had $M = 500$ and $K = 15200$, so 15700 GO cycles in total, followed by typically 5 to 20 local optimizations for every cluster species. The second run also included ternary clusters and it had $M = 200$ and $K = 34000$, so 34200 GO cycles in total, followed by 5 to 20 local optimizations for every cluster species.

6.3 Results and discussion

6.3.1 Structures

The lowest energy minima we found for every cluster species are shown in Fig 6.1 arranged in increasing order of RITS. Of the 130 cluster species, 21 have five atoms, 28 have six, 36 have seven, and 45 have eight; 12 are elemental clusters, 66 are binary (22 LiMg, 22 LiAl, 22 MgAl) and 52 are ternary.

Some trends and patterns are clearly apparent. In binary and ternary clusters, Al atoms are usually closest to the geometric center of the cluster and have the highest coordination, whereas Li atoms are usually furthest from the center and have the lowest coordination. This is consistent with the experimental surface energy ordering of the elements [190]: Al ($1.143\,\mathrm{J\,m^{-2}}$, $1.160\,\mathrm{J\,m^{-2}}$)); Mg ($0.785\,\mathrm{J\,m^{-2}}$, $0.760\,\mathrm{J\,m^{-2}}$); and Li ($0.522\,\mathrm{J\,m^{-2}}$, $0.525\,\mathrm{J\,m^{-2}}$). As a rule, Li-rich and Mg-rich clusters often display polytetrahedral structures, and Al-rich clusters often display trigonal prisms (but pure Al_n clusters do not). Planar GM structures are uncommon and show up only in the smallest (5-atom and 6-atom) clusters. Some symmetrical motifs are common to many geometries: the 6-atom trigonal prism (e.g., Li_2Al_6 $R = -1.65$), the 8-atom dodecahedron (e.g., Mg_4Al_4, $R = -1.23$) which is closely related to a bicapped octahedron, the 7-atom pentagonal bipyramid (e.g., Li_3Mg_4Al, $R = -0.44$ and Mg_7, $R = 0.00$), the 6-atom octahedron (e.g., Li_4Mg_2, $R = -0.07$), the 5-atom trigonal bipyramid (e.g., $LiMg_3Al$, $R = 0.81$), and the 6-atom planar triangle (e.g., Mg_3Al_3, $R = 0.88$). However, many geometries are best described as distorted or amorphous and lack any symmetry. This is surely due in part to the mismatch in atomic radii (1.51 Å for Li,

1.60 Å for Mg, 1.43 Å for Al) and electronic structure of the three elements. Elemental clusters have somewhat higher symmetry and more crystal-like structures, see the 12 clusters at $R = -0.33, -0.09, 0.00, 0.20, 0.37, 0.39, 0.43, 0.57, 1.01, 1.42, 1.54, 1.68$ (Fig 6.1). The RITS values of elemental clusters show that they are, on average, less stable than mixed clusters. This, and the irregular geometries of mixed clusters, shows how difficult structure predictions are — and how important unbiased global optimization is — in computational studies of binary and ternary clusters. The 130 putative GM we found display a great variety of, mostly low-symmetry, structures.

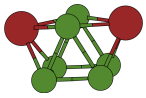

Li_2Al_6 (-1.65)

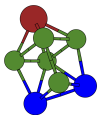

$LiMg_2Al_5$ (-1.46)

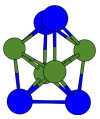

Mg_4Al_4 (-1.23)

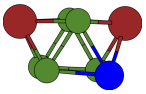

Li_2MgAl_5 (-1.08)

$LiMgAl_6$ (-1.04)

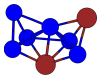

Li_3Al_5 (-0.90)

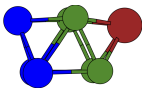

$LiMg_3Al_4$ (-0.89)

Li_5Al_3 (-0.87)

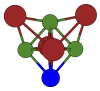

Li_4MgAl_3 (-0.82)

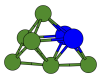

Mg_3Al_5 (-0.82)

$Li_2Mg_2Al_4$ (-0.77)

Li_4Al_4 (-0.76)

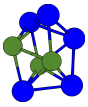

Mg_5Al_3 (-0.71)

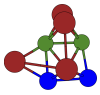

$Li_4Mg_2Al_2$ (-0.70)

$Li_3Mg_2Al_3$ (-0.67)

Li_3MgAl_4 (-0.63)

$LiAl_7$ (-0.60)

$Li_2Mg_3Al_3$ (-0.58)

Li_2Mg_5Al (-0.53)

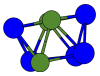

Mg_6Al_2 (-0.50)

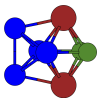

$Li_2Mg_4Al_2$ (-0.50)

Mg_2Al_6 (-0.48)

$LiMg_4Al_3$ (-0.46)

Li_5MgAl_2 (-0.46)

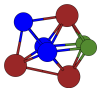

$Li_3Mg_3Al_2$ (-0.45)

Li_3Mg_4Al (-0.44)

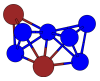

Li_2Mg_6 (-0.40)

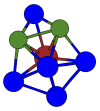

$LiMg_5Al_2$ (-0.39)

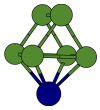

$MgAl_6$ (-0.38)

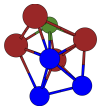

Li_4Mg_3Al (-0.37)

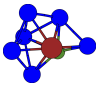

$LiMg_6Al$ (-0.36)

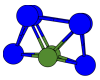

Mg_7Al (-0.34)

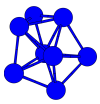

Mg_8 (-0.33)

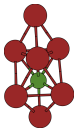

Li_7Al (-0.31)

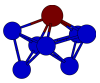

$LiMg_7$ (-0.30)

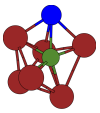

Li_6MgAl (-0.27)

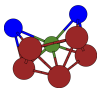

Li_5Mg_2Al (-0.26)

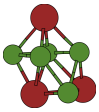

Li_3Mg_5 (-0.23)

Li_3Al_4 (-0.22)

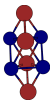

Li_4Mg_4 (-0.20)

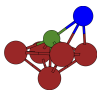

Li_5MgAl (-0.19)

Li_6Al (-0.13)

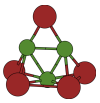

Li_5Mg_3 (-0.13)

Li_4Al_3 (-0.10)

Al_8 (-0.09)

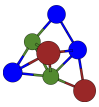

$Li_2Mg_3Al_2$ (-0.08)

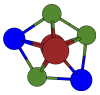

$Li_2Mg_2Al_3$ (-0.08)

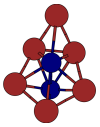

Li_6Mg_2 (-0.08)

$Li_2Mg_2Al_2$ (-0.08)

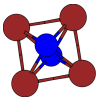

Li_4Mg_2 (-0.07)

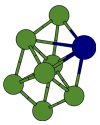

$MgAl_7$ (-0.06)

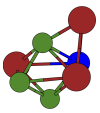

Li_3MgAl_3 (-0.06)

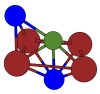

Li_4Mg_2Al (-0.05)

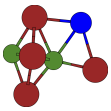

Li_4MgAl_2 (-0.05)

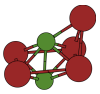

Li_5Al_2 (-0.04)

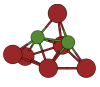

Li_6Al_2 (-0.04)

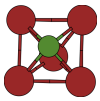

Li_5Al (-0.04)

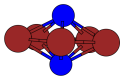

Li_5Mg_2 (-0.03)

$LiMg_4Al_2$ (-0.02)

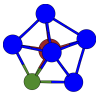

$LiMg_5Al$ (-0.02)

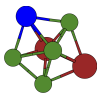

Li_2MgAl_4 (−0.01)

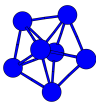

Mg_7 (0.00)

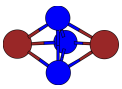

Li_2Mg_3 (0.01)

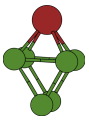

$LiAl_6$ (0.02)

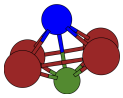

Li_4MgAl (0.03)

Li_2Al_5 (0.03)

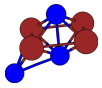

Li_4Mg_3 (0.03)

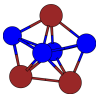

Li_3Mg_4 (0.04)

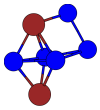

Li_2Mg_5 (0.04)

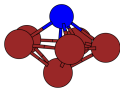

Li_6Mg (0.05)

Li_7Mg (0.07)

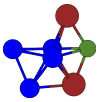

Li_2Mg_4Al (0.07)

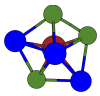

$LiMg_3Al_3$ (0.08)

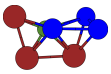

Li_3Mg_3Al (0.09)

Mg_6Al (0.11)

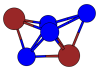

Li_2Mg_4 (0.12)

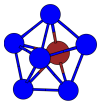

$LiMg_6$ (0.13)

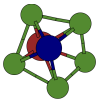

$LiMgAl_5$ (0.14)

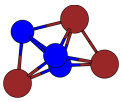

Li_3Mg_3 (0.15)

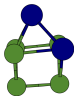

Mg_2Al_5 (0.15)

Li_3Mg_2Al (0.16)

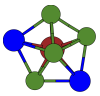

$LiMg_2Al_4$ (0.17)

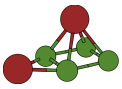

Li_2Al_4 (0.17)

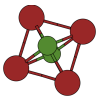

Li_4Al_2 (0.18)

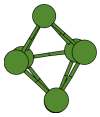

Al_7 (0.20)

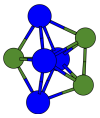

Mg_5Al_2 (0.21)

Li_3MgAl_2 (0.24)

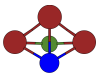

Li_3MgAl (0.26)

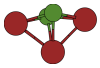

Li_3Al_2 (0.33)

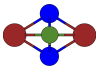

Li_2Mg_2Al (0.34)

Li_2Mg_3Al (0.35)

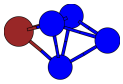

$LiMg_4$ (0.37)

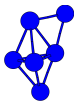

Mg_6 (0.37)

Mg_4Al_3 (0.38)

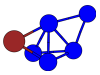

$LiMg_5$ (0.38)

Mg_5 (0.39)

Li_2MgAl_3 (0.40)

Mg_3Al_4 (0.42)

Li_8 (0.43)

$LiMg_2Al_3$ (0.45)

Li_3Al_3 (0.47)

$LiMg_3Al_2$ (0.51)

$LiMg_4Al$ (0.53)

$Li_2Mg_2Al_2$ (0.53)

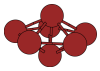

Li_7 (0.57)

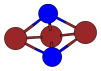

Li_3Mg_2 (0.59)

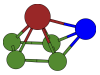

$LiMgAl_4$ (0.67)

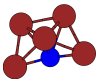

Li_5Mg (0.67)

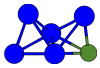

Mg_5Al (0.68)

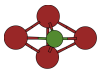

Li_4Al (0.72)

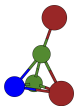

Li_2MgAl_2 (0.75)

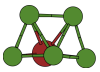

$LiAl_6$ (0.81)

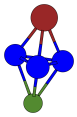

$LiMg_3Al$ (0.81)

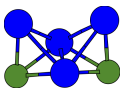

Mg_4Al_2 (0.84)

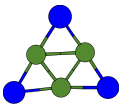

Mg_3Al_3 (0.88)

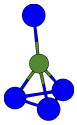

Mg_4Al (0.90)

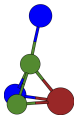

$LiMg_2Al_2$ (0.95)

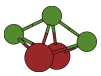

Li_2Al_3 (0.95)

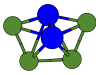

Mg_2Al_4 (1.00)

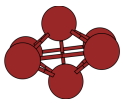

Li_6 (1.01)

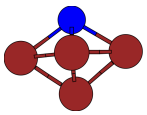

Li_4Mg (1.06)

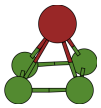

$LiAl_4$ (1.08)

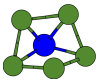

$MgAl_5$ (1.27)

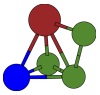

$LiMgAl_3$ (1.33)

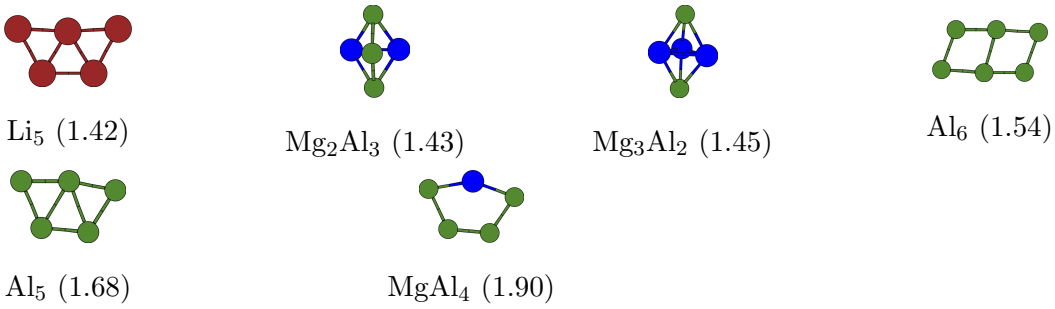

Fig. 6.1. Lowest energy structures of Li,Mg,Al clusters; R (eV) values in parentheses

6.3.2 Trends in Cluster Stability

We denote the negative of the atomization energy of the j^{th} cluster, $Li_xMg_yAl_z$, by $U\ (x, y, z)$ or U_j.

$$xLi + yMg + zAl \rightarrow Li_xMg_yAl_z \qquad : \ U_j$$

In order to show trends in the set of 130 atomization energies, we fitted the negative of atomization energies $U\ (x, y, z)$ by ordinary least squares (OLS) linear regression to a series of models of increasing complexity.

$$U_j \approx U_{j,fit} = \sum_i x_{ji}\beta_i \tag{6.3}$$

where x_{ji} is the i^{th} variable for the j^{th} cluster. The intercept was set to zero in every case. We used the following ten variables: the three stochiometric coefficients $x_1 = x$, $x_2 = y$, $x_3 = z$; the surface areas associated with each element, $x_4 = A_{Li}$, $x_5 = A_{Mg}$, $x_6 = A_{Al}$; and variables that depend on the electron count (x_7), the electronegativity of the atoms (x_8), the nonspherical shape of the cluster (x_9), and the parity (even

or odd) of the electron count (x_{10}). We quote all energies in eV. We now give explicit definitions for these variables.

The surface area variables $A_{Li} = x_4$, $A_{Mg} = x_5$, $A_{Al} = x_6$, were calculated as follows. We put overlapping spheres or radius r_k centered at nucleus k, where $r_k = sR_X$, R_X is the metallic radius of element X, and $s = 1.6$. We put 100,000 points on the surface of sphere k and calculate the number n_k of points that are closer to nucleus k than any other nucleus. The contribution of atom k to the surface area of element X is $4\pi r_k^2 n_k/100000$. The root-mean square error (RMSE) of fitted atomization energies using variables x_1 to x_6 inclusively depends only weakly on s when s is in the range 1.4 to 1.8, and it is a minimimum at $s \approx 1.6$, so we used $s = 1.6$ in all calculations reported here.

We define variable x_7 as

$$x_7 = \sqrt{\Delta N_e} \tag{6.4}$$

$$\Delta N_e = min\ (|N_e - 8|, |N_e - 20|) \tag{6.5}$$

where $N_e = x + 2y + 3z$ is the number of valence electrons in the cluster. The motivation for variable x_7 is the jellium model's prediction of electronic shell closings at $N_e = 8$ or and $N_e = 20$. Electron counts that deviate from 8 or 20 should be destabililizing. There is no theoretical justification for using $\sqrt{\Delta N_e}$ instead of ΔN_e, it simply gives a better fit.

Variable x_8 is defined as the standard deviation of the atoms' Mulliken electronegativities (3.00, 3.82 and 3.21 eV for Li, Mg and Al, respectively) from the mean in a given cluster. We expect x_8 to correlate with the size of ionic contributions to cluster

binding energies.

We calculated moments of inertia $I_c \leq I_b \leq I_a$ with fictitious unit mass assigned to every atom, so these moments of inertia are purely geometric constructs. Variable x_9 is given by

$$x_9 \;\; = \;\; |(2I_b - I_a - I_c)/I_a| \tag{6.6}$$

It deviates from zero when a cluster's shape deviates from quasi-spherical and has either a prolate shape $(I_c < I_b, I_b \sim I_a)$ or oblate shape $(I_c \sim I_b, I_b < I_a)$. These distortions from quasi-spherical shape are associated with higher surface areas and one may think they would increase the energy of a cluster. However, in the jellium model, these distortions are expected when the electron count deviates from 8 or 20, so this destabilizing effect is already partly accounted for with x_7. What we try to capture with x_9 is the *stabilizing* effect of Jahn-Teller distortions for a given open-shell electronic shell. In any case, x_9 and x_7 are correlated, and adding x_9 brings only a modest decrease in the RMSE of the fit. Finally, x_{10} is simply defined as 0 when N_e is even and 1 when it is odd. It relates to the stabilizing effect of spin subshell closing. We view (x_1, x_2, x_3) as one group of variables, (x_4, x_5, x_6) as a second group, and view the remaining variables individually.

The first insight we get by fitting atomization energies is in the hierarchy of variables required to achieve the best fits. With models of increasing complexity, the lowest RMSE are obtained by adding variables in precisely this order: (x_1, x_2, x_3), (x_4, x_5, x_6), x_7, x_8, x_9, and finally x_{10}. The results are shown in Table 6.1. The elements' cohesive energies (variables x_1, x_2, x_3) are by far the most important for

explaining cluster atomization energies, and surface areas (x_4, x_5, x_6) are clearly next in importance. The next two variables have nearly equal importance for explaining the data: electron count (x_7) and ionic bonding (x_8). The last two variables, cluster shape x_9 and spin-subshell closing x_{10}, add very little to the accuracy and could be ignored.

The parameters of the final 10-variable fit are instructive: $\beta_1 = -1.524$, $\beta_2 = -1.381$, $\beta_3 = -3.115$, $\beta_4 = +0.0174$, $\beta_5 = +0.0225$, $\beta_6 = +0.0393$, $\beta_7 = -0.162$, $\beta_8 = +0.240$, $\beta_9 = -0.347$, $\beta_{10} = +0.070$. The first three are the negative of effective cohesive energies for the three elements, in eV. All three are close to -0.92 times the experimental bulk cohesive energies which are 1.63 (Li), 1.51 (Mg) and 3.39 (Al). The next three fit parameters (in eV/Å^2) relate to surface energies and are positive, as they should. Converting to J/m^2 we get $\beta_4 = 0.279$, $\beta_5 = 0.360$, and $\beta_6 = 0.630$. These numbers correlate with experimental surface energies, the respective ratios are: $0.279/0.523 = 0.53$ for Li, $0.360/0.773 = 0.47$ for Mg, and $0.630/1.151 = 0.55$ for Al. They differ from 1 mostly because of how we calculate surface areas (with a $s = 1.6$, beginning of this section). The fact that the three ratios are close to each other is comforting.

As expected, we get a positive β_7 (destabilization of open electronic shells), a negative β_8 (stabilization from ionic contribution to bonding), a negative β_9 (stabilization associated with Jahn-Teller distortion) and a positive β_{10} (slight destabilization of doublet species relative to singlet).

Table 6.1: Mean absolute error (MAE), root-mean square error (RMSE), and fraction of variance unexplained by the fit (FVU=(RMSE/SD)^2), for atomization energies fitted with zero-intercept linear regressions using the first k variables. The mean and standard deviation (SD) of the atomization energies are 7.646 eV and 3.107 eV, respectively.

k	MAE	RMSE	FVU
3	0.480	0.644	0.0430
6	0.178	0.242	0.0061
7	0.171	0.223	0.0051
8	0.150	0.195	0.0039
9	0.151	0.190	0.0037
10	0.152	0.187	0.0036

The three-variable fit is the least accurate. But the difference between that fit and the DFT data is our working definition of cluster stability (RITS) and it gives useful insight as explained in section 6.2.1, so we will look at it in some detail.

The ten clusters with most negative RITS are shown in Table 6.3. They all have 8 atoms, $N_a = 8$. In fact, the 28 most stable clusters by RITS all have $N_a = 8$ (there are 45 8-atom clusters in total). This is understood simply by the surface area-to-volume ratio: it decreases, and the surface energy decreases, as N_a increases. The three most stable clusters have $N_e = 20$. The only other cluster with $N_e = 20$, $MgAl_6$, is ranked 29^{th} by RITS and it is the most stable cluster with $N_a < 8$. So, after N_a and surface energy, the most important factor in explaining the trend in cluster stability. appears to be the electron count N_e. However, ionic contributions to cluster binding are nearly as important. The least stable of the 8-atom clusters is Li_8 even though it has a closed electronic shell ($N_e = 8$) in the jellium model. Li_8, Mg_8, and Al_8, lack any stabilizing ionic contributions to the energy and rank 32nd, 40th and 45th out of the 45 8-atom clusters. The other elemental clusters, Li_n, Mg_n, and Al_n, are also near the bottom of their respective size group. They rank 36, 17 and 32 out of 36 ($n = 7$), 26, 11 and 28 out of 28 ($n = 6$), and 17, 6 and 20 out of 21 ($n = 5$).

Another way to quantify the importance for stability of different variables is to calculate the mean, over the 130 clusters, of the various terms in the 10-variable fit. They are, in eV: -13.663 for the cohesive energy term (x_1, x_2, x_3); $+5.918$ for surface energy (x_4, x_5, x_6); $+0.393$ for the electron count (x_7); -0.249 for the ionic term (x_8); -0.084 for shape distortion (x_9); and $+0.032$ for odd electron counts (x_{10}).

As the number of atoms n in clusters increase, the different terms should scale like this: n^1 (cohesive energy), $n^{2/3}$ (surface energy), n^0 (electron count), approximately n^1 (ionic term), approximately n^0 (shape distortion), and n^0 (odd electron count). The orbital effects associated with electron count and Jahn-Teller distortion must get relatively smaller as n increases. The relative stability, and the geometry, of large clusters are expected to depend mainly on surface area, the stoichiometry and degree of mixing (both of which affect ionic bonding), and factors tied to the local geometry around interior atoms (the cohesive energy term) such as coordination number and strain.

6.3.3 Geometric descriptors.

As an attempt to show trends in geometries, we use two descriptors of cluster shape, the asphericity ζ and shape η. The jellium model [23] predicts that clusters with an outer shell that is more than half filled have oblate geometries ($\eta < 0$) and those with an outer shell that is less than half filled are prolate ($\eta > 0$). Figure 6.2 (b) shows the mean asphericity of clusters with a given number of electrons, N_e, plotted as a function of N_e.

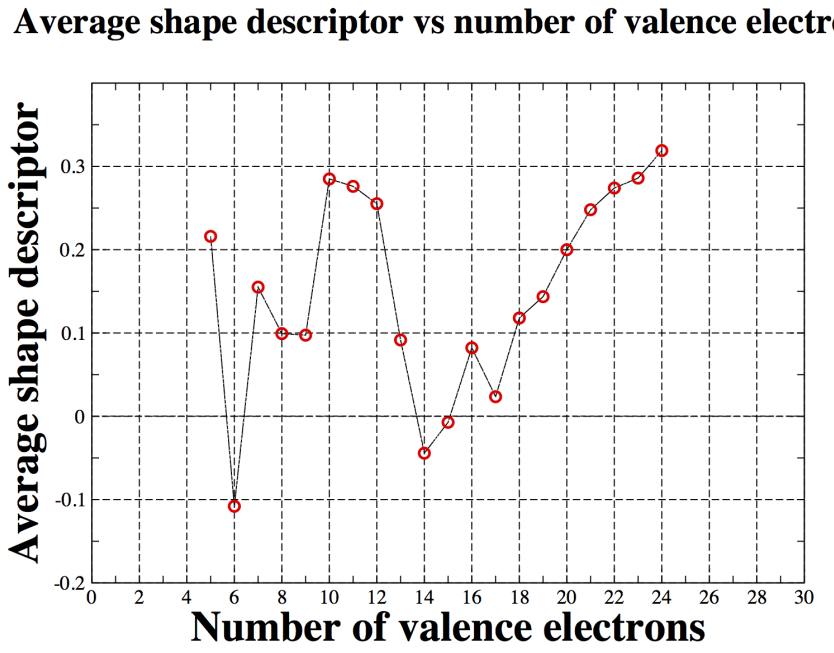

(a)

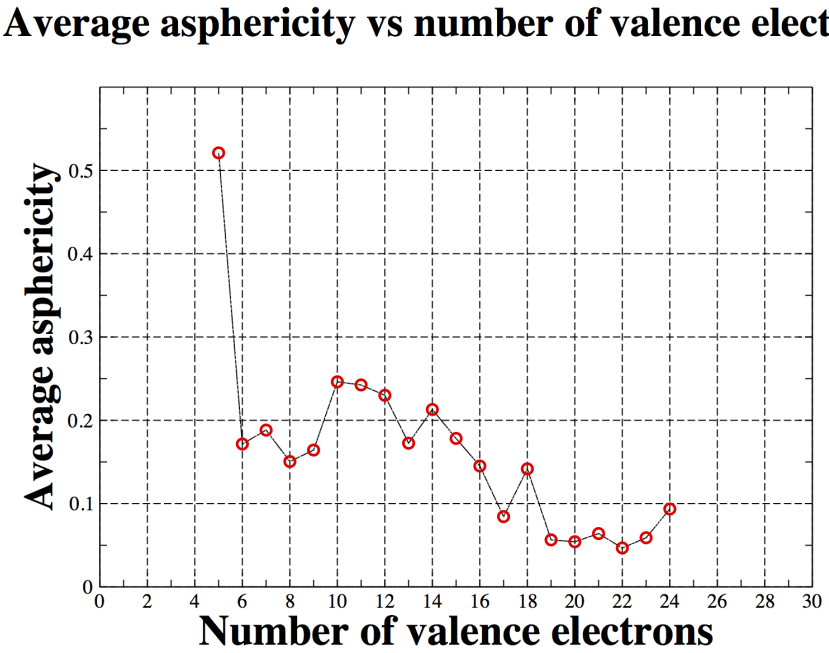

(b)

Fig. 6.2. (a) Average shape descriptor, and (b) average asphericity, as functions of number of electrons

The jellium model predicts that clusters with 8, 19, and 20 electrons are spherical. In agreement with this, we find a mean asphericity that is zero or very low for 8, 19 and 20 electrons. The mean asphericity is also small for numbers of electrons close to 8, 19 and 20. The mean value of the shape descriptor (Fig 6.2(a)) is in general agreement with the jellium model: close to zero for $N_e = 8, 18, 19, 20$, relatively small for $N_e = 6, 7$, relatively large for N_e =9–12, relatively small for N_e =13–17, and relatively large for N_e =21–24. The $N_e = 5$ case is an exception. At such a small cluster size the geometric constraints on possible arrangements of N nuclei in space makes the jellium model much less relevant. Ignoring the $N_e = 5$ case, it appears that the DFT global minimum geometries are in *rough* agreement with the jellium model, but the jellium model is of little use for predicting DFT global minima.

For every cluster we calculated the geometric center and the distance of every atom from it. The mean of all these atom-to-center distances is 2.48 Å for Li atoms, 2.40 Å for Mg atoms, and 2.01 Å for Al atoms, in line with the order in the surface energies of these elements. These atom-to-center distances in global minima structures show that it is energetically favorable to have Al atoms nearer to the center and Li and Mg on the periphery of clusters. We quantified the importance of this effect in another way. For every GM structure, we calculate the mean distance of element X to the geometric center, call that $R\,(X) = R_{GM}\,(X)$. Then, we generate a large number (a million or more) of homotops by a series of random interchanges of atomic positions Li↔Mg, Li↔Al, or Mg↔Al and recalculate, each time, $R(X)$. We define $f(X)$ as the fraction of these randomly generated homotops which have $R(X) < R_{GM}(X)$. A value of $f(X) \approx 0.5$ indicates no preferential position for element X, $f(X) \approx 1.0$ indicates

a strong preference for the periphery, $f(X) \approx 0.0$ indicates a strong preference for center of the cluster. After averaging over all 130 clusters we get $f(\mathrm{Li}) = 0.70$, $f(\mathrm{Mg}) = 0.57$, and $f(\mathrm{Al}) = 0.21$. Center-to-surface segregation is clearly one of the factors influencing GM structures.

In order to quantify the mixing tendency of the elements, we calculated a weighted mean distance for every pair AB of elements.

$$R(AB) \;=\; \frac{\sum_i \sum_j w_{ij} d_{ij}}{\sum_i \sum_j w_{ij}}$$

where d_{ij} is the distance between an atom i of element A and an atom j of element B. We took weights $w_{ij} = d_{ij}^{-6}$ in order to emphasize shorter distances. As before, we calclulated $R_{GM}(AB)$ for the global minimum structure, and then for a large number of randomly generated homotops, and calculated the fraction $M(AB)$ of those homotops that have $R(AB) > R_{GM}(AB)$, ie, homotops that show less mixing. Therefore $M(AB) = 1$ shows that the GM is maximally mixed, $M(AB) \approx 0$ shows that A and B segregate, and $M(AB) \approx 0.5$ shows no preference for either mixing or segregation. After averaging over all clusters that contain at least one atom of each element, we get $M(\mathrm{LiMg}) = 0.33$, $M(\mathrm{LiAl}) = 0.69$ and $M(\mathrm{MgAl}) = 0.53$. The average of these three values is 0.52 which is unremarkable. The apparent tendency of Li and Al to mix could be due to favorable ionic contributions to bonding or simply to the Li preference for peripheral sites on the clusters which produces few or no Li-Li neighbor pairs.

We calculated all X–A–Y angles where A=Li, Mg or Al, and (A,X) and (A,Y) are neighbors, for the 130 clusters. The results are summarized in Table 6.2. The angle

distribution around Li and Mg atoms are similar; but it is very different for Al with fewer 60° angles. The s-valence only elements Li and Mg have no directional bonding and tend to favor polytetrahedral geometries, rich in 60° angles, that minimize surface area. The p orbital of Al can give rise to directional bonding and more open angles consistent with maximum overlap of p orbitals in Al–Al pairs. Note in particular the presence of Al-containing 6-atom triangular prisms in the GM of Fig .6.1.

Table 6.2: Distribution of X–A–Y angles (X and Y are neighbors) for A=Li, Mg, Al, in the 130 global minima structures. The percentage of angles within ±7.5° of a given angle are shown, except for the last column which shows the percentage of angles bigger than 142.5°.

	60	75	90	105	120	135	>142.5
Li	71	6	7	11	3	1	1
Mg	65	5	7	14	6	1	2
Al	43	17	11	9	12	4	3

6.3.4 HOMO-LUMO gaps

The highest occupied molecular orbital (HOMO) to lowest unoccupied molecular orbital (LUMO) gap, E_g, is an important quantity [191]. The maximum hardness principle and empirical evidence suggest that E_g often correlates with kinetic stability [6]. A rationale for this is that E_g correlates with hardness $\chi = \frac{1}{2}(IE - EA)$, where IE and EA are the ionization energy and electron affinity of the molecule, respectively. Molecules or clusters with a large hardness do not easily give or accept electrons. Therefore, a reactant with a large E_g should disfavor reactions that involve accepting or donating electrons. It is natural to consider E_g in a search for stable clusters. The calculated E_g values for the $Li_xMg_yAl_z$ clusters are shown in Table 6.3, and E_g is plotted against the number of valence electrons N_e in Fig. 6.3.

The gaps of the species with the lowest RITS (R) are 1.36 eV (Mg_4Al_4), 1.59 eV ($LiMg_2Al_5$), 1.68 eV (Li_2Al_6), 0.34 eV (Li_2MgAl_5), and 0.82 eV (Mg_8). The largest gap in the set, 1.76 eV, is found for $MgAl_6$. It is consistent with the jellium shell closing at 20 electrons. In their study of Mg-Al alloy clusters Xing *et.al* [227] also found that $MgAl_6$ had the largest gap. They calculated E_g =2.60 eV for $MgAl_6$ with the hybrid exchange-correlation functional B3PW91, significantly larger than what we get with the PBE functional, 1.76 eV. This is typical: inclusion of Hartree-Fock exchange in hybrid functionals normally produces larger gaps. For comparison, some of the biggest gaps calculated for metal clusters include 2.46 eV for Mg_4Ag_{12} with the hybrid B3LYP functional [228] and 2.10 eV for Au_{20} calculated with BPW91 [229].

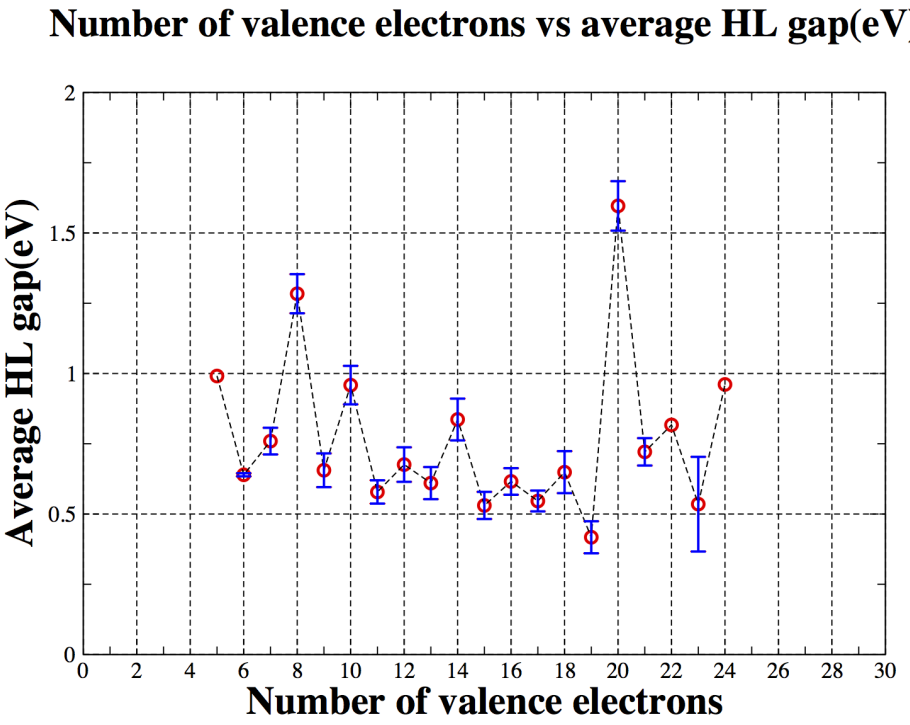

Fig. 6.3. E_g vs the number of valence electrons.

Table 6.3: RITS R, HOMO-LUMO gap E_g (eV) and cohesive energy E_c (eV/atom) for the ten most stable species.

Cluster	**R**	**HOMO-LUMO gap**	**AE**	E_c
Li_2Al_6	-1.649	1.678	15.35	1.92
$LiMg_2Al_5$	-1.464	1.589	13.17	1.65
Mg_4Al_4	-1.230	1.355	10.94	1.36
Li_2MgAl_5	-1.079	0.343	13.29	1.66
$LiMgAl_6$	-1.037	0.767	14.23	1.78
Li_3Al_5	-0.894	0.696	13.61	1.70
$LiMg_3Al_4$	-0.892	0.522	11.11	1.39
Li_5Al_3	-0.867	1.209	11.63	1.45
Li_4MgAl_3	-0.819	0.470	11.07	1.38
Mg_3Al_5	-0.815	0.624	12.01	1.50

Table 6.4: Mixing energies (eV) of the ten most stable, and ten least stable, binary or ternary clusters.

Cluster	RITS	E_{mix}
Li_2Al_6	−1.649	−1.694
$LiMg_2Al_5$	−1.464	−1.382
Mg_4Al_4	−1.230	−1.023
Li_2MgAl_5	−1.079	−1.093
$LiMgAl_6$	−1.037	−0.987
Li_3Al_5	−0.894	−1.003
$LiMg_3Al_4$	−0.892	−0.779
Li_5Al_3	−0.867	−1.103
Li_4MgAl_3	−0.819	−0.960
Mg_3Al_5	−0.815	−0.639
$LiMg_2Al_2$	0.950	−0.164
Li_2Al_3	0.955	−0.622
Mg_2Al_4	1.005	−0.145
Li_4Mg	1.064	−0.148
$LiAl_4$	1.078	−0.551
$MgAl_5$	1.267	−0.079
$LiMgAl_3$	1.335	−0.037
Mg_2Al_3	1.433	0.266
Mg_3Al_2	1.455	0.545
$MgAl_4$	1.902	0.477

We define the mixing energy of a n-atom cluster $Li_xMg_yAl_z$ ($n = x + y + z$) as

$$E_{mix} = \left(x\mathrm{AE}(\mathrm{Li}_n) + y\mathrm{AE}(\mathrm{Mg}_n) + z\mathrm{AE}(\mathrm{Al}_n) - n\mathrm{AE}(\mathrm{Li}_x\mathrm{Mg}_y\mathrm{Al}_z)\right)/n \qquad (6.7)$$

Table 6.4 gives the mixing energies for the 10 most stable, and the 10 least stable, mixed (binary or ternary) clusters. Mixing energies in Table 6.4 are all negative except for three. Table 6.4 seems to show a good correlation between R and E_{mix} for the most stable clusters, but not for the least stable ones. Among the 118 binary and ternary clusters, 13 have a positive mixing energy and 105 a negative one. The mean of E_{mix} over the set of 118 is $-0.427\,\mathrm{eV}$ and the standard deviation is $0.390\,\mathrm{eV}$. For the entire set of 130 clusters, the mean and standard deviation of E_{mix} are -0.388 and $0.391\,\mathrm{eV}$, respectively.

Dividing clusters in five categories, we find these mean values of mixing energies: $-0.312\,\mathrm{eV}$ for the 22 $\mathrm{Li}_x\mathrm{Mg}_y$ clusters; $-0.772\,\mathrm{eV}$ for $\mathrm{Li}_x\mathrm{Al}_z$; $-0.044\,\mathrm{eV}$ for $\mathrm{Mg}_y\mathrm{Al}_y$; $-0.492\,\mathrm{eV}$ for the 52 ternary clusters; and zero of course for elemental clusters.

Recall that the analysis of energy trends by sequential linear regressions in section 6.3.2 gives a mean ionic contribution $E_{ionic} = -0.249\,\mathrm{eV}$ per cluster. We believe that the difference, $E_{mix} - E_{ionic} = -0.388 - (-0.249) = -0.139\,\mathrm{eV}$, shows the mean stabilizing effect of having atoms of the lowest surface energy element (Li) on the outside of the clusters. This can explain the large negative E_{mix} values for $\mathrm{Li}_x\mathrm{Al}_z$ clusters. In these clusters, Li atoms act a bit like a partial passivating layer for the high surface energy Al_z core. Note that the analysis of section 6.3.2 shows a mean surface energy contribution of $+5.918\,\mathrm{eV}$. The stabilization coming from the preferential position of Li atoms on the periphery is a small fraction of that, $0.139/5.918 = 0.023$.

6.4 Conclusion

Small alloy clusters of Li, Mg and Al are of limited interest in themselves because they cannot be isolated and could hardly be used as catalysts or in materials. They are useful, however, for testing theories such as the ellipsoidal jellium model [23, 76] (EJM) and for showing the interplay of different effects on the structure and energy of metal alloy clusters.

A superficial look at our results shows that the EJM has some validity. For instance, the three clusters with lowest RITS all have 20 valence electrons; the HOMO-LUMO gaps are larger, on average, at electron counts 8 and 20; the average shape descriptor plotted against the number of electrons is in line with EJM predictions. However, a closer look shows many discrepancies between our results and EJM predictions. Likewise, a quick look at the GM in Fig. 6.1 reveals patterns: Li atoms are usually on the periphery and Al atoms usually near the center; 6-atom triangular prism motifs usually contain many Al atoms. Similar observations about energies and structures of clusters were made before. These types of results become more significant if we can quantify them, even if only approximately. We believe the main findings of this study are in quantifying these observations about trends. We will briefly recapitulate this aspect.

By doing simple linear regressions and adding one term at a time we assessed, roughly, the importance of energy contributions to the AEs of the clusters studied here. The fraction of variance that is unexplained (FVU) by a linear regression of AEs is 4.30% with a model that simply assigns a cohesive energy contribution to

every atom. The FVU goes from 4.30% to 0.61% upon adding a surface energy term. It goes to 0.51% upon adding a term that describes electronic shells. And the FVU goes to 0.39% upon adding a term that models ionic bonding. Terms that model Jahn-Teller distortion and spin subshell closing do not change the FVU appreciably.

The energy contributions in the final linear regression (FVU=0.0036) give a sense for the magnitude of various effects. In our regression of 130 AEs, the cohesive and surface energy contributions are very large: on average they are $-13.66\,\mathrm{eV}$ and $+5.92\,\mathrm{eV}$, respectively. The energy penalty associated with an electron count that deviates from 8 or 20 varies between 0.00 and $+0.59\,\mathrm{eV}$ and it is $+0.39\,\mathrm{eV}$ on average. The effect of electron count on the HOMO-LUMO gaps can be as large as $0.7\,\mathrm{eV}$ (Fig. 6.3). The ionic term in our model varies between 0.00 and $-0.68\,\mathrm{eV}$ (for Li_4Al_4), and it is $-0.25\,\mathrm{eV}$ on average. The term that models distortions from a quasispherical shape varies between 0.00 and $-0.23\,\mathrm{eV}$ (for Mg_4Al) and it is $-0.08\,\mathrm{eV}$ on average. Finally, the energy penalty for an unpaired electron is $+0.07\,\mathrm{eV}$ in our model. This kind of analysis, and the magnitude of the various energy terms, may give some guidance for making approximate energy models for metal alloy nanoparticles.

Chapter 7

Theoretical study of $(Al_2O_3)_n$ $(n = 1 - 3)$ and Al_xO_y, $(x + y < 17)$ clusters

7.1 Introduction

Alumina, Al_2O_3, is a common material that has many technological applications [230, 231, 232] especially as nanostructured ceramic materials, solid catalysts, and as supports for catalysts [233, 234, 235]. Small alumina crystals play an important role in astrophysics [236] and atmospheric chemistry [237]. There have been many studies of aluminium oxide clusters, in particular, computational studies of the stoichiometric clusters $(Al_2O_3)_n$ [238, 239, 240, 241, 294, 328]. Very small clusters may adopt stoichiometric ratios, or structures, that differ from the bulk. These small clusters can give insight into the growth mechanisms of oxides, starting with only a few atoms, and into possible local structures near impurities or surface defects.

In the present work we are concerned mainly with the stoichiometry and geometric

structure of the most stable species among very small Al_xO_y clusters, $x + y < 17$, as revealed by Density Functional Theory (DFT) calculations, and trends in computed energies and structures. Clusters of aluminum oxide have been studied by theory [85, 239, 241, 244, 245, 246, 247, 248, 249, 250, 251] and experiments [252, 253, 254, 255, 256, 257, 258]. Both stoichiometric and non-stoichiometric species have been studied extensively. For example, Sun *et al.* [85] studied the structural evolutions of $(Al_2O_3)_n$ molecules with $n = 1 - 10$ and $n = 30$. They found cage structures for the global minima for $n = 1 - 5$, and cage-dimer structures at $n = 6 - 9$. Woodley [244] optimized the structures of $(Al_2O_3)_n$ $(n = 1 - 5)$ by DFT starting with initial structures found with an evolutionary algorithm and empirical interatomic potential. Rahane *et al.* [241] derived the structures of $(Al_2O_3)_n$ $(n = 1 - 10)$ using DFT and simulated annealing. Li and Cheng [239] obtained the structures of $(Al_2O_3)_n$, $(n = 1 - 7)$ clusters with a genetic algorithm. Non-stoichiometric Al_xO_y have also been studied. Al_3O_2 and Al_2O_3 have been the subject of several experiments and computations [254, 255, 258, 259, 260, 261, 262]. Archibong *et al.* [263] studied the geometric and electronic structure of AlO_4 and AlO_4^- for the lowest energy states. Zhong *et al.* [246] studied the geometric structures, relative stabilities, and electronic properties of a series of neutral and anionic tetra-aluminum oxide clusters $Al_4O_n^\lambda$, $(3 \leq n \leq 8, \lambda = 0, -1)$ by DFT. They found $Al_4O_{4,6}^\lambda$ clusters to be more stable than their neighbours. Gowtham [264] *et al.* calculated the electronic and structural properties of neutral and anionic Al_3O_n, $(n = 6 - 8)$ by DFT and did experiments on $Al_3O_6H_2^-$. They found that oxidation of Al_3O_5 causes significant structural changes in these molecules.

Here we present the results of Kohn-Sham DFT calculations of 14 Al_xO_y ($x + y < 17$) cluster species. We report ground-state geometries, HOMO-LUMO gaps, atomization energies (AE), and we assess the relative stability of the clusters by taking the difference between AEs calculated by DFT and those from a simple model fitted to them. By this criterion we find, among other things, that Al_6O_8 is more stable than Al_6O_9.

The rest of this chapter is organized as follows. Section 7.2 describes our computational methods. The results are given and discussed in section 7.3. The main findings are summarized in section 7.4.

7.2 Theoretical methods and computational details

Electronic structure calculations and geometry optimizations were carried out with Kohn-Sham DFT as implemented in the Gaussian09 [49] software. We used the non empirical generalized gradient approximation for exchange-correlation with the functional of Perdew, Burke and Ernzerhof [59] (PBE). The LANL2DZ effective core potential (ECP) and basis set [225, 226] was employed. Global optimization was done with a modified version of the Tabu Search in Descriptor Space (TSDS) method [48] and local optimization was done using Gaussian. We calculated vibrational frequencies to verify that the geometries we found are minima. Singlet and triplet states were considered in all cases except odd-electron species (Al_3O_7, Al_5O_5, Al_7O_9) where we considered a doublet.

To make meaningful energy comparison between different chemical species, we

used a Relative Index of Thermodynamic Stability (RITS) [111].

7.3 Results

7.3.1 Stoichiometric oxides, $(Al_2O_3)_n$

The lowest energy isomers we found for $(Al_2O_3)_n$ (n =1-3) are shown in Fig. 7.1. We compared our results with those of earlier studies. Where there was disagreement, we took the lowest energy structure from the literature and performed a local optimization.

$(Al_2O_3)_n$	(a)	(b)
$n = 1$	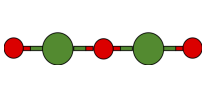	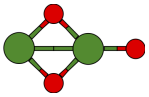
	$\Delta E\ (eV) = 0.0$	$0.3\ (eV)$
$n = 2$	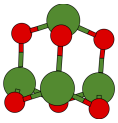	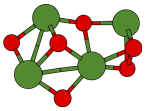
	$\Delta E\ (eV) = 0.0$	$0.18\ (eV)$
$n = 3$	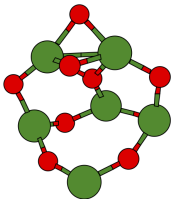	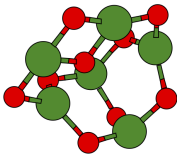
	$\Delta E\ (eV) = 0.0$	$0.4\ (eV)$

Fig. 7.1. Lowest energy isomers of $(Al_2O_3)_n$

($\mathbf{Al_2O_3}$): The lowest-energy geometry of Al_2O_3 is linear. It forms a singlet state. Its isomer, a rhombus with an oxygen atom attached to one of the Al atoms is 0.3 eV higher in energy and forms a triplet state. This result agrees with the studies by Fernandez [247], Sun and coworkers [85], Nemukhin [326] and Solornonik [327] who found a linear structure as the global minimum (GM). However, this result disagrees with calculations by Li [239], Rahane [241], Sharipov [328], Woodley [244] and their coworkers. They predicted the rhombus structure to be the GM for Al_2O_3. The Al-O bond lengths are 1.67 Å and 1.71 Å.

($\mathbf{Al_2O_3})_\mathbf{2}$. The GM is a T_d symmetry cage with four Al atoms forming a tetrahedron and the six O atoms capping the edges of the tetrahedron. The Al-O bond lengths are 1.79 Å. The ground state is a singlet. This agrees with earlier studies [247, 239, 241, 85, 328]. We found an isomer 0.18 eV above the GM consisting of four Al atoms in a plane with O atoms sides linking the Al atoms. It was predicted to be lowest energy isomer by Woodley [244].

($\mathbf{Al_2O_3})_\mathbf{3}$: We find two isomers within 0.4 eV. The GM is a triplet with C_1 symmetry. This is in agreement with Woodley [244, 239]. We find a C_{2v} symmetry isomer consistent with the results by Sharipov *et al.* [328]. Our calculated Al-O bond lengths range from 1.74 Å to 2.10 Å.

7.3.2 Other (non-stoichiometric) ($\mathbf{Al}_x\mathbf{O}_y$) clusters.

The lowest-energy isomers of non-stoichiometric clusters are shown in Fig. 7.2.

($\mathbf{Al_2O_y}$), ($\mathbf{y = 2, 4}$). The lowest energy isomer for Al_2O_2 is a linear ($C_{\infty v}$) structure. It is a singlet state. We also found a square cyclic structure (D_{2h}) which

is 0.19 eV higher in energy than the linear configuration. In separate optimization studies by Nemukin *et al.* [261] and Sarker *et al.* [272], a linear structure of Al_2O_2 was predicted to be one of low-energy isomers. The Al-O bond lengths are 1.67 Å, 1.72 Å and 1.76 Å.

Semiempirical and *ab initio* calculations on Al_2O_2 suggested that there are two stable isomers, a square and a linear configuration that is 0.65 eV less stable [270]. Linear Al_2O_2 was found to be more stable than the square cyclic structure in matrix isolation studies [260, 259, 268] and calculations with high levels of theory (multi-reference configuration interactions and completely renormalized CCSD (T)) [272, 273]. Calculations by DFT, MP (2) and CCSD (T) predict a D_{2h} structure as the ground state followed by the linear configuration [262]. Later studies have shown that singlet D_{2h} (rhombus) structure is the global minimum [271].

The GM of Al_2O_4 that we found is a triplet state rhombus with one oxygen atom attached to each of the Al atoms. It has D_{2h} symmetry. It is in agreement with the predicted GM of Desai *et al.* and Patzer *et al.* [254, 265].

($\mathbf{Al_4O_y}$), ($\mathbf{y = 5, 7}$): The GM for Al_4O_5 is a C_s symmetry hexagon with alternating Al-O atoms and a linear Al-O chain attached to one side. The Al-O bond lengths range from 1.67 Å to 1.77 Å. This structure was found to be a low-lying isomer by Zhong *et al.* [246]. Addition of one oxygen to Al_4O_6 leads to a distorted sheet-like configuration. The GM found for Al_4O_7 has C_1 symmetry. It can be viewed as a O_2 unit replacing the apex oxygen atom in the low- lying isomer 2 (b) of Al_4O_6. The GM we find for Al_4O_7 is in agreement with that predicted by Zhong *et al.* [246]. For Al_4O_5 we find that the singlet and triplet states are almost degenerate, with the

singlet being more stable by 0.02 eV. For Al_4O_7 the singlet is more stable than the triplet by 0.8 eV. The Al-O bond lengths vary from 1.79 Å to 1.98 Å.

($\mathbf{Al_6O_y}$), ($\mathbf{y = 8, 10}$). The GM we find for Al_6O_8 is formed by joining two hexagons with two capping oxygen atoms on either side. The Al-O bond lengths range from 1.74 Å to 2.00 Å. The most stable isomer for Al_6O_8 is a triplet state which is 0.7 eV lower in energy than the singlet state. All atoms of Al_6O_{10} are in the same plane except for two oxygen atoms, with one above and the other below the plane. The GM is the triplet state and it is 1.1 eV lower in energy than the singlet state. The Al-O bond lengths range from 1.72 Å to 2.01 Å.

The ground states of Al_xO_y clusters are singlet or doublet in all cases except Al_2O_4, Al_6O_8, Al_6O_9 and Al_6O_{10}. The ground states of Al_3O_7 and Al_5O_5 are doublets. Non planar structures start to emerge for clusters with 10 or more atoms. Clusters with a composition $x/y < 2/3$, are electron deficient and normally exhibit O-O bonds. The GM structure for these clusters (Al_3O_7, Al_4O_7, and Al_6O_{10}) can be viewed as resulting from the substitution of an oxygen atom by an O_2 molecule.

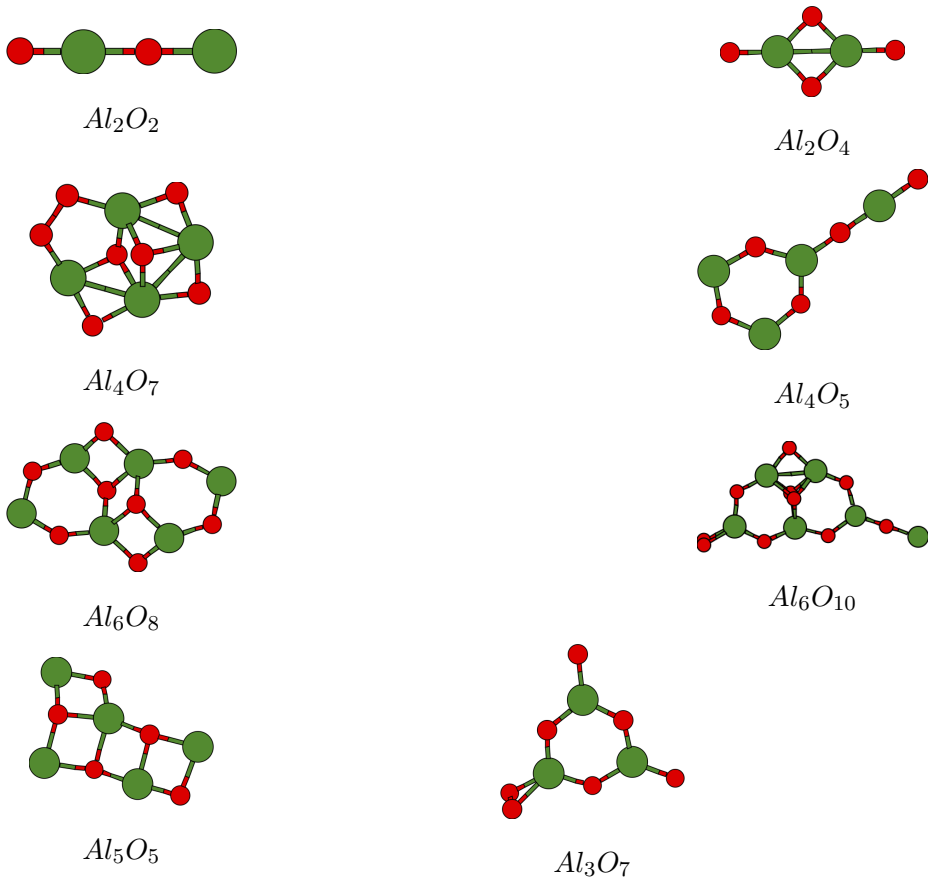

Fig. 7.2. Lowest energy isomers of Al_xO_y

Fig.7.3 shows the distribution of distances in the GM of the Al_xO_y clusters studied here. The first peak (Al-O bond lengths) tends to be narrower for smaller clusters, and for clusters that are energetically more stable (Al_2O_2, Al_4O_6 and Al_6O_8, see subsection 3.4).

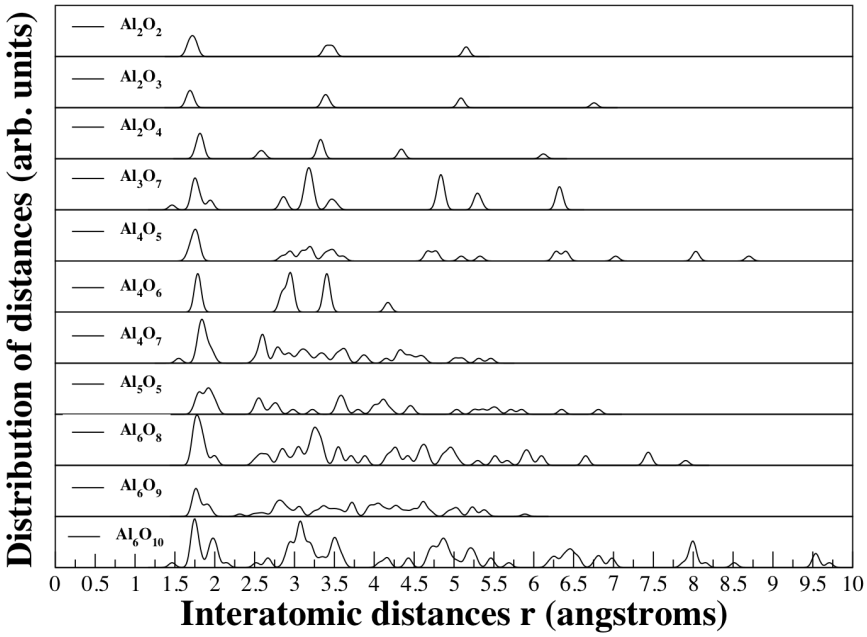

Fig. 7.3. Distance distribution in Al_xO_y clusters

7.3.3 Electronic properties

We calculated the energy gap E_g between the highest occupied molecular orbital (HOMO) and the lowest unoccupied molecular orbital (LUMO). In open-shell cases we calculated the gap for alpha spin and beta spin and took E_g as the smaller of the two. The HOMO-LUMO gaps are shown in Table 7.1 along with the vertical ionization potentials (VIP), vertical electron affinities (VEA), atomization energies (AE), and index of thermodynamic stability (R).

There is a rough correlation between E_g and the kinetic stability of molecules and clusters. The maximum hardness principle suggests that it also correlates with conformational ("mechanical") and thermodynamic stability [187, 188, 189]. The E_g

of Al_xO_y clusters are much smaller than the experimental band gap of bulk alumina (8.7 eV) [264]. This is expected for such small clusters. The effect of oxidation is more pronounced in the case of smaller clusters as compared to the bigger ones. Oxygen deficient alumina clusters have smaller values of VIP. Oxygen-rich alumina clusters have higher VEAs as expected on the basis of the atoms' electronegativities (O: 7.54 eV; Al: 3.21 eV). This trend was also reported by Wu et. al. [258].

Our calculated VEAs agree well with the experimental EAs, they are, in eV: for Al_2O_4, 4.63 vs 3.98 [254]; for Al_4O_5, 2.44 vs 2.59 [255]; and for Al_5O_5, 2.61 vs 2.22 [255].

7.3.4 Relative stability

The most obvious trend in stability (RITS values in Table 7.1) is that bigger clusters are generally more stable. This is expected: the surface-to-volume ratio decreases with size and it is the most important factor for cluster stability. However, there are many instances where the stability order does not follow the number of atoms $(x+y)$ — Al_2O_2 vs Al_2O_3, Al_4O_5 vs Al_5O_5, Al_6O_8 vs Al_6O_9, etc.

Energies of reaction (in eV) show that stoichiometric Al_xO_y clusters (those with $x/y = 2/3$) are not always more stable than the non-stoichiometric ones.

$$Al_2O_2 + Al_2O_4 \rightarrow 2Al_2O_3 \quad \Delta E = +0.33$$

$$Al_4O_5 + Al_4O_7 \rightarrow 2Al_4O_6 \quad \Delta E = -3.78$$

$$Al_5O_5 + Al_3O_7 \rightarrow 2Al_4O_6 \quad \Delta E = -6.58$$

$$Al_6O_8 + Al_6O_{10} \rightarrow 2Al_6O_9 \quad \Delta E = -0.90$$

From these, it appears that Al_4O_6 is particularly stable (relative to others), but that Al_2O_3 is not, and that Al_6O_9 is only slightly more stable than its non-stoichiometric partners. However, energies of reaction give an incomplete picture. For instance, the fourth reaction ($\Delta E = -0.90\,\text{eV}$) could be negative because Al_6O_9 is stable, or because Al_6O_8, or Al_6O_{10}, or both, are unstable. The RITS values (chapter 4, (4.13)) amount to a comparison of every cluster energy to all other cluster energies and provide a more complete picture of thermodynamic stability. The RITS values (R in Table 7.1) show that: (i) Al_2O_2 is stable (smaller R) relative to Al_2O_3 and Al_2O_4; (ii) Al_4O_6 is much more stable than Al_4O_5 and Al_4O_7; and (iii) Al_6O_8 is more stable than Al_6O_9 (and Al_6O_{10}). So, even with our very small data set, we find two examples of non-stoichiometric clusters, Al_2O_2 and Al_6O_8, that are more stable than their stoichiometric counterpart. This trend in RITS is fully consistent with the trend in E_g and the maximum hardness principle: (i) the HOMO-LUMO gap of Al_2O_2 is larger than those of Al_2O_3 and Al_2O_4; (ii) the HOMO-LUMO gap of Al_4O_6 is larger than those of the four species below it in Table 7.1; and (iii) the HOMO-LUMO gap of Al_6O_8 is larger than those of Al_6O_9 and Al_6O_{10}. In these ultra-small clusters, details of the geometric and electronic structure matter as much as the stoichiometric ratio. A look at Fig. 7.1 and Fig. 7.2 suggests that stability is achieved with geometric structures made entirely of 4- and 6-membered rings where Al and O atoms strictly alternate. In very small clusters, there may not be any such structure for certain compositions (e.g., Al_2O_3).

Cluster	R (eV)	α-HL gap (eV)	β-HL gap (eV)	IP (eV)	EA (eV)	AE (eV)
Al_6O_8	-3.56	2.92	2.49	7.94	2.67	64.08
Al_6O_9	-3.31	1.98	1.29	8.33	2.78	67.52
Al_6O_{10}	-2.16	3.16	0.00	8.55	3.09	70.06
Al_4O_6	-0.48	1.90		9.21	2.76	43.29
Al_4O_7	0.58	1.47		9.20	2.58	45.91
Al_4O_5	2.23	0.96		7.57	2.44	36.89
Al_3O_7	2.80	1.14	0.43	11.8	3.58	38.52
Al_5O_5	2.81	1.58	0.13	7.35	2.61	41.48
Al_2O_2	3.55	2.86		8.87	0.52	14.16
Al_2O_3	3.81	2.20	0.06	9.35	1.95	17.59
Al_2O_4	3.83	3.91	0.00	18.22	4.63	21.26

Table 7.1: RITS (R), HL gap, Vertical Ionization energies, Electron affinity and Atomization energy values for Aluminium oxide clusters

In Table 7.1, Al_6O_8 stands out. It has a big HOMO-LUMO gap and the smallest RITS. Curiously, it also has a small value of vertical ionization potential. On the basis of our stability analysis we expect Al_6O_8 will be abundant in experiments on ultra-small neutral alumina clusters. We give our calculated vibrational frequencies and IR intensities in Table 7.2 in hope they may help identify this cluster.

61 (1.1), 83 (0.7),122 (0.0), 136 (20.4), 143 (0.0), 162 (3.7),
173 (0.0), 197 (0.0), 212 (38.9), 248 (79.9), 251 (0.0), 258 (32.8),
283 (0.0), 304 (0.0), 318 (84.0), 320 (0.1), 369 (0.0), 383 (117.3),
446 (0.0), 456 (122.4), 487 (36.4), 508 (0.0), 551 (166.4), 551 (15.6),
587 (185.1), 597 (0.0), 683 (0.0), 697 (63.9), 704 (0.4), 707 (166.9),
739 (0.0), 746 (269.1), 889 (0.0), 910 (584.8), 944 (797.3), 954 (0.1)

Table 7.2: Harmonic frequencies (in cm^{-1}) and IR intensities (in km/mole) in parentheses for Al_6O_8

7.4 Conclusion

We calculated ground-state geometries and energies of Al_xO_y clusters ($x+y < 17$) by DFT with the PBE exchange-correlation functional. The stability of cluster species was assessed with energies of reaction, a relative index of thermodynamic stability (RITS), and the HOMO-LUMO gap. Out of three clusters with stoichiometry $(Al_2O_3)_n$ (n =1,2,3), only Al_4O_6 is stable relative to clusters of comparable size. By all measures, Al_2O_2 is more stable than Al_2O_3 and Al_6O_8 is more stable than Al_6O_9. For a given x, in Al_xO_y, the ionization potential and the electron affinity increase with y but do not correlate with cluster stability. The geometries of the most stable clusters of each size category (Al_2O_2, Al_4O_6, Al_6O_8) are characterized by the absence of Al-Al or O-O bonds and the absence of any structural motifs other than 4- and 6-membered rings. The stability (RITS and HOMO-LUMO gap) of Al_6O_8 is remarkable. It suggests that Al_6O_8, and maybe also Ga_6O_8 and In_6O_8, could be relatively abundant species in cluster experiments. We studied only a few very small

species, but our results show that non-stoichiometric clusters could play a role in the early stages of growth of group 13 oxides.

Chapter 8

Small silicon oxide clusters (Si_xO_y), $(x = 1 - 4, y = 2x \pm 1)$ and Si_3O_y $(y = 1 - 9)$

8.1 Introduction

Silicon oxide is an essential material in electronics, optical communication systems, thin-layer coatings, solar cells, and medical applications[277]. Silica glass is a vital component in optical fiber communication [277, 278]. It has been found experimentally that the growth of silicon nanowires is greatly enhanced by the presence of silicon dioxide during synthesis [279]. Recently, Si/SiO_x composite powders have attracted a great deal of interest in lithium-ion batteries [280]. This composite structure makes the batteries more efficient and also maintains their high capacity. Nanoparticles and clusters Si_xO_y are obviously important for nanoscience.

The structural and electronic properties of silicon oxide clusters have been studied both experimentally [281, 295, 283, 310, 285, 286, 287] and theoretically [288,

289, 290, 291, 292, 293, 294]. Wang and coworkers [295] studied small anionic clusters including $Si_3O_n^-$ $(n = 1-6)$, $Si_nO_n^-$ $(n = 3-5)$, $(SiO_2)_n^-$ $(n = 1-4)$ and Si $(SiO_2)_n^-$ $(n = 2, 3)$ using photoelectron spectroscopy. Large changes in the geometry have been revealed upon ionizing the neutral clusters. The Si_3O_4 cluster was proposed to model oxygen-deficient defects in bulk silicon oxide. Reactions of cationic silicon clusters containing up to six atoms with oxygen were studied by Creasy *et al.* [296]. Bergeron and Castleman Jr. [297] studied the stability of silicon cluster ions by O_2 etching. Their results suggested that Si_n^+ $(n = 4, 6, 9, 13, 14, 23)$ and Si_n^- $(n = 18, 21, 24, 25, 28)$ have large stability.

Harkless *et al.* [298] used molecular dynamics and an additive pair interaction potential to theoretically study the possible stable structures of $(SiO_2)_n$. Cheung et. al [299] evaluated the ground-state structures and electronic properties of Si_nO_m $(n, m = 1, 8)$ clusters using both semiempirical molecular orbital and DFT calculations. Chelikowsky and coworkers [300] investigated the geometric structures and electronic properties of neutral and charged Si_nO_n $(n = 3, 4, 5)$ clusters by using a higher-order finite-difference pseudopotential method. Nayak *et al.* [301] studied the atomic and electronic structure of neutral and charged Si_nO_m clusters $(n \leq 6,$ $m \leq 12)$ and Si_3O_n $(n = 1, 3, 4)$. They found that a double oxygen bridged motif is energetically favored for Si_2O_n $(n = 2-6)$ clusters. Chu *et al.* [288] performed a detailed computational study of the structures of Si_nO_m $(n, m = 1-8)$ clusters using DFT-B3LYP and suggested several new geometries for these clusters. Zang *et al.* [302] systematically studied the stability and oxidation pattern of Si_6O_n $(n = 1-12)$ using DFT. Lu and co-workers [303] performed a systematic study of the structures

and fragmentations of small silicon oxide clusters Si_mO_n ($m = 1-5, n = 1-(2m+1)$). Their study showed that SiO is the most abundant species in fragmentation and that $(SiO_2)_n$ clusters tend to have the largest dissociation energy. In other studies by Bromley *et al.* [304, 305] and Zhang *et al.* [306], ab initio calculations of larger silicon oxide clusters with O:Si ratios of 2:1 and 1:1 were reported. The studies on medium size clusters provide information on the most stable motif of silicon dioxide clusters. Wang *et al.* did an experimental study of Si_3O_n, $(n = 1-6)$ clusters [295]. Although an experimental study of Si_3O_n, $(n = 1-6)$ clusters has been conducted, the size was limited up to 6 oxygen atoms. Study of O-rich silicon oxide is important to study the trends in the stability of these clusters.

Here we present a DFT and global optimization study of (Si_xO_y), $(x = 1-4)$ and $(y = 2x, 2x \pm 1)$ clusters, Si_3O_y, $(y = 1-9)$, and Si_xO_7, $(x = 2-5)$ clusters. This chapter is organized as follows. In section 8.2, the computational methods are described. In section 8.3, low-energy structures are presented. The relative stability of the clusters is presented in section 8.4 followed by a discussion in section 8.5.

8.2 Computational Methods

We performed Density Functional Theory (DFT) calculations with the Perdew-Burke-Ernzerhof generalized gradient approximation to exchange-correlation [59]and the Gaussian software. Recently, Byun *et al.* [307] evaluated three functionals (B3LYP, PBE, and M06) and 29 different basis sets for studying the structural and electronic properties of silicon oxide clusters. The calculated values of the electron

affinities and vertical detachment energies of SiO_2 and Si_2O_4 clusters were compared with the experimental ones. They concluded that PBE/DGDZVP was the best for calculating the structural and electronic properties of small silicon oxide clusters, but it underestimated the electron affinities (EA). Using the LANL2DZ basis set and effective core potential gave EA values closer to the experimental values. In another study by Bae *al.* [308] of Cu_nO_n, $(n = 1 - 4)$, results from B3LYP and different basis sets were compared with the experimental values. It was found that LANL2DZ gave values closer to the experimental values. Therefore we used the PBE functional with the LANL2DZ [225, 226] basis set. Global optimization was carried out using a modified version of the Tabu Search in Descriptor Space (TSDS) method [48]. We calculated DFT energies with Gaussian 16 at every step of the TSDS global optimization. For instance, for Si_2O_4, Si_3O_6, Si_4O_8 and Si_5O_7, we performed 250, 600, 800 and 900 energy evaluations with TSDS. These were followed by 20, 30, 20 and 10 local optimizations for these clusters. To make meaningful energy comparisons between different chemical species, we used the Relative Index of thermodynamic stability (RITS) [111]. The atomization energies of all Si_xO_y clusters are fitted to a simple geometry-independent model:

$$AE_{fit}\ (C_j, X_j) = xU_{Si} + yU_O$$

The parameters of the fit, U_{Si} and U_O, are obtained by ordinary least-squares. The fit results in $U_{Si} = -5.022\,eV$ and $U_O = -3.674\,eV$, and are interpreted as the mean cohesive energies of Si and O for the given set of clusters.

8.3 Results

8.3.1 Lowest-energy structures

The putative global minima and low-lying isomers (within 0.5 eV) found by DFT-TSDS are shown in Fig. 8.1.

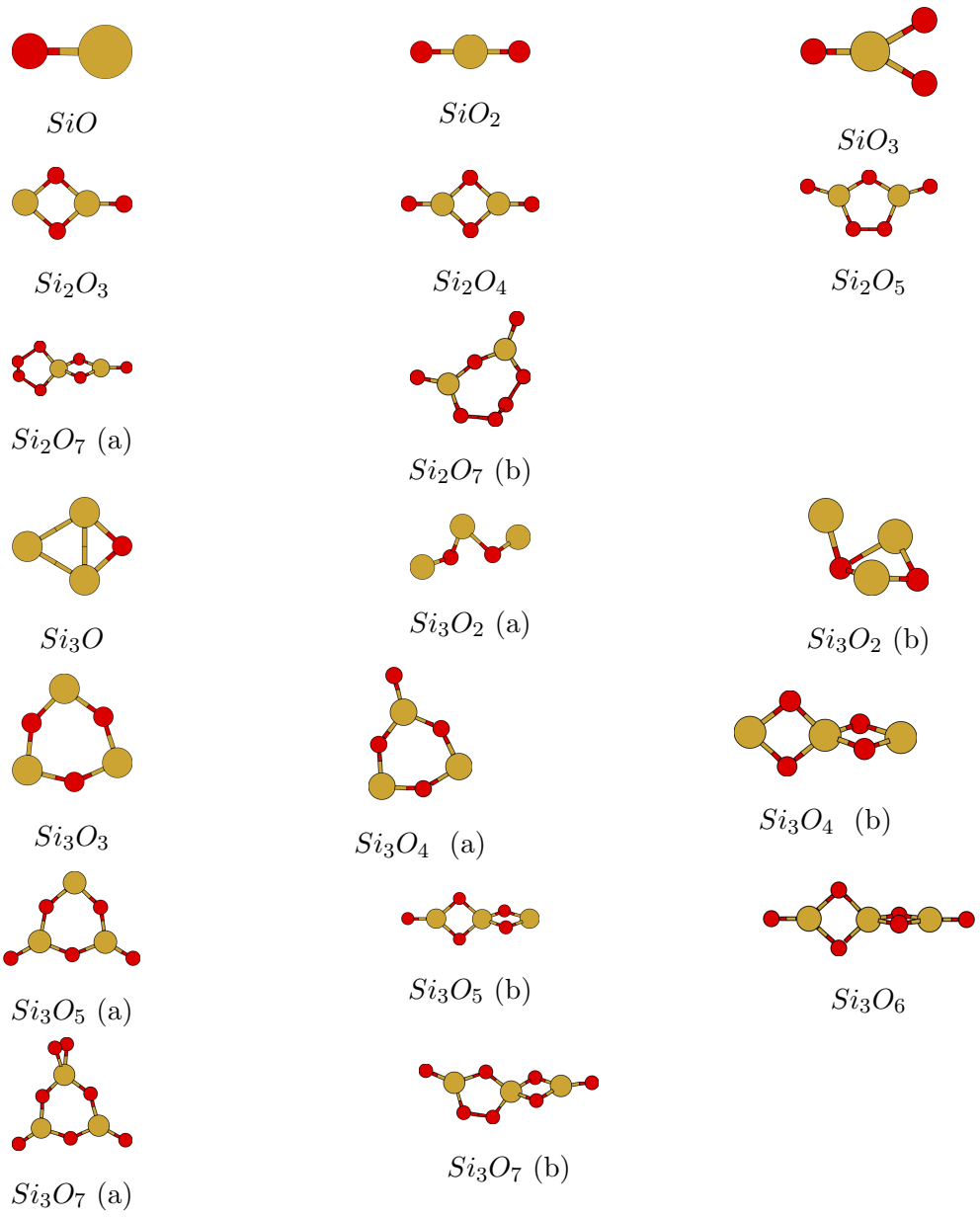

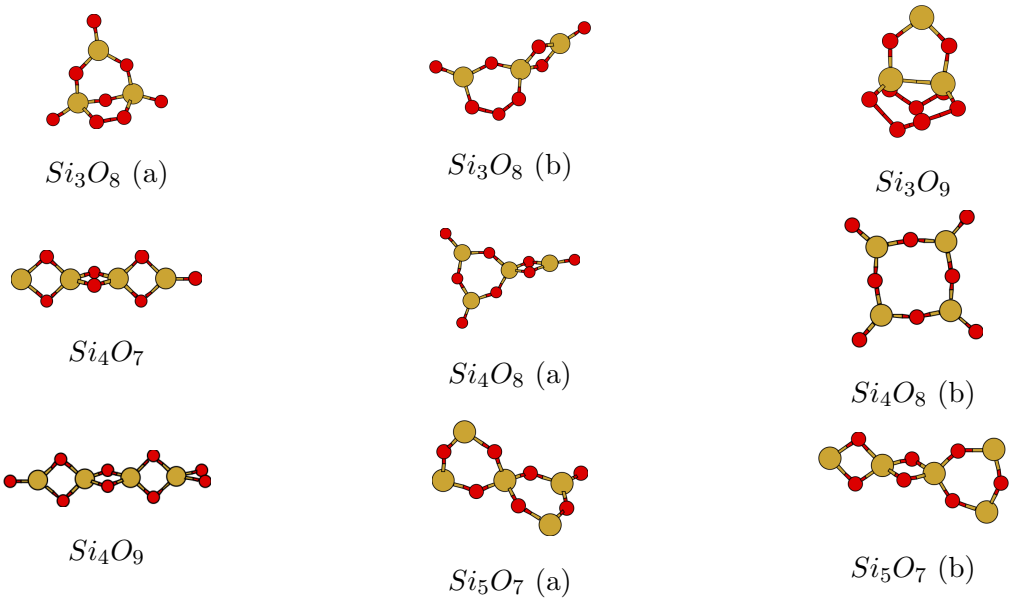

Fig. 8.1. Lowest-energy isomers for Si_xO_y clusters

We found low-lying isomers in the following cases: a planar Si_4O_8 with 8 alternating Si and O atoms forming a ring and four oxygen atoms attached to each Si atom. This structure is 0.58 eV above the GM. For Si_3O_8, we find a non planar structure with a two Si and three O atoms forming a hexagon and rhombus attached to one side and an O atom on the other. This structure is 0.22 eV higher in energy than the GM. For Si_5O_7, we find a non planar structure with two Si-O rhombuses attached to hexagon on one side. This structure is 0.54 eV higher in energy than the GM. For Si_3O_4, our calculations give a non-planar structure with two connected rhombi, 0.24 eV above the GM. In case of Si_2O_7, we get two Si and five O atoms forming a non planar ring and two O atoms attached to each of the Si atom. This structure is 0.44 eV above the GM. For Si_3O_7, a hexagon with an oxygen atom attached to one

side and a nonplanar rhombus attached to other, is a low lying isomer 0.35 eV above the GM. For Si_3O_5, we get two non planar rhombi connected to each other and an O atom attached to Si atom on one side. This structure is 0.38 eV above the GM. For Si_3O_2, a nonplanar structure with two Si atom and two O atoms connected to form a closed structure and 3rd Si atom attached to one of the O atoms is the low lying isomer. This structure is 0.43 eV above the GM. We see in Fig. 8.1 that Si-Si and O-O bonds are disfavored, and some structural units are common to many GM: 4-membered rings (Si_2O_2) and 6-membered rings (Si_3O_3) with or without capping O atoms; Si-sharing 4-membered rings at 90° degrees of each other, with the shared Si atom in an approximate tetrahedral geometry (e.g., Si_4O_7 and Si_4O_9); and O_2 units in $Si_xO_{(2x+1)}$ $(x = 2, 3, 4)$.

SiO_n, **$(n = 1 - 3)$**: We calculate an equilibrium bond length of 1.58 Å for SiO: it is close to the experimental value (1.61 Å [309]). Our calculations predict a symmetric linear structure with $D_{\infty h}$ symmetry for SiO_2. The Si−O bonds 180° apart have a bond length of 1.59 Å. This result is in agreement with earlier studies [298, 301, 303]. SiO_3 is planar and our predicted lowest energy structure is in agreement with that predicted by Lu *et al.* [303]. The Si-O bond distances for all Si_xO_y clusters are given in the table. 8.3

Si_2O_n, **$(n = 3 - 5)$**: Our calculations produce a doubly-bridged stable dimer structure for Si_2O_4. It has D_{2h} symmetry. Two of the four oxygens in this $(SiO_2)_2$ cluster form a symmetric double bridge between the silicons, while the other two are external to that rhombus. For Si_2O_3 the lowest-energy structure has an oxygen bonded to Si_2O_2 rhombus. The most stable structures for Si_2O_3 and Si_2O_4 are in

agreement with those suggested by Wang *et al.* [310]. The lowest-energy isomer for Si_2O_5 is formed by joining two oxygens on sides of a pentagon formed by two Si and three O atoms.

Si_3O_n, ($n = 5 - 7$): In the lowest energy structure of Si_3O_5, three O atoms and three Si atom form a ring and other two O atoms are joined to two Si atoms on either side of this ring. Lu *et al.* [303] in their study predicted this structure to be 1.0 eV higher in energy than the lowest-energy structure. However, the lowest-energy structure predicted by their study is 0.57 eV higher in energy than the global minima in our study. They performed structural optimizations using GAMESS [311] applying DFT with B3LYP functional [62] and 6-31G (d) basis set. The lowest-energy structure for Si_3O_6 is predicted to be D_{2d}, symmetry where four O atoms belong to double bridges and two end O atoms bonded to Si atoms. This is in agreement with earlier studies [288, 295, 298, 301]. The lowest energy structure for Si_3O_7 can be seen as capping the doubly coordinate Si atom of Si_3O_5 with a O_2 unit. Lu *et al.* [303] also obtained this structure but they found it to be 0.8 eV above their GM. GM for Si_3O_7 predicted by their study is 0.47 eV higher in energy relative to our predicted GM.

Si_4O_n, ($n = 7 - 9$): The lowest energy structure for Si_4O_7 is a rhombus chain structure with double oxygen bridges. This is consistent with the previous computational results [288, 301]. The lowest-energy structure for Si_4O_8 in our calculations is predicted to have C_{2v} symmetry. This structure is predicted to be a low energy isomer by Harkless *et al.* in their study [298]. Harkless *et al.* used additive pair interactions derived by Tsuneyuki *et al.* (TTAM) for their calculations, supplemented

with small-distance configurational constraints. Two other isomers with D_{4h} and D_{2h} symmetry are predicted to be 0.58 eV and 0.60 eV higher in energy than the lowest energy isomer. For Si_4O_9, a rhombus chain structure with one O atom on one side and an O_2 unit on the other side is predicted to be the lowest-energy structure.

Si_3O_n, **($n = 1 - 9$)** The low-energy structures of Si_3O_n clusters $(n = 1 - 9)$ are plotted in Fig 8.1. The lowest-energy structure for Si_3O has one O atom bonded to two Si atoms of Si_3 cluster. This structure is consistent with that predicted in reference [295, 301, 312]. However for Si_3O_2, the previously predicted ring structure [295, 303] is found to be 1.0 eV less stable than the most stable structure predicted by our PBE/LANL2DZ. The most stable structure for Si_3O_3 in the present study is predicted to be a planar D_{3h} ring. This result is consistent with previous studies [281, 295, 300]. The lowest-energy structure for Si_3O_4 is a ring with one oxygen attached to the side. We found two isomers (Si_3O_4 (a) and Si_3O_4 (b)). The relative energies of these two are 0.00 eV and 0.25 eV by PBE/LANL2DZ (this study), and 1.13 eV and 0.00 eV by B3LYP/6-31G (d) in the study by Lu *et al.* [303] . The most energetically favourable structure for Si_3O_5 is a planar D_{3h} ring with two oxygen atoms attached to either side of two Si atoms. The rhombus chain structure for this cluster, predicted to be most stable by other studies [288, 295, 301] is 0.38 eV higher in energy in our case. The GM for Si_3O_6 has D_{2d} symmetry and two Si-sharing 4-membered rings, each with a O capping atom. The GM of Si_3O_7 is a $(SiO)_3$ hexagon with O, O and O_2 bonded to the three Si atoms. This preference for ring structure can also be seen in the structures of Si_3O_8 and Si_3O_9.

8.3.2 Stability

Cluster	R (eV)	AE (eV)	HOMO-LUMO gap (eV)	VEA	VIP
Si_5O_7	−4.74	55.57	2.95	1.87	9.41
Si_4O_8	−3.85	53.33	3.42	1.70	14.0
Si_4O_7	−2.88	48.69	3.88	2.13	10.81
Si_4O_9	−1.71	54.86	2.82	2.98	10.51
Si_3O_5	−1.58	35.01	3.32	1.64	12.41
Si_3O_6	−1.56	38.67	3.69	2.36	11.2
Si_3O_4	−0.971	30.73	2.79	1.54	9.40
Si_3O_7	−0.493	41.27	1.85	2.62	10.49
Si_3O_3	−0.216	26.30	2.83	0.964	8.98
Si_2O_4	0.172	24.57	3.46	1.95	11.3
Si_2O_3	0.517	20.55	3.56	1.35	12.00
Si_3O_8	0.706	43.75	2.69	6.19	10.57
SiO	1.42	7.27	4.29	0.49	11.53
Si_2O_5	1.55	26.86	2.68	0.57	11.08
SiO_2	1.62	10.75	3.35	1.22	11.9
Si_2O_7	3.32	32.44	2.41	2.75	11.07
SiO_3	3.36	12.69	1.86	1.69	14.4
Si_3O_2	4.77	17.64	1.68	1.27	8.08
Si_3O_9	6.12	42.01	0.52	4.04	9.97
Si_3O	6.54	12.20	1.04	1.87	8.38

Table 8.1: RITS (R), AE, HOMO-LUMO gap, VEA and VIP for Si-oxide clusters

Table 8.1 shows the RITS, AE, HOMO-LUMO gap VEA and VIP values for all the Si_xO_y clusters. For a given x, the RITS of Si_xO_y is at, or near, a minimum when $y = 2x$: the 1:2 stoichiometric clusters are generally more stable. The EAs lie

between 1 and 2 eV for stoichiometric clusters, and they increase with the addition of an oxygen atom. A few IPs and EAs have been measured and may be compared to our calculations (in parentheses). The IP of SiO is 11.43 [313] (11.53). The experimental EAs are 1.96 for Si_3O [314] (1.87), 1.05 for Si_3O_4 [314] (1.54), and above 3.50 for Si_3O_6 [314] (2.36). The poor agreement for Si_3O_6 could be caused by having a wrong GM, or the intrinsic error of PBE/LANL2DZ method for the EA, or the vertical approximation.

We now discuss the stability of $(SiO_2)_n$ clusters. One stability criterion is energies of reactions such as disproportionation reaction. We define the disproportionation energy D (x,y) as

$$D\ (x,y) = 2E_{Si_xO_y} - \ (E_{Si_xO_{y-1}} + E_{Si_xO_{y+1}}) \tag{8.1}$$

Cluster	D (eV)
D (4,8)	3.11
D (3,6)	1.06
D (2,4)	1.73
D (1,2)	1.59

Table 8.2: Disproportionation energy (in eV) for Si_xO_y clusters

The disproportionation energies are all positive which indicates that the stoichiometric clusters are favoured over the non-stoichiometric ones. The disproportionation energy is highest for Si_4O_8 indicating a relatively high stability. This is what is

indicated by RITS. The disproportionation energy is lowest for Si_3O_6. Disproportionation energies compare only 3 cluster species at a time. The RITS compare the energy of every cluster to those of all other clusters and give different information. In general, bigger clusters have smaller (ie more negative) RITS because of their smaller surface energy per atom. For a given m, the RITS of Si_xO_y normally increase in the order $x = 2y$, $x = 2y - 1$, and $x = 2y + 1$. The diatomic SiO has an unusually low RITS for its size.

8.3.3 Electronic properties

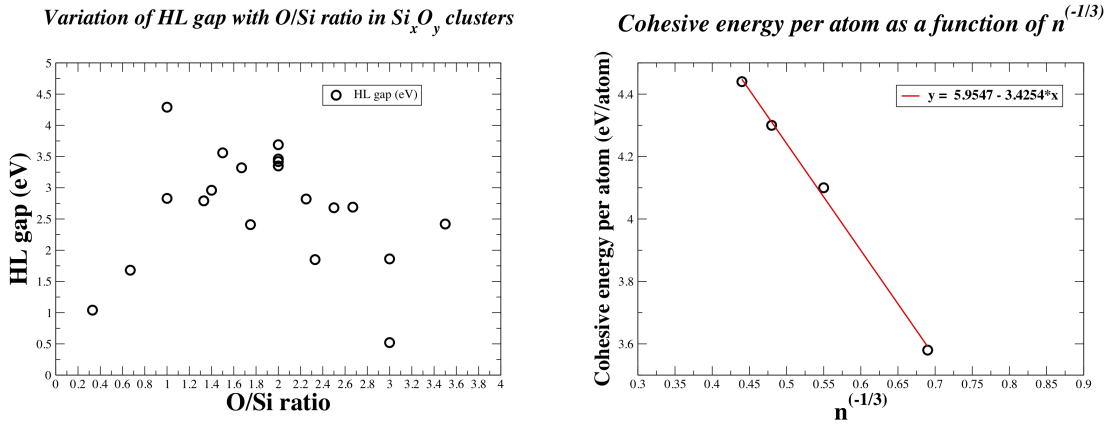

(a) **(b)**

Fig. 8.2. (a) HOMO-LUMO gap as a function of O:Si ratio and (b) Cohesive energy per atom as a function of $n^{-1/3}$

Fig 8.2 (a) shows the variation of the HOMO-LUMO gap with the O:Si ratio in Si_xO_y clusters. SiO has the largest HOMO-LUMO gap of 4.29 eV. For $(SiO_2)_n$ clusters, the HOMO-LUMO gap increases with size up to $n = 3$. The HOMO-LUMO gap decreases with increasing oxygen concentration in Si_xO_y clusters. For Si-rich

and stoichiometric clusters, the HOMO-LUMO gap scatters around 3 eV with the exception of Si_4O_7 (2.41 eV).

The difference in the gap among these small clusters may bring insight into the optical properties of materials with embedded silicon nanoparticles. When the local stoichiometry of these clusters is altered, it causes a change in the value of the HOMO-LUMO gap. As assumed by Nayak *et al.* [301], when the value of the gap decreases to that corresponding to visible light, photoluminescence becomes possible.

The atomization energies (AE's) for Si_xO_y clusters are given in table 8.1. We fitted cohesive energies $E_{coh}\ (Si_xO_y) = \text{AE}\ (Si_xO_y)/\ (x+y)$ to the function,

$$E_{coh,fit} = a + bn^{-1/3} \tag{8.2}$$

where $n = x + y$.

Ignoring any detail about geometric structure, one expects an increase of the cohesive energy with the number of atoms 'n' as,

$$E_{coh} = E_{coh,bulk} - a_{surface}n^{-1/3} - a_{edge}n^{-2/3} - a_{corner}n^{-1} \tag{8.3}$$

So, by plotting E_{coh} versus $n^{-1/3}$, particularly stable clusters can be identified. We obtained the value of $E_{coh}/atom$ for Si_xO_y clusters = 5.95 eV/atom. Lanord *et al.* in their theoretical study on (SiO_2) polymorphs, found a value of 8.222 (eV/atom) for α- quartz. They used DFT implemented in the Vienna Ab initio Simulation Package (VASP) [315, 316] and PBEsol [59, 317]to describe the exchange correlation.

Cluster	Si-O bond distances (Å)
Si_4O_9	1.59 (1), 1.73 (2),1.75 (6) 1.76 (4),1.77 (2)
Si_4O_8	1.58 (3), 1.68 (2), 1.69 (4), 1.75 (2), 1.77 (2)
Si_4O_7	1.58 (2), 1.74 (2), 1.76 (4), 1.75 (2), 1.77 (2)
Si_3O_8	1.58 (2),1.67 (1),1.68 (1),1.75 (1),1.76 (1),1.77 (3),1.78 (1)
Si_3O_9	1.72 (2),1.73 (1),1.75 (1),1.76 (1),1.80 (1),1.83 (1)
Si_5O_7	1.58 (1),1.69 (3),1.70 (3),1.73 (1),1.74 (5)
Si_3O_4	1.59, 1.74 (2), 1.75 (2), 1.70 (2)
Si_2O_7	1.58, 1.76 (2), 1.77 (4)
Si_3O_7	1.58 (2), 1.68 (2), 1.69 (4), 1.73 (2)
Si_3O_6	1.58 (2), 1.75 (4), 1.77 (4)
Si_3O_5	1.58 (2),1.70 (4), 1.74 (2)
Si_2O_5	1.58 (2),1.71 (2), 1.77 (2)
Si_2O_4	1.58 (2), 1.77 (4)
Si_2O_3	1.58 (1), 1.77 (2)
SiO_3	1.58 (1), 1.74 (2)
Si_3O_2	1.71 (2),1.97 (2)
Si_3O	1.82 (2)
Si_3O_3	1.74 (6)
SiO_2	1.59 (2)
SiO	1.58

Table 8.3: Si-O bond distances in Si-oxide clusters, the number in parenthesis indicates the number of bonds with this bond length.

The optimized Si-O bond distances are reported in table 8.3. Most of them fall in the range from 1.58 to 1.78 Å. In general, singly coordinated oxygen atoms have a bond length to Si close to 1.58 Å, and doubly coordinated oxygen atoms have bond

lengths ranging between 1.70 and 1.80 Å.

To study the effect of varying Si atom number while keeping the number of O atoms unchanged, we studied Si_2O_7, Si_3O_7, Si_4O_7 and Si_5O_7 clusters.

Cluster	O:Si ratio	HOMO-LUMO gap (eV)	VEA (eV)	VIP (eV)
Si_2O_7	3.5	2.41	2.75	11.07
Si_3O_7	2.3	1.85	2.62	10.49
Si_4O_7	1.75	3.88	2.13	10.81
Si_5O_7	1.4	2.95	1.87	9.41

Table 8.4: HOMO-LUMO gap (eV), Vertical electron affinity (eV) and Vertical Ionization potential for Si_xO_7 clusters

The HOMO-LUMO gap varies non-monotonically with increasing Si content in Si_xO_7 clusters. It reaches a maximum at the ratio 1.75 which is close to the stoichiometric ratio of silicon oxide clusters. The calculated electron affinity decreases from Si_2O_7 to Si_5O_7. Higher EA values for the oxygen rich clusters are expected and are the result of dominance of oxygen orbitals in forming the HOMO's of these clusters. We are not aware of any experimental or theoretical values of vertical electron affinity and vertical ionization potential for Si_2O_7, Si_3O_7, Si_4O_7, Si_5O_7. RITS is more negative for clusters with O:Si ratio closer to 2, indicating a higher stability for these clusters.

8.3.4 $\mathbf{Si_3O_y}$, $(y = 1 - 9)$

We examined the structures and stability of Si_3O_y $(y = 1-9)$ clusters. Our purposes were (i) to compare the structures of Si_3O_y clusters at different O/Si ratio, (ii) study

the effect of changing oxygen concentration while keeping the number of Si atoms fixed, and (iii) study the relative stability of these clusters by using RITS and to study the trends in the stability and electronic properties of these clusters.

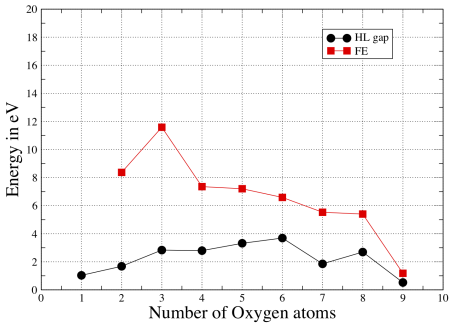

(a)

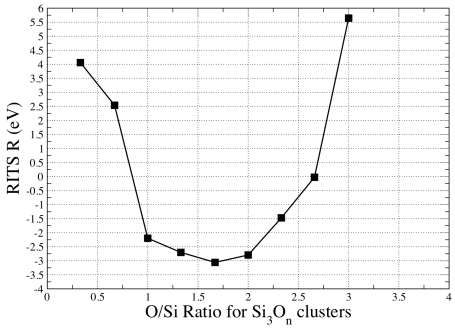

(b)

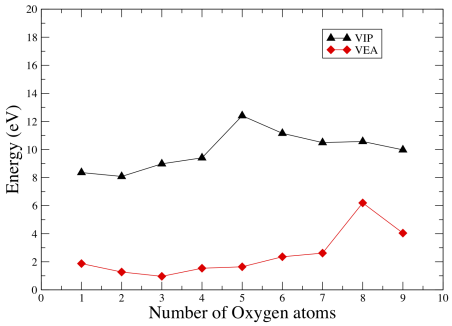

(c)

Fig. 8.3. (a) HOMO-LUMO gap (eV) and Fragmentation energy (eV) of Si_3O_y clusters, (b) Variation of RITS with O/Si ratio (c) VIP and VEA for Si_3O_y clusters

We define the fragmentation energy FE as the energy required to remove one oxygen atom, that is

$$FE\ (Si_3O_y) = FE\ \ (3, y) = E\ (O) + E\ (Si_3O_{y-1}) - E\ (Si_3O_y)$$

FE is either the energy required to remove one oxygen atom from Si_3O_y or the incremental energy for adding one oxygen atom to the Si_3O_{y-1} system. Because of that, the peaks observed in the plot of FE vs the number of oxygen atoms 8.3a in the Si_3O_y cluster are an indication of cluster stability. Clusters with high fragmentation energy are particularly stable, while large HOMO-LUMO gaps are indicative of chemical inertness. Si_3O_9 is the least stable using both criteria. The fragmentation energy is highest for the Si_3O_3 cluster. This may be attributed to the extra stability associated with the Si_3O_3 cluster due to closed atomic shell. Overall, FE (3,y) decreases with increasing y, except for a maximum at Si_3O_3. The very large FE (3,3) is apparently a consequence of the stable, high-symmetry structure, as well as the low stability of the chain-shaped Si_3O_2 (RITS: 4.77 eV). The HOMO-LUMO gap increases sharply by 1.2 eV from Si_3O_2 to Si_3O_3. Si_3O_6 has the largest HOMO-LUMO gap in the set. This is understandable as all the bonds in the stoichiometric cluster are saturated. There are odd-even oscillations in the HOMO-LUMO gap as a function of number of oxygen atoms.

We plot RITS as a function of the O/Si ratio in Si_3O_y clusters (Fig.8.3 (b)). RITS indicates the relative stability of clusters in the set. Clusters with O/Si ratio near 2 are more stable as compared to other clusters in the set. As the O:Si ratio increases above 2, the clusters become less stable and the cluster with highest O:Si ratio of 3 in the set is the most unstable cluster predicted by RITS. Clusters having lower values of fragmentation energy and smaller HOMO-LUMO gaps are also predicted to be less stable by RITS.

8.4 Conclusion

We have calculated the equilibrium geometries and electronic structure of Si_xO_y clusters using DFT-PBE/LANL2DZ. The structures of stable clusters are diverse and do not suggest a simple growth principle. Rhombus chain structure and ring structure emerge as the structural motifs for the most stable structures. All of the stoichiometric clusters are stable against the disproportionation reaction. The HOMO-LUMO gap has a large value for Si rich and stoichiometric clusters and it decreases for O rich clusters. The relative stability comparison for these clusters suggests Si_5O_7 to be most stable in the set. The RITS values indicate that the energetically favored stoichiometries in Si_xO_y clusters $(x, 2x)$ and $(x, 2x-1)$, which are very close, then $(x, 2x+1)$, and then stoichiometries that deviate further from the 1:2 ratio.

Chapter 9

Metal oxides

9.1 Introduction

The study of clusters allows a better understanding of the evolution of the main physical properties of the systems ranging from the atom to the crystal. These studies also provide an interesting way to develop materials with varying properties by changing size and shape. Properties and structures of metal oxides could be entirely different in small clusters than the bulk. Clusters of metal oxides are stable with respect to reaction with atmospheric oxygen. This gives them a practical advantage over metal clusters.

Here we report a comparative study of the structures, stabilities and properties of some alkaline earth metal oxides, alkali metal oxides, transition metal oxides, and semimetal oxides as well. We chose elements of groups I, II, XI, XII, XIII and XIV, with valence ranging from 1 to 4, in order to study trends in qualitatively different metal oxides . We studied $(Li_2O)_n$, $(K_2O)_n$, $(MgO)_n$, $(CaO)_n$, $(Cu_2O)_n$, $(CuO)_n$, $(Ag_2O)_n$, $(ZnO)_n$, $(Al_2O_3)_n$ and $(SiO_2)_n$.

9.2 Computational Methods

We performed global optimization of geometries using the DFT energy, the TSDS optimization method and the following option in the Gaussian software: PBE for exchange correlation and LANL2DZ basis set. We typically did 50 (n)+200 TSDS iterations for n-atom clusters. We then selected between 5 (for small n) and 20 (for large n) lowest energy clusters and performed local optimization by Broyden–Fletcher–Goldfarb–Shanno (BFGS) algorithm.

9.3 Lowest energy isomers

The putative global minima we found for the different cluster species are shown in Fig. 9.1 to 9.10. The low-energy structures generally show alternating metal and oxygen atoms. Metal-metal bonds are common only in species with $(M_2O)_n$ stoichiometry or with large metal atoms (Ca). This is expected on account of the strong ionic bonding in these clusters and the opposite charges on M and O atoms.

9.3.1 $(Li_2O)_n, n = 1 - 4$

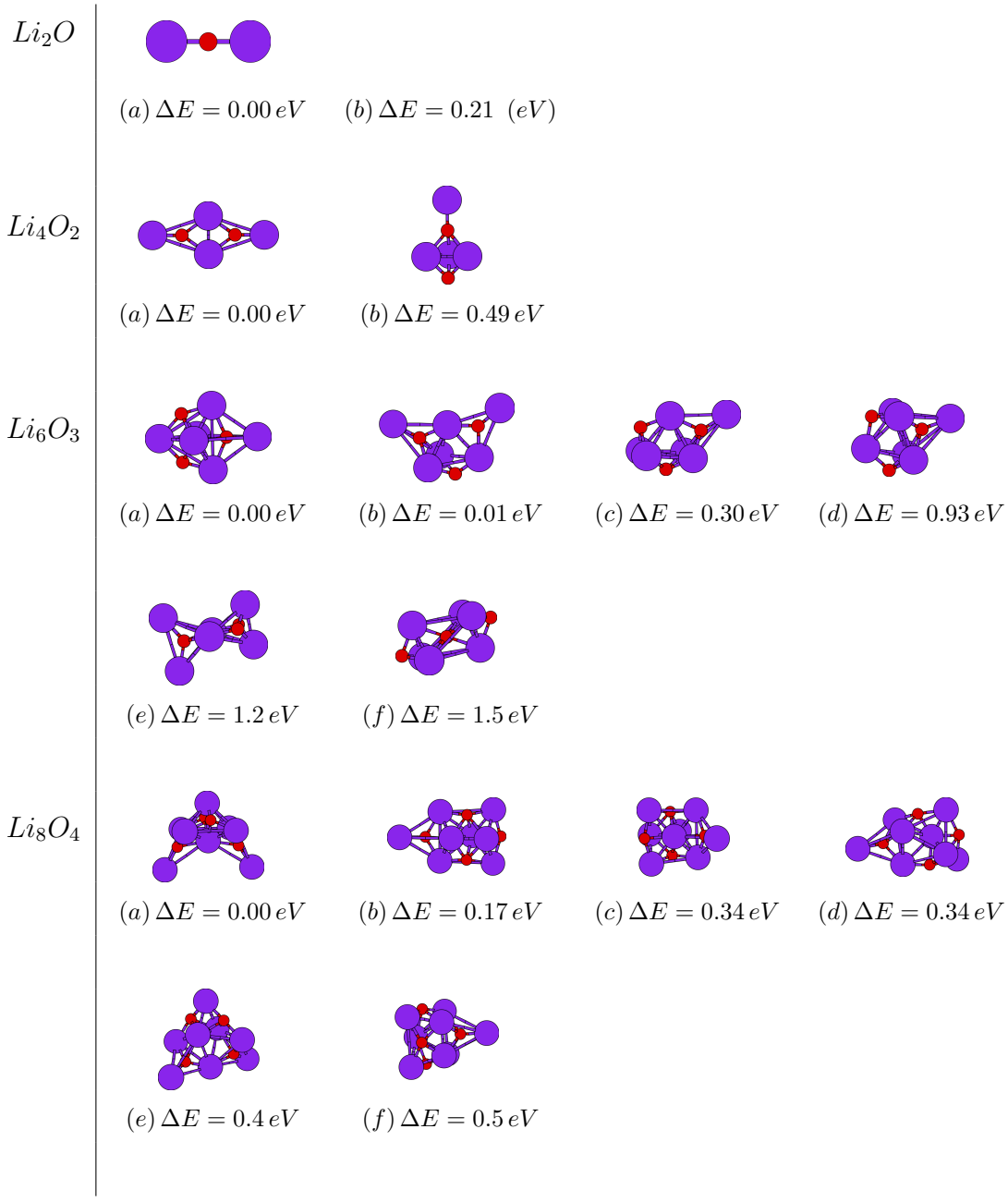

Fig. 9.1. Low-energy isomers of $(Li_2O)_n$

9.3.2 $(MgO)_n, n = 1 - 6$

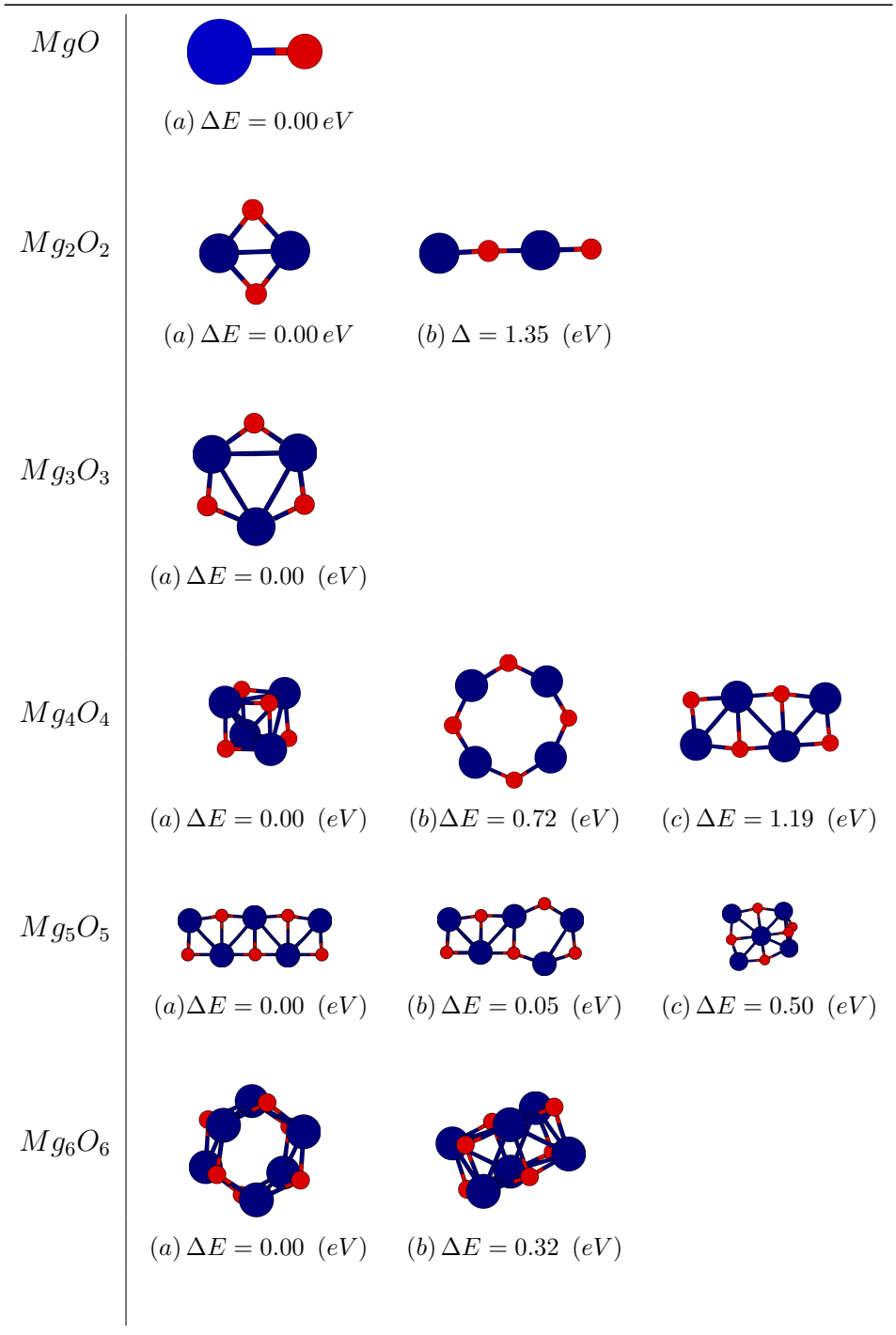

Fig. 9.2. Low-energy isomers of $(MgO)_n$

9.3.3 $(Al_2O_3)_n, n = 1 - 3$

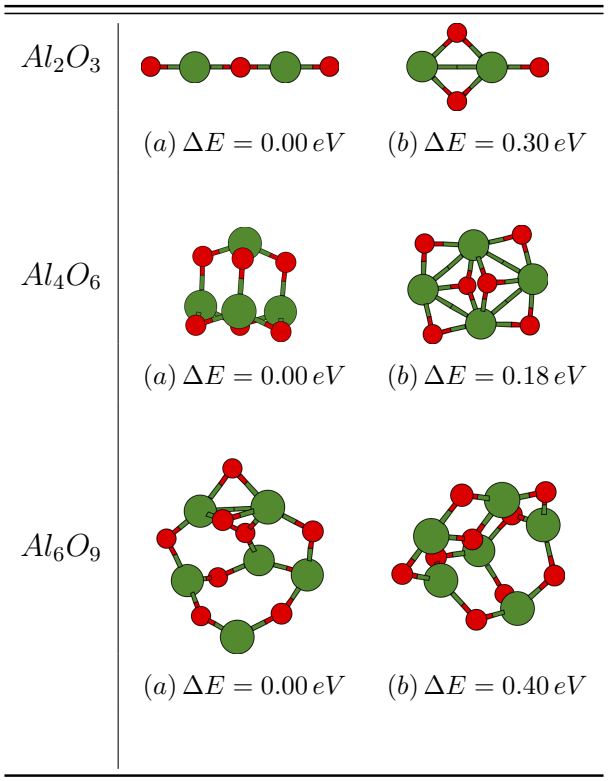

Fig. 9.3. Low-energy isomers of $(Al_2O_3)_n$

9.3.4 $(SiO_2)_n$, $n = 1 - 4$

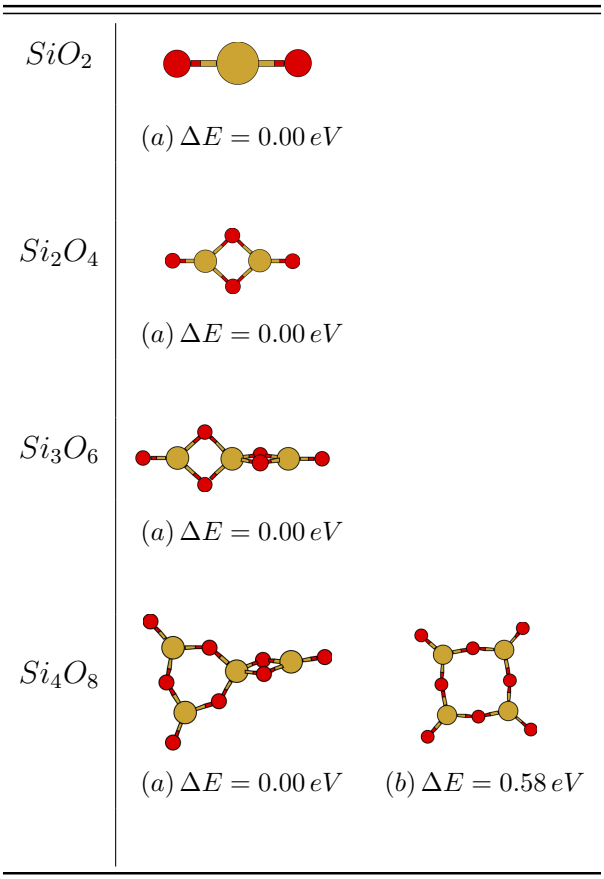

Fig. 9.4. Low-energy isomers of $(SiO_2)_n$

9.3.5 $(K_2O)_n, n = 1 - 4$

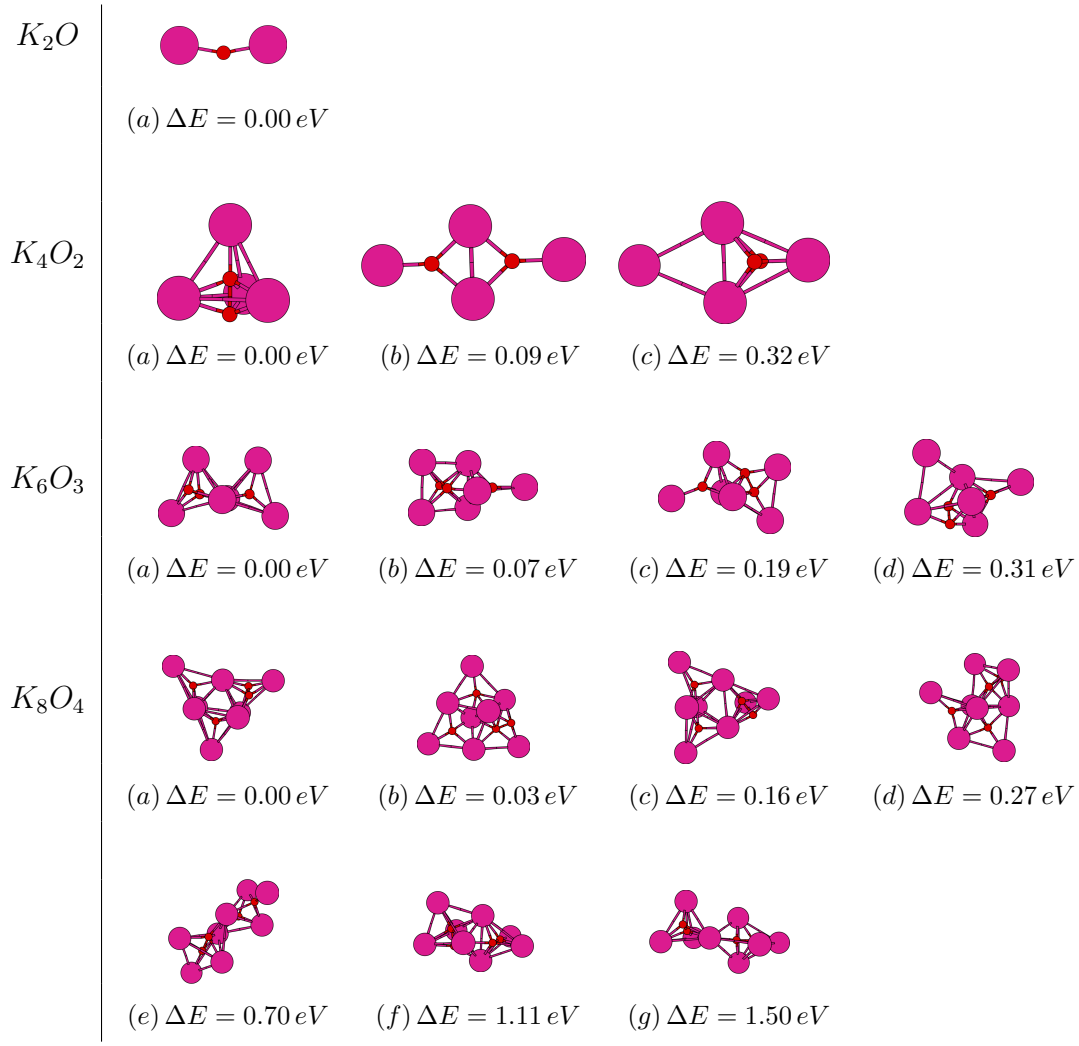

Fig. 9.5. Low-energy isomers of $(K_2O)_n$

9.3.6 $(CaO)_n, n = 1 - 6$

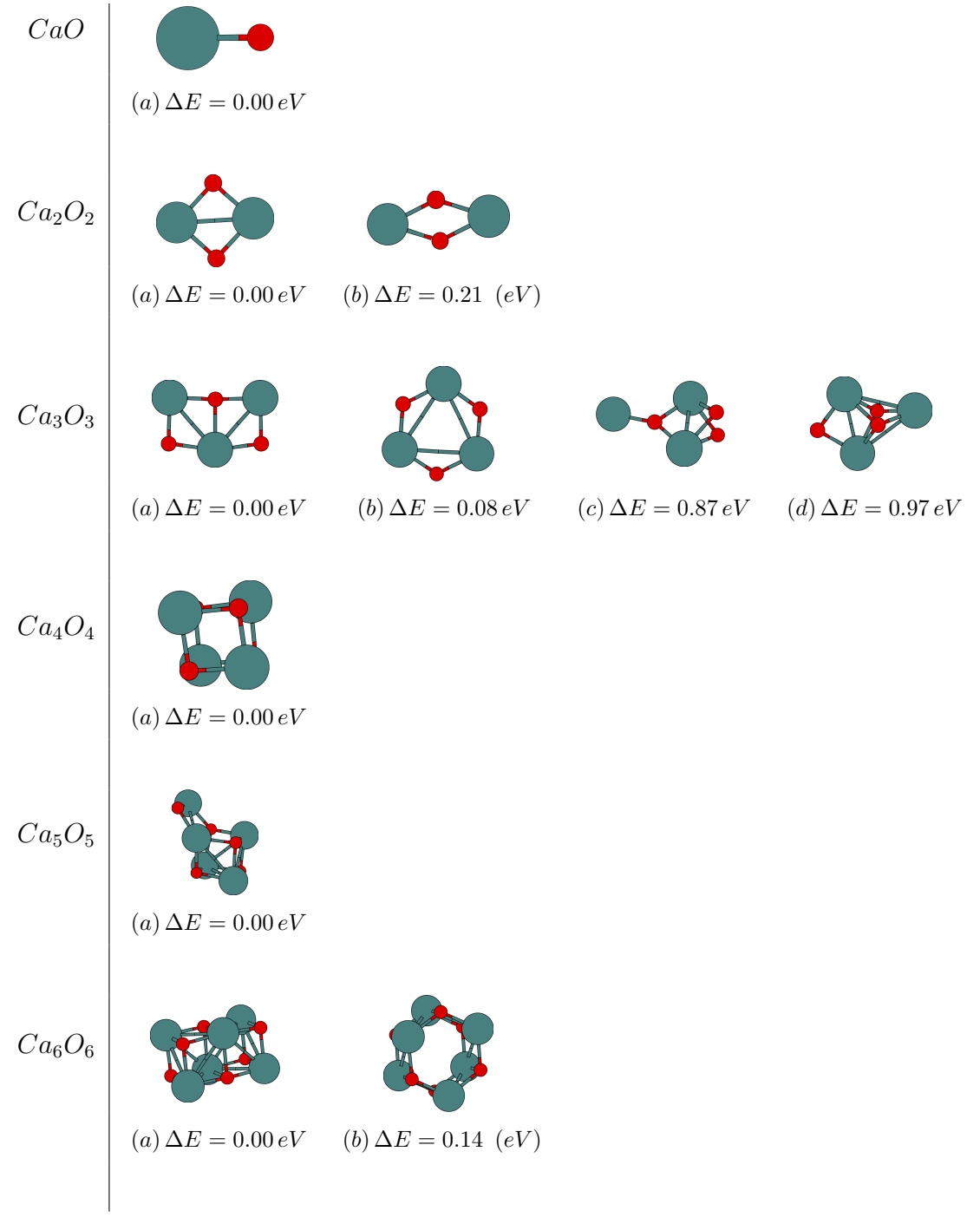

Fig. 9.6. Low-energy isomers of $(CaO)_n$

9.3.7 $(Cu_2O)_n, n = 1 - 4$

Cu_2O

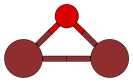

$(a)\,\Delta E = 0.00\,eV$

Cu_4O_2

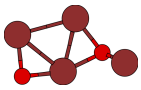

$(a)\,\Delta E = 0.0\,eV$

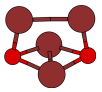

$(b)\,\Delta E = 0.06\,eV$

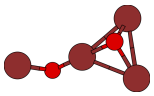

$(c)\,\Delta E = 0.14\,eV$

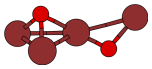

$(d)\,\Delta E = 0.22\,eV$

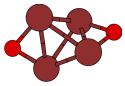

$(e)\,\Delta E = 0.44\,eV$

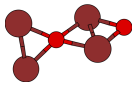

$(f)\,\Delta E = 0.52\,eV$

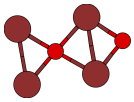

$(g)\,\Delta E = 0.65\,eV$

Cu_6O_3

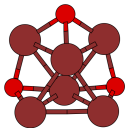

$(a)\,\Delta E = 0.00\,eV$

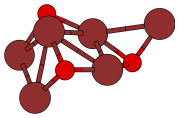

$(b)\,\Delta E = 0.30\,eV$

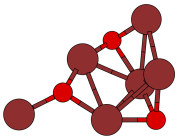

$(c)\,\Delta E = 0.40\,eV$

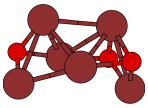

$(d)\,\Delta E = 0.70\,eV$

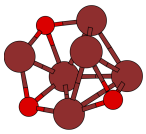

$(e)\,\Delta E = 0.81\,eV$

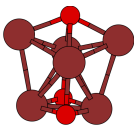

$(f)\,\Delta E = 0.91\,eV$

Cu_8O_4	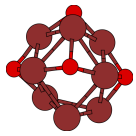 $(a)\,\Delta E = 0.00\,eV$ 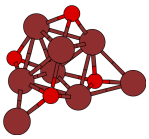 $(b)\,\Delta E = 0.18\,eV$ 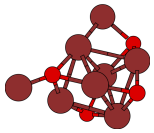 $(c)\,\Delta E = 0.32\,eV$ 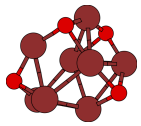 $(d)\,\Delta E = 0.40\,eV$ 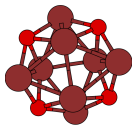 $(e)\,\Delta E = 0.79\,eV$

Fig. 9.7. Lowest energy isomers of $(Cu_2O)_n$

9.3.8 $(CuO)_n, n = 1 - 6$

CuO

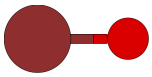

$(a)\ \Delta E = 0.00\, eV$

Cu_2O_2

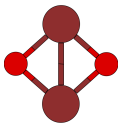

$(a)\ \Delta E = 0.00\, eV$

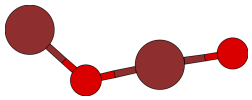

$(b)\ \Delta E = 0.99\, eV$

Cu_3O_3

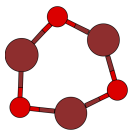

$(a)\ \Delta E = 0.00\, eV$

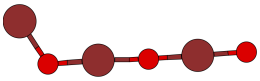

$(b)\ \Delta E = 0.77\, eV$

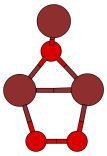

$(c)\ \Delta E = 1.04\, eV$

Cu_4O_4

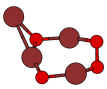

$(a)\ \Delta E = 0.00\, eV$

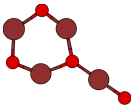

$(b)\ \Delta E = 0.34\, eV$

Cu_5O_5

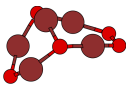

$(a)\ \Delta E = 0.00\, eV$

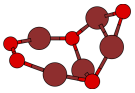

$(b)\ \Delta E = 0.07\, eV$

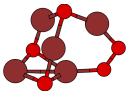

$(c)\ \Delta E = 0.38\, eV$

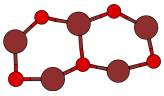

$(d)\ \Delta E = 0.51\, eV$

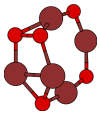

$(e)\ \Delta E = 0.89\, eV$

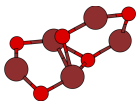

$(f)\ \Delta E = 1.06\, eV$

Cu_6O_6	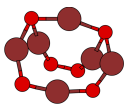 $(a)\,\Delta E = 0.00\,eV$ 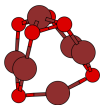 $(b)\,\Delta E = 0.13\,eV$ 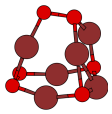 $(c)\,\Delta E = 0.20\,eV$ 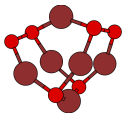 $(d)\,\Delta E = 0.37\,eV$  $(e)\,\Delta E = 0.46\,eV$ 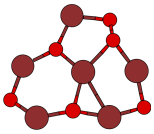 $(f)\,\Delta E = 0.86\,eV$

Fig. 9.8. Low-energy isomers of $(CuO)_n$

9.3.9 $(ZnO)_n, n = 1 - 6$

ZnO	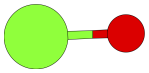		
	$(a)\,\Delta E = 0.00\,eV$		
Zn_2O_2	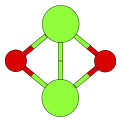	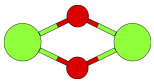	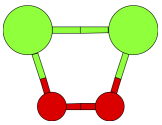
	$(a)\,\Delta E = 0.00\,eV$	$(b)\,\Delta = 1.45\ \ (eV)$	$(b)\,\Delta = 1.56\ \ (eV)$
Zn_3O_3	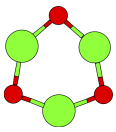		
	$(a)\,\Delta E = 0.0\ \ (eV)$		
Zn_4O_4	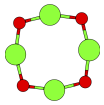	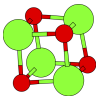	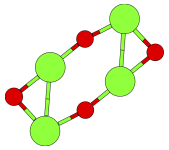
	$(a)\,\Delta E = 0.00\ \ (eV)$	$(b)\,\Delta E = 0.18\ \ (eV)$	$(c)\,\Delta E = 0.77\ \ (eV)$
Zn_5O_5	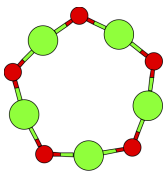	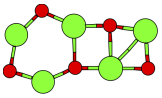	
	$(a)\,\Delta E = 0.00\ \ (eV)$	$(b)\,\Delta E = 0.32\ \ (eV)$	

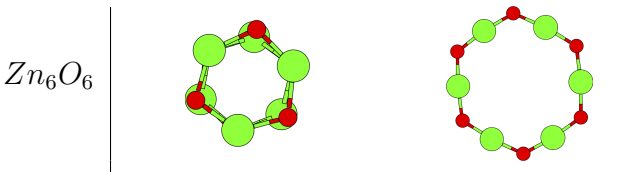

Fig. 9.9. Low-energy isomers of $(ZnO)_n$

9.3.10 $(Ag_2O)_n, n = 1 - 4$

Ag_2O

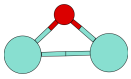

$(a)\ \Delta E = 0.00\, eV$

Ag_4O_2

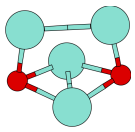

$(a)\ \Delta E = 0.00\, eV$

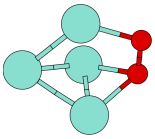

$(b)\ \Delta E = 0.10\, eV$

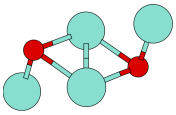

$(c)\ \Delta E = 0.18\, eV$

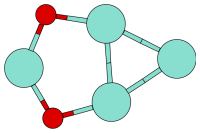

$(d)\ \Delta E = 0.55\, eV$

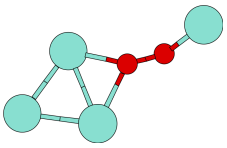

$(e)\ \Delta E = 0.57\, eV$

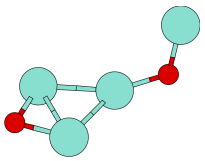

$(f)\ \Delta E = 0.74\, eV$

Ag_6O_3

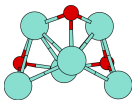

$(a)\ \Delta E = 0.00\, eV$

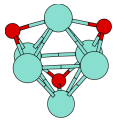

$(b)\ \Delta E = 0.02\, eV$

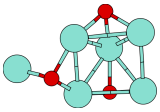

$(c)\ \Delta E = 0.04\, eV$

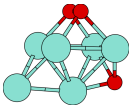

$(d)\ \Delta E = 0.24\, eV$

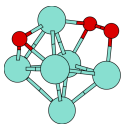

$(e)\ \Delta E = 0.48\, eV$

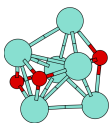

$(f)\ \Delta E = 0.60\, eV$

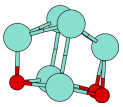

$(g)\ \Delta E = 0.96\, eV$

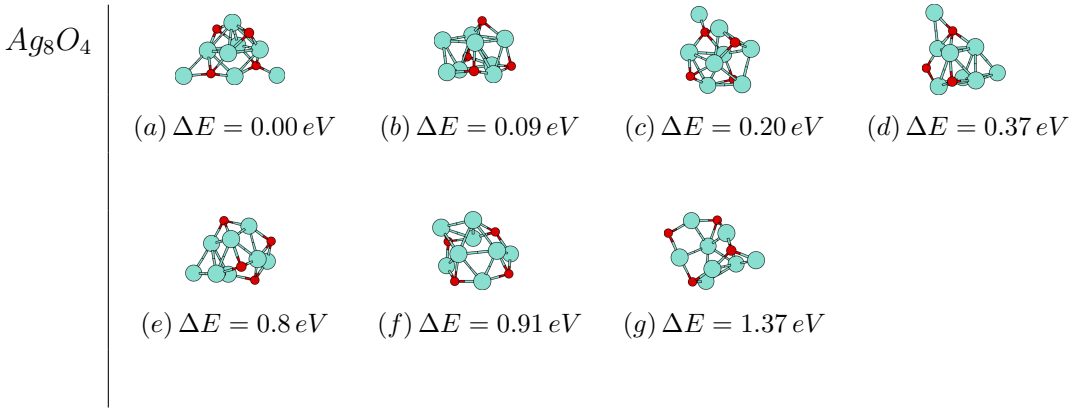

Fig. 9.10. Low-energy isomers of $(Ag_2O)_n$

9.4 Discussion

There are similarities between clusters $(M_xO_y)_n$ with the same ratio x/y. The energetically favored structures of $x/y = 2$ clusters ($(Li_2O)_n$, $(K_2O)_n$, $(Ag_2O)_n$, $(Cu_2O)_n$) often have a polytetrahedral metal framework with O atoms in interstitial or capping positions. At $x/y = 1$, ($(ZnO)_n$, $(MgO)_n$, $(CaO)_n$, $(CuO)_n$) the low-energy structures are planar or quasi-planar rings at small n. For larger n, the GM are stacks of 4-membered rings (ie, cubes, Mg and Ca) or 6-membered rings (Ca, Zn); $(CuO)_n$ are different in that they remain quasiplanar until $n = 6$. At $x/y = 2/3$ (Al), the structures are cage-like and show several 4- and 6-membered rings with near perfect alternation of Al and O atoms. At $x/y = 1/2$ (Si), the common structural motifs are rings, 90-degree angles, and O atoms that have a coordination number of either one or two.

$(\mathbf{Li_2O})_\mathbf{n}$ clusters. The GM we found for Li_8O_4 is in agreement with Finocchi *et al.* [318]. However, Yuan and Cheng, who used the TPSSh functional and a 6-

311+G* basis set, in their study of Li clusters predict this to be an isomer with an energy difference of 0.15 eV above the global minimum. The Li-O bond lengths are 1.67 Å (2),1.78 Å (4),1.82 Å (2), 1.86 Å (4),2.05 Å (2),2.08 Å (2). GM for all other $(Li_2O)_n$ clusters are in agreement with other studies [318, 319]. The GM we found for Li_4O_2 is planar with D_{2h} symmetry. Li_6O_3 has a C_{2v} symmetry. This is in agreement with previous studies. [318, 319]

$(MgO)_n$ clusters. The lowest-energy structure for Mg_6O_6 in our calculations is predicted to be hexagonal prism. This is agreement with other studies [320, 321]. Its $2 \times 2 \times 3$ cubic isomer is 0.32 eV higher in energy than the GM. The MgO bond lengths are 1.92 in the hexagonal planes and 2.02 between the two hexagons. The Mg-O bond length is 1.97 Å in cubic isomer of Mg_6O_6. The structure obtained for Mg_6O_6 is in agreement with that predicted by Batra *al.* [320] and Chen *et al.* [321]. The GM we found for Mg_5O_5 is ladder shaped which is as predicted by Batra *et al.* [320] but different from Chen *et al.* [321]. Mg_4O_4 is a cube with a Mg-O bond length of 1.98 Å. The Mg-Mg bond length is 2.70 Å: this is much shorter than the Mg-Mg distance in Mg bulk metal, 3.20 Å. These results are in agreement with Batra *et al.* [320] and Chen *et al.* [321]. Mg_3O_3 is a distorted hexagon with a Mg-O bond length of 1.85Å and Mg-Mg bond length of 2.99 Å . Mg_2O_2 is rhombus shaped with a Mg-O bond length of 1.90 Å and Mg-Mg bond length of 2.50 Å. This is in agreement with the study of Batra *et al.* [320]. The Mg-O bond length in linear MgO is 1.80 Å. The experimental bond length for Mg-O is 1.749 Å [322, 323, 324]. HOMO-LUMO-gap (9.2) increases with increasing n up to $n = 3$, it decreases for $n = 4$ and starts increasing again. The HOMO-LUMO gap is largest for $n = 3$ and 6. For bulk MgO,

the experimental value of the band gap is 7.8 eV [325].

$(\mathbf{Al_2O_3})_\mathbf{n}$ clusters. The lowest-energy configuration of Al_2O_3 is a linear and forms singlet state. Its isomer, a rhombus with an oxygen atom attached to one of the Al atoms is 0.3 eV higher in energy. It has triplet state. This result agrees with the studies by Fernandez [247], Sun and coworkers [85], Nemukhin [326] and Solornonik [327] who found a linear structure as the global minimum (GM). However, this result disagrees with calculations by Li [239], Rahane [241], Sharipov [328], Woodley [244] and their coworkers. They predicted the rhombus structure to be the GM for Al_2O_3. The Al-O bond lengths are 1.67 Å and 1.71 Å

The global minima for $(Al_2O_3)_2$ is a cage with four Al atoms forming a tetrahedron and O atoms capping the edges of the tetrahedron. The Al-O bond length in this structure is 1.79 Å. This configuration has a T_d symmetry and is a singlet. This result agrees with earlier studies [85, 239, 241, 328, 247]. Our TSDS algorithm missed the GM. So the starting geometry for Al_4O_6 was taken to be the lowest-energy structure predicted in earlier studies. The optimized structure with this geometry was found to be 0.18 eV lower in energy than our initially predicted GM. This is the structure that we report in our results. Another isomer formed by linking four planar Al atoms with O atoms placed on sides linking Al atoms is predicted to be lowest-energy isomer by Woodley [244]. In our case, it is 0.18 eV higher in energy than the lowest-energy isomer. In the case of $(Al_2O_3)_3$, we find two isomers within 0.4 eV. The lowest-energy isomer for $(Al_2O_3)_3$ has C_1 symmetry. This structure is in agreement with Woodley [239, 244]. This is followed by an isomer with C_{2v} symmetry. This structure is consistent with the results by Sharipov *et al.* [328]. The Al-O bond lengths range

from 1.74 Å to 2.02 Å.

$(\mathbf{SiO_2})_\mathbf{n}$ clusters. Our calculations predict a symmetric linear structure with $D_{\infty h}$ symmetry for SiO_2. The Si−O bonds 180° apart have a bond length of 1.5895 Å. This result is in agreement with earlier studies by Harkless et. al, Nayak *et. al.* and Lu *et. al.* [298, 301, 303]. Our calculations produce a doubly-bridged stable dimer structure for Si_2O_4. It has D_{2h} symmetry. Two of the four oxygens in this $(SiO_2)_2$ cluster form a symmetric double bridge between the silicons, while the other two are external to that rhombus. The most stable structures for Si_2O_4 are in agreement with those suggested by Wang *et al.* [310]. The lowest-energy structure for Si_3O_6 is predicted to be D_{2d} symmetry where four O atoms belong to double bridges and two end O atoms bonded to Si atoms. This is in agreement with the earlier studies [298, 301, 288, 43]. The ground-state geometry for Si_4O_8 is predicted to be a C_{2v} symmetry. This structure is predicted to be a low-energy isomer by Harkless *et al.* in their study [298]. Two other isomers with D_{4h} and D_{2h} symmetry are predicted to be 0.58 eV and 0.60 eV higher in energy than the lowest-energy isomer.

$(\mathbf{K_2O})_\mathbf{n}$ clusters. K_4O_2 is a triangular bipyramid with one capping K-atom. In all the structures obtained as GM for different cluster sizes, K - atoms tend to attach around central oxygen atom. The obtained structures are three dimensional with the exception of K_2O which is a bent molecule with a bond angle of 157.96° and a K-K bond length of 4.68 Å. For K_4O_2, the calculated K-O bond lengths with the number of bonds shown in parenthesis are 2.56 Å (3), 2.59 Å (3) and the K-K bond lengths are 4.16 Å (3), 4.22 Å (1), 4.24 Å (2). For K_6O_3 , the K-K bond lengths lie between 3.56 Å and 4.38 Å . The K-O bond lengths vary between 2.50 Å and 2.63 Å . For

K_8O_4, the K-K bond length variation is between 3.41 Å and 4.54 Å , whereas for K-O the bond length values vary between 2.47 Å and 2.76 Å .

$(\mathbf{CaO})_\mathbf{n}$ clusters. Ca_2O_2 is a rhombus shaped with Ca-O bond length of 2.25 Å and Ca-Ca bond length of 3.24 Å: the nearest neighbor distance in Ca metal is 3.95 A. The experimental bond length for Ca-O is 1.818 Å [324]. Ca_3O_3 is a bent ladder structure with Ca-O bond length of 2.25 Å. For Ca_4O_4 a cube structure or a slab structure is preferred to be the GM. The Ca-O bond length is 2.31 Å. The lowest-energy isomer for Ca_5O_5 can be seen as the addition of Ca-O to one edge of the Ca_4O_4 cubic cluster. The GM for Ca_6O_6 is a $2 \times 2 \times 3$ cubic structure. Hexagonal prism structure is also observed as an isomer for this cluster, 0.14 eV higher in energy than the lowest one. The Ca-O bond length is 2.31 Å whereas for oxygen atoms in the middle of the cube, this bond length is 2.5 Å. The predicted global minima for Ca_nO_n clusters are in agreement with those reported in literature [320, 329].

$(\mathbf{CuO})_\mathbf{n}$ clusters. The structure of the lowest-energy Cu_2O_2 cluster is a rhombus. This is in agreement with the study by Wang *et al.* [331] but disagrees with Dai *et al.* [332]. Wang *et al.* studied Cu_2O_n clusters based on density functional calculations and experimental measurements. Wang *et al.* suggest the structure for Cu_2O_2 is a rhombus. Dai *et al.* studied Cu_2O_x, $(x = 1 - 4)$ clusters using B3LYP functional and LANL2DZ basis set and suggested that the structure for Cu_2O_2 is linear or near linear. Bae*et al.* [308] did a DFT study of Cu_nO_n clusters using different functionals and basis set. They suggested a rhombic structure for the Cu_2O_2 cluster. Our calculations find Cu_3O_3 structures to be planar. The lowest-energy isomer for Cu_3O_3 is a ring structure with alternating Cu and O atoms. This result is in agreement

with studies by Bae *et al.* [308] and Xu *et al.* [330]. The Cu_4O_4 cluster is the first nonplanar structure found for Cu_nO_n and consists of a copper atom above the plane and an oxygen atom below the plane of a Cu_3O_3 ring. There is also an O-O bond in this structure. The lowest-energy isomer for Cu_5O_5 consists of a 6-membered Cu_3O_3 ring and a 7-membered Cu_3O_4 ring fused together sharing a O-Cu-O edge. Bae *et al.* [308] also found a similar structure for Cu_5O_5. The Cu_6O_6 structure consists of Cu_3O_2 and a Cu_2O_2 ring fused together sharing an O-Cu-O edge. There is also an O-O bond in this structure.

$(\mathbf{Cu_2O})_\mathbf{n}$ clusters. The lowest energy isomer for Cu_2O is triangular, with the oxygen atom bridged to a Cu_2 dimer. The Cu-O bond length is 1.82Å. This structure is in agreement with earlier studies [332, 333]. Cu_4O_2 consists of two Cu_2O triangular units sharing a Cu-atom and one Cu atom above the plane of the Cu_3O_2 unit. The Cu-O bond lengths are 1.83Å, 1.95Åand 1.99Å. The Cu_6O_3 unit has a Cu_4O_4 rhombus and two Cu atoms capping this rhombus; one above and one below the plane. The oxygen atoms are attached to the sides of these Cu-atoms. Cu_8O_4 is a 3D cage structure with connected Cu_2O units.

$(\mathbf{ZnO})_\mathbf{n}$ clusters. For $n = 1$, there is only one structure, a linear stick with bond length 1.76 Å. For $n = 2$, the GM is a rhombus with a bond length of 1.95 Å. Unlike reported in the literature [334], our algorithm did not find any linear structure as the lowest-energy isomer for Zn_2O_2. For $n = 3$, the predicted GM is in agreement with other studies [335, 336, 337, 338]. The Zn-O bond length is 1.89 Å. For $n = 4$ we found three isomers within 1.0 eV. The predicted GM agrees with other studies and the Zn-O bond length is 1.86 Å. The Zn-O bond length in the cuboid isomer

stretches to 2.0 Å. This bond length in Zn_5O_5 is 1.84 Å and in Zn_6O_6 it is 1.96 Å and 2.09Å respectively.

The global minima for Zn_nO_n clusters are rings up to $n = 5$. This result is in agreement with previous studies [335, 336, 337, 338] that predict the global minima for $(ZnO)_n$ clusters to be ring structure upto n=6. However, in our case for Zn_6O_6, hexagonal prism with alternating arrangement of Zn and O atoms, is predicted to be 2.2 eV more stable than the ring structure. This observation agrees with the study by Sunaidi *et al.* [334].

$(\mathbf{Ag_2O})_\mathbf{n}$ clusters. The lowest-energy isomer for Ag_2O is a triangle with an Ag-O bond length of 2.06Å, which is in good agreement with the experimental bond length of 2.0 Å [324]. This is in agreement with findings by Trushin and coworkers [339]. The lowest-energy isomer for Ag_4O_2 is a Ag_2O_2 rhombus with two Ag atoms above the plane attached to two oxygen atoms. The Ag-O bond length in the planar rhombus is 2.31 Å and between non-planar Ag and O this value is 2.09 Å . Also the Ag-Ag bond length is 2.90 Å which is close to the experimental value of 2.69 Å. The Ag-O bond length in Ag_6O_3 stretches to 2.20 Å and 2.30 Å . Klacar *et al.* [340] predicted the hexagonal prism structure for Ag_6O_3 with O atoms arranged in three-fold positions. Our calculations predict this structure to be 0.02 eV higher in energy than the lowest-energy isomer. Ag_8O_4 is a tetragonal bipyramid structure with two O atoms capping on two sides and O-Ag unit capping the other two sides. The Ag-O bond lengths range from 2.10Å for the outer Ag-O unit to 2.20 Å and 2.30 Å for interior Ag-O bonds.

The bond lengths for all the clusters are summarized in table 9.1.

Cluster	Bond lengths (Å)
(Li_2O)	1.65 (2)
$(Li_2O)_2$	1.82 (4), 1.66 (2)
$(Li_2O)_3$	1.71, 1.76 (2), 1.86, 1.87, 1.92 (4)
$(Li_2O)_4$	1.68 (2), 1.78 (4),1.82 (2),1.86 (4)
(MgO)	1.80
$(MgO)_2$	1.91 (4)
$(MgO)_3$	1.85 (6)
$(MgO)_4$	1.98 (12)
$(MgO)_5$	1.85 (2), 1.86 (2), 1.87 (4), 1.91 (1), 1.92 (1), 2.05 (1), 2.20, 2.21
$(MgO)_6$	1.92 (12), 2.02 (6)
Al_2O_3	1.67 (2), 1.71 (2)
Al_4O_6	1.79 (12)
Al_6O_9	1.74, 1.76 (4), 1.77 (2), 1.78, 1.79 (3), 1.81 (2), 1.82, 1.83, 1.84, 1.88, 1.95, 2.02
SiO_2	1.59 (2)
Si_2O_4	1.58 (2), 1.77 (4)
Si_3O_6	1.58 (2), 1.75 (4), 1.77 (4)
Si_4O_8	1.58 (3), 1.68 (2), 1.69 (4), 1.75 (2), 1.77 (2)

Cluster	Bond lengths (Å)
(K_2O)	2.38 (2)
$(K_2O)_2$	2.51, 2.56 (3), 2.59 (3)
$(K_2O)_3$	2.50, 2.53 (2), 2.55, 2.57 (2), 2.60,
	2.61, 2.62, 2.63, 2.70
$(K_2O)_4$	2.47, 2.51, 2.52, 2.55, 2.56,
	2.60 2.61 (2), 2.63, 2.64, 2.69, 2.70, 2.71, 2.73, 2.75, 2.76
(CaO)	2.13
$(CaO)_2$	2.25 (4)
$(CaO)_3$	2.21 (2), 2.22 (2), 2.27 (2), 2.46
$(CaO)_4$	2.32 (12)
$(CaO)_5$	2.20, 2.23, 2.27, 2.30,
	2.31 (6), 2.32 (2), 2.33 (2)
$(CaO)_6$	2.30, 2.31 (11), 2.32 (4), 2.49, 2.50 (3)
(CuO)	1.59
$(CuO)_2$	1.87 (4)
$(CuO)_3$	1.83 (2),1.84,1.85 (2), 1.87
$(CuO)_4$	1.81 (2),1.84,1.87 (2), 1.88, 1.89
$(CuO)_5$	1.83, 1.84, 1.87, 1.88 (2),
	1.89, 1.90 (2), 1.95, 1.97
$(CuO)_6$	1.80,1.82, 1.83, 1.88 (2), 1.87,
	1.89, 1.91 (4), 1.97, 2.10

Cluster	Bond lengths (Å)
(Cu_2O)	1.82 (2)
$(Cu_2O)_2$	1.83 (3), 1.95, 1.99
$(Cu_2O)_3$	1.92 (3),1.93, 1.96 (2), 1.97 (2), 2.01
$(Cu_2O)_4$	1.90 (3),1.91, 1.93, 1.95 (3), 1.97 (2), 1.98, 2.03
(ZnO)	1.78
$(ZnO)_2$	1.95 (4)
$(ZnO)_3$	1.89 (6)
$(ZnO)_4$	1.86 (8)
$(ZnO)_5$	1.84 (10)
$(ZnO)_6$	1.97 (12), 2.10 (6)
(Ag_2O)	2.06 (2)
$(Ag_2O)_2$	2.10 (2), 2.32 (4)
$(Ag_2O)_3$	2.13 (2), 2.16 (2), 2.23 (3), 2.30 (2)
$(Ag_2O)_4$	2.08, 2.13, 2.15, 2.16, 2.19 (2), 2.24 (3), 2.25, 2.26, 2.27, 2.28, 2.29

Table 9.1: Bond lengths

Cluster	Atomization energy (eV)	Dissociation energy (eV)	HOMO-LUMO gap (eV)
(Li_2O)	10.19		1.91
$(Li_2O)_2$	23.16	2.78	1.70
$(Li_2O)_3$	35.99	2.64	0.26
$(Li_2O)_4$	49.92	3.74	0.76
(MgO)	5.51		0.41
$(MgO)_2$	16.22	5.19	0.80
$(MgO)_3$	28.07	6.34	2.34
$(MgO)_4$	39.77	6.19	1.90
$(MgO)_5$	49.72	4.44	1.57
$(MgO)_6$	63.94	8.71	2.57
Al_2O_3	17.59		0.06
Al_4O_6	43.29	8.10	1.90
Al_6O_9	67.52	9.23	1.29
SiO_2	10.75		3.35
Si_2O_4	24.57	3.06	3.46
Si_3O_6	38.67	3.35	3.69
Si_4O_8	55.57	3.91	3.42
(K_2O)	6.91		0.39
$(K_2O)_2$	15.96	2.16	0.57
$(K_2O)_3$	25.15	2.27	0.33
$(K_2O)_4$	34.45	2.39	0.28

Cluster	Atomization energy (eV)	Dissociation energy (eV)	HOMO-LUMO gap (eV)
(CaO)	5.05		0.13
$(CaO)_2$	14.62	4.52	0.11
$(CaO)_3$	24.91	5.24	0.52
$(CaO)_4$	36.56	6.60	0.80
$(CaO)_5$	44.94	4.59	0.37
$(CaO)_6$	58.65	7.40	0.87
(CuO)	6.02		0.39
$(CuO)_2$	15.33	3.28	0.23
$(CuO)_3$	25.16	3.81	0.37
$(CuO)_4$	33.61	2.43	0.15
$(CuO)_5$	44.48	4.84	0.63
$(CuO)_6$	53.68	3.18	0.14
(Cu_2O)	9.11		1.16
$(Cu_2O)_2$	20.66	2.44	0.44
$(Cu_2O)_3$	34.06	4.30	0.07
$(Cu_2O)_4$	47.41	4.23	0.19
(ZnO)	4.57		0.51
$(ZnO)_2$	13.38	4.23	0.92
$(ZnO)_3$	23.25	5.30	2.14
$(ZnO)_4$	32.26	4.62	2.26
$(ZnO)_5$	38.47	4.25	2.43
$(ZnO)_6$	52.10	6.26	1.91

Cluster	Atomization energy (eV)	Dissociation energy (eV)	HOMO-LUMO gap (eV)
(Ag_2O)	7.13		1.06
$(Ag_2O)_2$	16.22	1.96	0.20
$(Ag_2O)_3$	26.44	3.09	0.32
$(Ag_2O)_4$	36.93	3.36	0.49

Table 9.2: Atomization energy (eV), Dissociation energy (eV) and HOMO-LUMO gap (eV) for metal oxide clusters

9.5 Energy Trends

To characterize the relative stability of the clusters, we considered energy parameters. We calculated the removal energy of a structural unit from the entire cluster, i.e. "dissociation energy" ΔE. Dissociation energy of the structures under consideration characterizes their stability to separation of a whole M_xO_y unit from $(M_xO_y)_n$ cluster.

$$\Delta\ (E) = E\ (M_xO_y)\ _{(n-1)} + E\ (M_xO_y) - E\ (\ (M_xO_y)_n) \tag{9.1}$$

The calculated values of dissociation energies for $(MO)_n$ and $(M_2O)_n$ clusters as a function of size n are given in figure 9.11.

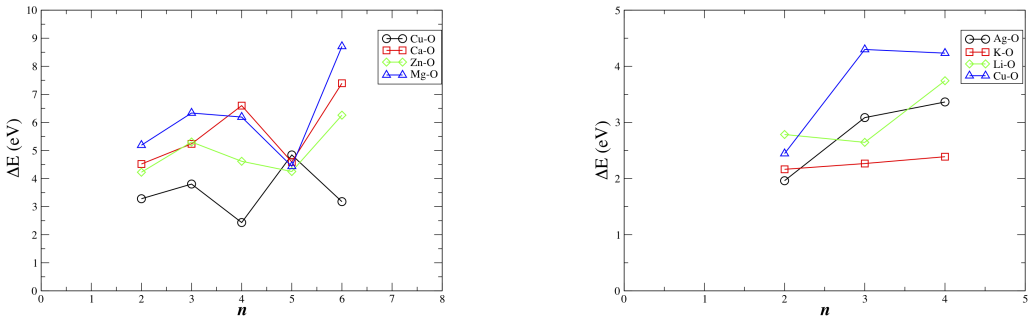

Fig. 9.11. Dissociation energy as a function of n for (a) $(MO)_n$ clusters (b) $(M_2O)_n$ clusters

Table 9.2 summarizes the atomization energies, dissociation energies and HOMO-LUMO gap values for all the clusters. The calculated values of dissociation ΔE for $(ZnO)_n$ clusters show a maximum at $n = 3$ and 6, demonstrating particular stability for $(ZnO)_3$ and $(ZnO)_6$. For $(CaO)_n$ clusters, this stability is indicated for cluster size $n = 4, 6$. For $(MgO)_n$ clusters, the maximum is at cluster size $n = 6$. Except for Cu, the dissociation energy curves have a minimum at $n = 5$. This shows that two $(MO)_5$ are unstable relative to $(MO)_4 + (MO)_6$. This can be understood by the high symmetry and perfect M/O ordering in the cube (n= 4) and the hexagonal prism (n= 6) which makes them energetically favorable.

To analyze the trends in geometry better, we calculated the asphericity (ζ) and shape descriptors (η) derived from the moment of inertia.

The asphericity (ζ) quantifies the deviation from spherical behaviour and (η) deviates from zero when a cluster shape deviates from quasi-spherical and has either a prolate shape $(I_c < I_b, I_b \sim I_a)$ or oblate shape $(I_c \sim I_b, I_b < I_a)$. The calculated values for (ζ) and (η) for all the clusters are summarized in the table 9.3.

Cluster	ζ	η
(Li_2O)	1.00	1.00
$(Li_2O)_2$	0.83	0.74
$(Li_2O)_3$	0.30	0.07
$(Li_2O)_4$	0.14	0.27
(MgO)	1.00	1.00
$(MgO)_2$	0.35	-0.28
$(MgO)_3$	0.33	-0.50
$(MgO)_4$	0.00	0.00
$(MgO)_5$	0.74	0.61
$(MgO)_6$	0.05	-0.22
Al_2O_3	1.00	1.00
Al_4O_6	0.00	0.00
Al_6O_9	0.06	-0.22
SiO_2	1.00	1.00
Si_2O_4	0.74	0.61
Si_3O_6	0.80	0.90
Si_4O_8	0.47	0.24
(K_2O)	0.98	0.96
$(K_2O)_2$	0.01	0.08
$(K_2O)_3$	0.38	0.38
$(K_2O)_4$	0.22	-0.04

Cluster	ζ	η
(CaO)	1.00	1.00
$(CaO)_2$	0.33	-0.45
$(CaO)_3$	0.49	0.14
$(CaO)_4$	0.00	0.00
$(CaO)_5$	0.27	-0.39
$(CaO)_6$	0.16	0.43
(CuO)	1.00	1.00
$(CuO)_2$	0.35	-0.31
$(CuO)_3$	0.33	-0.38
$(CuO)_4$	0.37	0.02
$(CuO)_5$	0.26	0.12
$(CuO)_6$	0.04	-0.12
(Cu_2O)	0.55	0.27
$(Cu_2O)_2$	0.48	0.42
$(Cu_2O)_3$	0.06	-0.12
$(Cu_2O)_4$	0.03	-0.08

Cluster	ζ	η
(ZnO)	1.00	1.00
$(ZnO)_2$	0.37	-0.21
$(ZnO)_3$	0.33	-0.500
$(ZnO)_4$	0.33	-0.500
$(ZnO)_5$	0.33	-0.499
$(ZnO)_6$	0.04	-0.215
(Ag_2O)	0.60	0.37
$(Ag_2O)_2$	0.11	0.12
$(Ag_2O)_3$	0.13	0.10
$(Ag_2O)_4$	0.13	0.22

Table 9.3: Asphericity (ζ) and shape descriptors (η) for metal oxides

The $(ZnO)_n$ clusters prefer planar ring structures. The most stable structures for $(Li_2O)_n$, $(Ag_2O)_n$, $(K_2O)_n$ and $(Cu_2O)_n$ are three-dimensional. The asphericity is 0.00 in 4 cases by symmetry, but otherwise asphericity is generally big compared to metal clusters. $(SiO_2)_n$ clusters favour prolate geometries, $(ZnO)_n$ favour oblate geometries (quasi planar rings, or stack of rings at $n = 6$). There is no obvious pattern in "shape" for the other clusters.

9.6 Conclusion

We have calculated the equilibrium geometries, energetics and electronic structure of $(Li_2O)_n$, $(K_2O)_n$, $(MgO)_n$, $(CaO)_n$, $(Cu_2O)_n$, $(CuO)_n$, $(Ag_2O)_n$, $(ZnO)_n$, $(Al_2O_3)_n$ and $(SiO_2)_n$ clusters with valence ranging from 1 to 4. The transition from

planar to non-planar structures occurs at $n = 4$ for $(MgO)_n$, $(CaO)_n$ and $(CuO)_n$, whereas for $(ZnO)_n$, this transition occurs at $n = 5$. $(Ag_2O)_n$, $(Li_2O)_n$, $(K_2O)_n$, $(Cu_2O)_n$, form three dimensional structures (except at $n = 1$). For $(SiO_2)_n$ and $(Al_2O_3)_n$, the most stable structures are planar up to $n = 2$ and $n = 1$ respectively, after which the most stable structures are non-planar. There are similarities in the shape pattern of $(M_xO_y)_n$ clusters with same x/y ratio, for example, stacked ring or cube like structures for $(MO)_n$ clusters $(M = Mg, Cu, Ca$ and $Zn)$. However, there are no simple growth patterns with increasing cluster size n. The HOMO-LUMO gap varies non-monotonically with size for $(MO)_n$ clusters. For $(M_2O)_n$ $(M = K, Ag, Cu)$ clusters, HOMO-LUMO gap decreases with increase in cluster size n. Overall, the calculated asphericity values for $(M_xO_y)_n$ clusters are bigger as compared to metal clusters. Minimizing surface area is relatively less important in metal oxides than in metal clusters, alternating M-O is more important and leads to non-spherical geometries.

Chapter 10

Conclusion

We obtained low energy geometries for a variety of metal and metal oxide clusters by DFT and TSDS optimization. In global optimization (GO), one can never be sure to have found the true global minimum. Accordingly, we interpret results for specific cluster species with caution and choose to emphasize, instead, trends within series of clusters. We note also that early tests of the TSDS method, and comparisons of results obtained by us to the literature, show that the TSDS-DFT methodology is among the best for cluster geometry optimization and often succeeds at finding the global minimum.

In general, the energetically favored cluster compositions and structures we found by TSDS-DFT are in qualitative agreement with well-known simple models. For instance: (1) silver clusters and Li-Mg-Al cluster alloys show, *on average*, enhanced stability when the valence electron count is $n = 8$ or $n = 20$, in line with the jellium model. And (2) the shapes of these clusters are, *on average*, nearly spherical at $n = 8$ and $n = 20$, oblate when n is slightly below 8 or 20, and prolate when n is slightly above 8 or 20. Other simple rules that are generally observed in our TSDS-DFT

results are as follows. (3) Metal cluster geometries tend to be compact, they tend to minimize surface area. (4) In cluster alloys, the element with the lowest surface energy tends to segregate to the surface. (5) Metals with with closed p- and d-type shells (Li, Ag, etc.) favor compact structures characterized by the presence of triangles, whereas Al-rich clusters often contain squares. (6) The favored structures of metal oxide clusters have few or no O-O neighbor pairs and few metal-metal pairs. (7) The favored chemical compositions of Al_xO_y and Si_xO_y have x/y equal to, or near, the bulk ratio of 2/3 and 1/2, respectively.

However, TSDS-DFT shows many exceptions to these rules, including low-lying isomers with sometimes qualitatively different geometries. And, to our knowledge, the above structural rules have very limited value for predicting the structure or composition of stable clusters. Thus, the results of TSDS-DFT global optimization reported in this thesis are far from trivial. The cluster specific predictions we make about geometries and energies should be of interest to experimentalists studying these clusters and could help interpret spectra.

Simple models and structural rules do help make sense of TSDS-DFT results. In particular, we showed the relative importance of different physical effects for stability of Li-Mg-Al clusters, and quantified these effects. The factors affecting the binding energies of Li-Mg-Al clusters and their magnitude (in eV) are: the cohesive energy of the three elements (-13.66); the surface area and associated surface energy of a cluster (+5.92); deviations from the ideal valence electron count of 8 or 20 (+0.39); difference in electronegativities of the constituting atoms of a cluster, and the associated ionic bonding (-0.25); Jahn-Teller distortions that stabilize clusters with open electronic

shells (-0.08); and the presence of spin-unpaired electrons (+0.03). The relative magnitude of these effects brings more precision to our understanding of metal clusters. They could help researchers make better educated guesses about the structure and stability of Li-Mg-Al, and other, metal alloy clusters.

An important finding in our study of aluminum oxide clusters is that the most stable clusters do not necessarily have the stoichiometric ratio $x/y = 2/3$ of the bulk oxide. This changes our understanding of the initial growth of very small alumina clusters and points to the possible role of these "non stoichiometric" species in small cluster experiments and, maybe, in alumina supported catalysts. At the very least, this result should caution researchers about the possible presence of cluster species with x/y different from 2/3 in their experiments. On the other hand, the $x/y = 1/2$ stoichiometry is clearly favored in Si_xO_y clusters.

The main conclusions of our study of the other metal oxides clusters M_xO_y (M=Li,Mg,K,Ca,Cu,Zn,Ag) are that: (i) O-O neighbor pairs are disfavored, (ii) there are resemblances between cluster geometries of elements in the same group (Li and K, Cu and Ag, Mg and Ca), as expected, however (iii) the size of the metal atom can make significant changes to structure (compare for instance Ca_6O_6 and Mg_6O_6, or Li_8O_4 and K_8O_4). Here again, simple rules have very limited predictive value, the TSDS-DFT results can be rationalized by these rules, but could not be obtained without solving the global optimization problem.

Future work

Future work should consider deeper analysis of algorithms and methods to calculate molecular structure and energetics, new proposals to try different methods, or address certain concerns. In future, more research is needed to apply the energy decomposition method used for Li-Mg-Al clusters in this research to a few other cases to see how the magnitude of the different effects change with elements and cluster size. Aside from a trivial dependence on the number of atoms of each element, the most important factor for Li-Mg-Al cluster structure and energy is the surface area (surface energy). We should develop and test empirical models where the only energy term (or the leading term) is an estimated surface energy based on some simple working definition of surface area. We could then use such a model, which is computationally very efficient, to study very large bimetallic clusters.

TSDS does not work as well for metal oxides as it does for metal clusters. Future work on a better global optimization method is needed, especially with a view to bigger metal oxide clusters.

It will be important that future research develop an empirical potential that reproduces, roughly, the TSDS-DFT optimized geometries of Al_xO_y. Such an empirical potential gives energy estimates millions of times faster than DFT. Therefore, doing global optimization with the empirical potential will take only a few seconds or few minutes of computing time. The geometries generated in this way can then be used as input for simple local optimizations with DFT. The enormous speed-up would allow us to study much bigger clusters, in particular the series $Al_{2x}O_{3x}$, $Al_{2x}O_{3x-1}$,

and $Al_{2x}O_{3x+1}$ with $x = 1, 2, 3$ (as we already studied) and $x = 4$ to 10. This may constitute the object of future studies.

Bibliography

[1] J. A. Alonso, *Structure and properties of atomic nanoclusters*, Imperial College, London, (2005)

[2] M. B. Knickelbein, *Reactions of Transition metal clusters with small molecules*, Annu. Rev. Phys. Chem. **50**, 79-115, (1999). https://doi.org/10.1146/annurev.physchem.50.1.79

[3] Reddy, B. V.; Khanna,S. N.; Dunlap,B. I. Giant magnetic moment in 4d clusters. *Phys. Rev. Lett.* **1993**, *70,* 332310.1103/PhysRevLett.70.3323

[4] Cox, A. J.; Louderback, J. G.; Bloomfield, L. A. Experimental observation of magnetism in rhodium clusters. *Phys. Rev. Lett.* **1993**, *71*, 92310.1103/PhysRevLett.71.923

[5] A. L. Mackay, Acta Cryst. 15(1962) 916

[6] Pearson, R. G., The Principle of Maximum Hardness, *Acc. Chem. Res.*, **1993**,*26(5)*, 250-255, 10.1021/ar00029a004

[7] De Volder, M. F. L.; Tawfick, S. H.; Baughman, R. H.; Hart, A. J. Carbon Nanotubes: Present and Future Commercial Applications. *Science* **2013**, *339(6119)*, 535-53910, 1126/science.1222453

[8] Cui, L. F.; Huang, X.; Wang, L. M.; Li, J.; Wang, L. S. Endohedral Stannaspherenes $M@Sn_{12}^{-}$: A Rich Class of Stable Molecular Cage Clusters. *Angewandte Chemie International Edition*, **2007**, *46(5)*, 742-745, 10.1002/anie.200603226

[9] Satya, B.; Li, X.; Wang, L.; Zeng, X. C., Evidence of hollow golden cages, *Proceedings of the national academy of sciences of the United States of America*, **2006**, *103(22)*, 8326-8330, 10.1073/pnas.0600637103

[10] Fournier, R.; Hussain, S. A.,Bimetallic Cages, *J. Chem. Phys.*,**2013**,*138*, 054303, 10.1063/1.4789417

[11] Wang, C.; Li, S.; Han, Y.; Lu, Z., Assembly of $LiMnPO_4$ Nanoplates into Microclusters as a High-Performance Cathode in Lithium-Ion Batteries, *ACS applied materials & interfaces*, **2017**, *9(33)*, 27618-2762, 410.1021/acsami.7b05868

[12] Wu, H.; Yuan, C.; Luo, Z., Tungsten-copper clusters assembled on porous alumina for optical limiting applications, *Journal of materials Chem. C*, **2017**, *5(30)*, 7561-7566,10.1039/C7TC01990D

[13] Song, B.; Zhang, X.; He, P.; Zhao, G., Han, G., Design of cluster structure units with large surface areas for high-capacity hydrogen storage: In the case of $Si_{12}C_{12}H_{24}$, *International Journal of Hydrogen energy*, **2017**,*42(31)*, 20003-20015/10.1016/j.ijhydene.2017.06.124

[14] Khanna, S. N.; Jena, P., *Atomic clusters: Building blocks for a class of solids*, Phys. Rev. B, **1995**, 51(19), 13705-1371610.1103/PhysRevB.51.13705

[15] P. Pyykkö, N. Runeberg, *Icosahedral WAu_{12}: A Predicted Closed-Shell Species, Stabilized by Aurophilic Attraction and Relativity and in Accord with the 18-Electron Rule* Angew. Chemie Int. Ed. 2002, 41, 2174

[16] Khanna, S. N.; Jena, P., *Assembling Crystals from Clusters*, Phys. Rev. Lett. 1992, 69, 1664-1667.

[17] Lievens, P.; Thoen, P.; Bouchaert, S.; Bouwen, W.; Vanhoutte, F.; Weidele, H.; Silverans, R. E.; Navarro-Vazquez, A.; von R. Schleyer, P. *Ionization potentials of $Li_nO(2 \leq n \leq 70)$ Clusters: Experiment and Theory*, J. Chem. Phys. 1999, 110, 10316-10329.

[18] Beck, S. M,, *Mixed metal-silicon clusters formed by chemical reaction in a supersonic molecular beam: Implications for reactions at the metal silicon interface* J. Chem. Phys. 1987, 87, 4233; 1989, 90, 6306-6312.

[19] Koyasu, K.; Akutsu, M.; Mitsui, M.; Nakajima, A. *Selective formation of $MSi_{16}(M = Sc, Ti, andV)$*, J. Am. Chem. Soc. 2005, 127, 4998-4999

[20] Koyasu, K.; Atobe, J.; Akutsu, M.; Mitsui, M.; and Nakajima, A., *Electronic and Geometric Stabilities of Clusters with Transition Metal Encapsulated by Silicon*, J. Phys. Chem. A 2007, 111, 42-49

[21] Torres, M. B.; Fernandez, E. M.; Balba's, L. C. *Theoretical Study of Isoelectronic* Si_nM *Clusters* ($M = Sc^-, Ti, V^+; n = 14 - 18$), Phys. Rev. B: Condens. Matter Mater. Phys. 2007, 75, 205425.

[22] Tsunoyama, H; Shibuta, M.; Nakaya, M.; Eguchi, T.; and Nakajima, A. *Synthesis and Characterization of Metal-Encapsulating* Si_{16} *Cage Superatoms*, Acc. Chem. Res., 2018, 51, 1735-1745. 10.1021/acs.accounts.8b00085

[23] Knight, W. D.; Clemenger, K.; Heer, W. A.; Saunders, W. A.; Chou, M. Y.; Cohen, M. L., Electronic Shell Structure and Abundances of Sodium Clusters, *Phys. Rev. Lett.*, **1984**, *52*, 2141, 10.1103/PhysRevLett.52. 2141

[24] Bonacic-Koutecky V., Fantucci P., Koutecky J., *Quantum chemistry of small clusters of elements of groups Ia, Ib, and IIa: fundamental concepts, predictions, and interpretation of experiments* Chem. Rev. 1991; **91**(5), 1035-1108 10.1021/cr00005a016

[25] Miller, T. A. *Chemistry and chemical intermediates in supersonic free jet expansions*, Science, 1984, 223(4636), 545-53, 10.1126/science.223.4636.545

[26] Murphy, H. R.; Miller, D. R., *Effects of nozzle geometry on kinetics in free-jet expansions*, J. Phys. Chem. 1984, 88(20), 4474-4478, 10.1021/j150664a005

[27] Smalley, R. E.; Wharton, L.; Levy, D. H. *Molecular optical spectroscopy with supersonic beams and jets*, Acc. Chem. Res. 1977, 10(4), 139-145, 10.1021/ar50112a006

[28] Sylla, F.; Veltcheva, M.; Kahaly, S.; Flacco, A.; Malka, V., *Development and characterization of very dense submillimetric gas jets for laser-plasma interaction*, Rev. Sci. Instrum. 2012, 83, 033507, 10.1063/1.3697859

[29] C. Ratsch, A. Fielicke, A. Kiriyuk, J. Behler, G. von Helden, G. Meijer and M. Scheffer, J. Chem. Phys. **122**, 124302(2005) A. Fielicke, G. Meijer, D. B Pedersen, B. Simard and D. M. Rayner, J. Phys. Chem. B. **108**, 14591(2004)

[30] Truong, N. X.; Jaeger, B. K. A.; Gewinner, S.; Schollkopf, W.; Fielicke, A.; Dopfer, O. *Infrared spectroscopy and structures of borondoped silicon clusters* ($Si_nB_m, n = 3-8, m = 1-2$), J. Phys. Chem. C, (2017), **121(17)**, 9560-9571, 10.1021/acs.jpcc.7b01290

[31] Lapoutre, V. J. F.; Haertelt, M.; Meijer, G.; Fielicke, A.; Bakker,J. M. Communication: *IR spectroscopy of neutral transition metal clusters through thermionic emission*, J. Chem. Phys. 2013, 139, 121101. 10.1063/1.4822324

[32] Bowlan, J.; Harding, D. J.; Jalink, J.; Kirilyuk, A.; Meijer, G.; Fielicke, A. Communication: *Structure of magnetic lanthanide clusters from far-IR spectroscopy:* $Tb_n^+(n = 5-9)$, J. Chem. Phys. 2013, 138, 031102. 10.1063/1.4776768

[33] Yacovitch, T. I.; Wende, T.; Jiang, L.; Heine, N.; Meijer, G.; Neumark, D. M.; Asmis, K. R., *Infrared spectroscopy of hydrated bisulfate anion clusters:* $HSO_4(H_2O)_{1-16}$. J. Phys. Chem. Lett. 2011, 2(17), 2135-2140. 10.1021/jz200917f

[34] Bakker, J. M.; Lapoutre, V. J. F.; Redlich, B.; Oomens, J.; Sartakov, B. G.; Fielicke, A.; von Helden, G.; Meijer, G.; van der Meer, A. F. G., *Intensity-*

resolved IR multiple photon ionization and fragmentation of C_{60}. J. Chem. Phys. 2010, **132**, 074305. 10.1063/1.3313926

[35] Fielicke, A.; Ratsch, C.; von Helden, G.; Meijer, G. *The far infrared spectra of neutral and cationic niobium clusters:* $Nb_5^{0/+}$ *to* $Nb_9^{0/+}$. J. Chem. Phys. (2007), **127**, 234306 10.1063/1.2806176

[36] Kirilyuk, A.; Fielicke, A.; Demyk, K.; von Helden, G.; Meijer,G.; Rasing, T., *Ferrimagnetic cagelike* Fe_4O_6 *cluster: Structure determination from infrared dissociation spectroscopy*, Phys. Rev. B: Condens. Matter Mater. Phys. (2010), **82(2)**, 020405 10.1103/PhysRevB.82.020405

[37] Weber, J. M.; Leber, E.; Ruf, M. -W.; Hotop, H. *Nuclear-Excited Feshbach Resonances in Electron Attachment to Molecular Clusters*, Phys. Rev. Lett., **82(3)**, 516, (1999), 10.1103/PhysRevLett.82.516

[38] Mitsui, M.; Nakajima, A.; Kaya, K., Even, U., *Mass spectra and photoelectron spectroscopy of negatively charged benzene clusters,* $(benzene)_n^-(n = 53 - 124)$ J. Chem. Phys., **115(13)**, 5707, (2001), 10.1063/1.1407844

[39] Lin, S. H.; Neusser, H. J.; Schlag, E. W. *Multiphoton Spectroscopy of Molecules: Quantum Electronics: Principles and Applications*; Academic Press: New York, (1984).

[40] Gilb, S.; Weis, P.; Furche, F.; Ahlrichs, R.; and Kappes, M. M., *Structures of small gold cluster cations* $(Au_n^-, n < 14)$*: Ion mobility measurements*

versus density functional calculations, J. Chem. Phys., **116**, 4094, (2002), 10.1063/1.1445121

[41] Schoos, D.; Blom, M. N.; Parks, J. H.; Issendorff, B. V.; Haberland, H.; and Kappes, M. M., *The Structures of Ag_{55}^{+} and Ag_{55}^{-}: Trapped Ion Electron Diffraction and Density Functional Theory*, Nano. Lett. 5, (2005), 1972-1977 10.1021/nl0513434

[42] Maier-Borst, M.; Cameron, D. B.; Rokni, M.; Parks, J. H., *Electron diffraction of trapped cluster ions*, Phys. Rev. A, 59(5), R3162-R3165, (1999) 10.1103/PhysRevA.59.R3162

[43] Wang, L. M.; Bai, J.; Lechtken, A.; Huang, W.; Schooss, D.; Kappes, M. M.; Zeng, X. C.; Wang, L. S., *Magnetic doping of the golden cage cluster $M@Au-16^{-}(M = Fe, Co, Ni)$* Phys. Rev. B, 79(3), 033413, 2009 10.1103/PhysRevB.79.033413

[44] Blom, M. N.; Schooss, D.; Stairs, J.; Kappes, M. M., *Experimental structure determination of silver cluster ions ($Ag_n^{+}, 19 \leq n \leq 79$)*, J. Chem. Phys. 124(24), 244308, (2006), 10.1063/1.2208610

[45] Knickelbein, M. B., *Experimental observation of superparamagnetism in manganese clusters*, Phys. Rev. Lett. 86(23), (2001), 5255-7, 10.1103/PhysRevLett.86.5255 .

[46] Bucher, J. P.; and Bloomfield, L. A.; *Magnetism of free transition-metal and rare earth clusters*, Int. Journal of Modern Physics B, 7(4), 1079-1114, 10.1142/S0217979293002249

[47] Stillinger, F. H. *Exponential multiplicity of inherent structures*, Phys. Rev. E: Stat. Phys., Plasmas, Fluids, Relat. Interdiscip. Top. (1999), 59, 48-51

[48] Cheng, J.; Fournier, R., Structural Optimization of Atomic Clusters by Tabu Search in Descriptor Space, Theor. Chem. Acc. 112 (2004) 7-15.

[49] Frisch, M. J.; Trucks, G. W.; Schlegel, H. B.; Scuseria, G. E.; Robb, M. A.; Cheeseman, J. R.; Scalmani, G.; Barone, V.; Mennucci, B.; Petersson, G. A.; Nakatsuji, H.; Caricato, M.; Li, X.; Hratchian, H. P.; Izmaylov, A. F.; Bloino, J.; Zheng, G.; Sonnenberg, J. L.; Hada, M.; Ehara, M.; Toyota, K.; Fukuda, R.; Hasegawa, J.; Ishida, M.; Nakajima, T.; Honda, Y.; Kitao, O.; Nakai, H.; Vreven, T.; Montgomery, J. A.; Peralta, J. E.; Ogliaro, F.; Bearpark, M.; Heyd, J. J.; Brothers, E.; Kudin, K. N.; Staroverov, V. N.; Kobayashi, R.; Normand, J.; Raghavachari, K.; Rendell, A.; Burant, J. C.; Iyengar, S. S.; Tomasi, J.; Cossi, M.; Rega, N.; Millam, J. M.; Klene, M.; Knox, J. E.; Cross, J. B.; Bakken, V.; Adamo, C.; Jaramillo, J.; Gomperts, R.; Stratmann, R. E.; Yazyev, O.; Austin, A. J.; Cammi, R.; Pomelli, C.; Ochterski, J. W.; Martin, R. L.; Morokuma, K.; Zakrzewski, V. G.; Voth, G. A.; Salvador, P.; Dannenberg, J. J.; Dapprich, S.; Daniels, A. D.; Farkas; Foresman, J. B.; Ortiz, J. V.; Cioslowski, J.; Fox, D. J. Gaussian 09, Revision B.01; Gaussian, Inc.: Wallingford, CT, 2009

[50] Gaussian 16, Revision B.01, Frisch, M. J.; Trucks, G. W.; Schlegel, H. B.; Scuseria, G. E.; Robb, M. A.; Cheeseman, J. R.; Scalmani, G.; Barone, V.; Petersson, G. A.; Nakatsuji, H.; Li, X.; Caricato, M.; Marenich, A. V.; Bloino, J.; Janesko, B. G.; Gomperts, R.; Mennucci, B.; Hratchian, H. P.; Ortiz, J. V.; Izmaylov, A. F.; Sonnenberg, J. L.; Williams-Young, D.; Ding, F.; Lipparini, F.; Egidi, F.; Goings, J.; Peng, B.; Petrone, A.; Henderson, T.; Ranasinghe, D.; Zakrzewski, V. G.; Gao, J.; Rega, N.; Zheng, G.; Liang, W.; Hada, M.; Ehara, M.; Toyota, K.; Fukuda, R.; Hasegawa, J.; Ishida, M.; Nakajima, T.; Honda, Y.; Kitao, O.; Nakai, H.; Vreven, T.; Throssell, K.; Montgomery, J. A., Jr.; Peralta, J. E.; Ogliaro, F.; Bearpark, M. J.; Heyd, J. J.; Brothers, E. N.; Kudin, K. N.; Staroverov, V. N.; Keith, T. A.; Kobayashi, R.; Normand, J.; Raghavachari, K.; Rendell, A. P.; Burant, J. C.; Iyengar, S. S.; Tomasi, J.; Cossi, M.; Millam, J. M.; Klene, M.; Adamo, C.; Cammi, R.; Ochterski, J. W.; Martin, R. L.; Morokuma, K.; Farkas, O.; Foresman, J. B.; Fox, D. J. Gaussian, Inc., Wallingford CT, 2016

[51] Robert Withnall, Babur Z. Chowdhry, Stephen Bell, Trevor J. Dines, *Computational Chemistry Using Modern Electronic Structure Methods* J. Chem. Educ., **2007**, 84 (8), 1364, 10.1021/ed084p1364

[52] R.G. Parr, W. Yang, *Density Functional Theory of Atoms and Molecules*, Oxford University Press, Oxford, 1989.

[53] Lecture notes: **Kohn-Shan Density Functional Theory** by Dr. R. Fournier, 2003

[54] Thesis: Structural and electronic principles for atomic clusters by Yan Sun, 2008, York University

[55] P. Hohenberg and W. Kohn, Phys. Rev. **136**, B864 (1964)

[56] Kutzelnigg, W.: J. Mol. Struct. Theochem 768, 163-173 (2006)

[57] W. Kohn and L.J. Sham, Phys. Rev. 140, A1133(1965)

[58] S.H.Vosko, L.Wilk and M.Nusair, *Accurate spin-dependent electron liquid correlation energies for local spin density calculations: a critical analysis*, Can. J. Phys. 58, 1200 (1980), 10.1139/p80-159

[59] Perdew, J. P., Burke, K., Ernzerhof, M., "Generalized Gradient Approximation Made Simple", Phys. Rev. Lett. **77**, 3865(1996), 10.1103/PhysRevLett.77.3865

[60] J. Tao, J. P. Perdew, V. N. Staroverov, and G. E. Scuseria , Meta-generalized gradient approximation: explanation of a realistic nonempirical density functional, J Chem Phys., 2004, 120(15), 6898-911, 10.1063/1.1665298

[61] A.D. Becke, *Density functional calculations of molecular bond energies*, J. Chem. Phys. **84** (1986) 4524 - 4529.

[62] Becke, A. D. A new mixing of Hartree-Fock and local density- functional theories, J. Chem. Phys. 1993, 98, 5648

[63] Kurth, S.; Perdew, J. P. ; Blaha, P. *Molecular and solid-state tests of density functional approximations: LSD, GGAs, and meta-GGAs* International Journal of Quantum Chem., 75(4-5), 889-909, (1999)

[64] Schimkaa, L.; Harl, J.; Kresse, G.; *Improved hybrid functional for solids: The HSEsol functional* J. Chem. Phys. 134, 024116 (2011),10.1063/1.3524336

[65] Staroverov, V. N.; Scuseria, G. E.; Tao, J.; Perdew, J. P., Phys. Rev. B 2004, 69, 075102

[66] Staroverov, V. N.; Scuseria, G. E.; Tao, J.; Perdew, J. P. Phys. Rev. B, 2008, 78, 239907

[67] Haas, P.; Tran, F.; Blaha, P., 2009 Phys. Rev. B, 2009, 79 085104

[68] Haas, P.; Tran, F.; Blaha, P., Phys. Rev. B 2009,79, 209902

[69] Csonka, G. I.; Perdew, J. P.; Ruzsinszky, A.; Philipsen, P. H. T.; Lebgue, S.; Paier, J.; Vydrov, O. A.; and ngyn, J. G., 2009 Phys. Rev. B 2009, 79, 155107

[70] Tran, F.; Laskowski, R.; Blaha, P.; Schwarz, K., Phys. Rev. B 2007, 75, 115131

[71] Sun, J.; Marsman, M.; Csonka, G. I.; Ruzsinszky, A.; Hao, P.; Kim, Y. S.; Kresse, G. and Perdew, J. P.; 2011 Phys. Rev. B, 2011, 84, 035117

[72] Wellendorff, J.; Lundgaard, K. T.; Jacobsen, K. W.; and Bligaard, T., J. Chem. Phys. 2014, 140, 144107

[73] Xiao, B.; Sun, J.; Ruzsinszky, A; Feng, J.; Haunschild, R.; Scuseria, G. E.; and Perdew, J. P.; 2013 Phys. Rev. B 2013 88, 184103

[74] Tran, F.; Stelzl, J.; and Blaha, P.; J. Chem. Phys. 2016, 144, 204120

[75] V. N. Staroverov, G. E. Scuseria, J. Tao, and J.P. Perdew, Comparative assessment of a new nonempirical density functional: Molecules and hydrogen-bonded complexes, J. Chem. Phys. 119 (2003) 12129-12137.

[76] W. D. Knight, K. Clemenger, W. A. DeHeer, W. A. Saunders, M. Y. Choy, and M. L. Cohen, Phys. Rev. Lett **52**, 2141(1984); W. A. DeHeer, Rev. Mod. Phys. **65**, 611(1993); M. Brack, Rev. Mod. Phys. **65**, 677(1993).

[77] M. Y. Chou, Andrew Cleland, and Marvin L. Cohen, *Total Energies, abundances, and electronic shell structure of Lithium, Sodium and Potassium clusters*, Solid State Communications, 52(7), 645-648, 1984.

[78] Jahn, H. A.; Teller, E., Stability of polyatomic molecules in degenerate electronic states - 1.-Orbital degeneracy Proc. R. Soc. London A, 1937, 161, 220-235 10.1098/rspa.1937.0142

[79] Dhillon, H.; Fournier, R. *Geometric structure of silver clusters with and without adsorbed Cl and Hg*, Computational and Theoretical Chemistry, 1021, (2013), 26-34, 10.1016/j.comptc.2013.06.007

[80] R. Fournier, *Theoretical study of the structure of silver clusters*, J. Chem. Phys., 115 (2001), 2165 - 2177.

[81] M.R. Hoare and P. Pal, Adv. Phys. 20 161 (1971); Nature (Physical Sciences) 230, 5 (1971) Nature (Physical Sciences) 236, 35 (1972)

[82] Echt, O.; Sattler, K.; Recknagel, E. *Magic numbers for sphere packings: Experimental verification in free xenon clusters*, Phys. Rev. Lett., (1981), 47(16), 1121-1124.

[83] J. P. K . Doye, *A model metal potential exhibiting polytetrahedral clusters* J. Chem. Phys. 111 1890(1999)

[84] O.P. Charkin, D.O. Charkin, N.M. Klimenko, A.M. Mebel, *A theoretical study of isomerism in doped aluminum* XAl_{12} *clusters* $(X = B, Al, Ga, C, Si, Ge)$ *with 40 valence electrons*. Chemical Physics Letters 365 (2002) 494 - 504

[85] D. Y Sun and X. G Gong, *Structural properties and glass transition in* Al_n *clusters*, Phys. Rev. B. 57, 4730,(1998), 10.1103/PhysRevB.57.4730

[86] Aguadoa A, and Jose M. Lopez, Structures and stabilities of Al_n^+, Al_n, and Al_n^-, $n = 13 - 34$ clusters. J. Chem. Phys, 130, 064704, (2009)

[87] B. K. Rao and P. Jena, *Evolution of the electronic structure and properties of neutral and charged aluminum clusters: A comprehensive analysis* J. Chem. Phys. 111, 1890(1999)

[88] Yan Sun, Min Zhang, and Rene Fournier, *Periodic trends in the geometric structures of 13-atom metal clusters*, Phys. Rev. B, 77, 075435, (2008), 10.1103/PhysRevB.77.075435

[89] R. G. Pearson, *Recent advances in the concept of hard and soft acids and bases*, J. Chem. Educ. 64(7), 561 (1987). 10.1021/ed064p561

[90] R. G. Parr and P. K. Chattaraj, *Principle of maximum hardness*, J. Am. Chem. Soc., 113(5), 1854-1855, (1991). 10.1021/ja00005a072

[91] J. L. Gázquez, *Chemical hardness: Structure and bonding (ed.) K D Sen (Berlin: Springer)* Struct. Bonding 80, 27 (1993).

[92] R. G. Parr and J. L. Gzquez, *Hardness functional*, J. Phys. Chem. 97(16), 3939-3940 (1993), 10.1021/j100118a003

[93] Manoj K. Harbola, *Magic numbers for metallic clusters and the principle of maximum hardness*

[94] Knickelbein, M. B.; Yang, S., *Isomers of niobium clusters: Direct spectroscopic evidence* J. Chem. Phys. 93, 1476, (1990) 10.1063/1.459159

[95] K. Athanassenas , D. Kreisle , B.A. Collings , D.M. Rayner, P.A. Hackett *Ionization potentials of niobium cluster oxides*, Chemical Physics Lett., 213, 1-2, 105-110, (1993) 10.1016/0009-2614(93)85426-O

[96] Koopmans, T., *Über die Zuordnung von Wellenfunktionen und Eigenwerten zu den einzelnen Elektronen eines Atoms*, Physica, 1, 104-113, 1934 10.1016/S0031-8914(34)90011-2

[97] J.P. Perdew, R.G. Parr, M. Levy, J. Balduz, *Density-Functional Theory for Fractional Particle Number: Derivative Discontinuities of the Energy*, Phys. Rev. Lett., 49, (1982), 1691. 10.1103/PhysRevLett.49.1691

[98] J.P. Perdew, M. Levy, *Physical Content of the Exact Kohn-Sham Orbital Energies: Band Gaps and Derivative Discontinuities*, Phys. Rev. Lett., 51, (1983), 1884. 10.1103/PhysRevLett.51.1884

[99] M. Levy, J.P. Perdew, V. Sahni, *Exact differential equation for the density and ionization energy of a many-particle system*, Phys. Rev. A, 30, (1984), 2745. 10.1103/PhysRevA.30.2745

[100] C.-O. Almbladh, A.C. Pedroza, *Density-functional exchange-correlation potentials and orbital eigenvalues for light atoms*, Phys. Rev. A, 29, (1984) 2322. 10.1103/PhysRevA.29.2322

[101] C.-O. Almbladh, U. von Barth, *Exact results for the charge and spin densities, exchange-correlation potentials, and density-functional eigenvalues* Phys. Rev. B, 31, (1985), 3231. 10.1103/PhysRevB.31.3231

[102] J.P. Perdew, M. Levy, *Comment on "Significance of the highest occupied Kohn-Sham eigenvalue"*, Phys. Rev. B 56 (1997) 16021, 10.1103/PhysRevB.56.16021

[103] M. E. Casida, *Correlated optimized effective-potential treatment of the derivative discontinuity and of the highest occupied Kohn-Sham eigenvalue: A Janak-type theorem for the optimized effective-potential model*, Phys. Rev. B 59, 4694, (1999), 10.1103/PhysRevB.59.4694

[104] Tsuneda, T.; Song, J.-W.; Suzuki, S.; Hirao, K., *On Koopmans-theorem in density functional theory*, J. Chem. Phys. 133, 174101, (2010), 10.1063/1.3491272

[105] Chong, D. P.; Gritsenko, O. V.; and Baerends E. J., *Interpretation of the Kohn-Sham orbital energies as approximate vertical ionization potentials*, J Chem. Phys., 116(5), 1760-1772, (2002), 10.1063/1.1430255

[106] Savin, A.; Umrigar, C. J.; Gonze, X., *Relationship of Kohn-Sham eigenvalues to excitation energies*, Chem. Phys. Lett., 288(2-4), (1998), 391-395, 10.1016/S0009-2614(98)00316-9

[107] Fournier, R *Trends in energies and geometric structures of neutral and charged aluminum clusters*, Journal of Chemical Theory and computation, 3, 921-929, (2007)

[108] Shvartsburg, A. A,; Jarrold, M. F.; Liu, B.; Lu, Z. Y.; Wang, C. Z.; Ho, K. M.; Phys. Rev. Lett. 81, (1998), 4616.

[109] Shvartsburg, A. A.; Liu, B; Jarrold, M. F.; Ho, K. M. (2000) J Chem. Phys., (2000), 112, 4517

[110] Chekmarev, S.; Phys. Rev. E. 64, 036703 (2001) Tsai, C.; and Jordan, K. ; J. Phys. Chem, 97, 11227 (1993)

[111] Fournier, R.; Mohareb, A., Optimizing molecular properties using a relative index of thermodynamic stability and global optimization techniques, *Journal of Chemical Physics*, **2016**, *144*, 02411410.1063/1.4939530

[112] Perdew, J. P.; Zunger, A.; Phys. Rev. B, 23, (1981), 5048.

[113] Rösch, N. in: P. Phariseau, L. Scheire (Eds.), Electrons in Finite and Infinite Structures, NATO Advanced Study Institute, Series B, vol. 24, Plenum Press, New York, 1977, p. 1.

[114] Rösch, N.; Trickey, S. B.; J. Chem. Phys.,106, (1997), 8940.

[115] Mardirossian, N; Gordon, M. H., Thirty years of density functional theory in computational chemistry: an overview and extensive assessment of 200 density functionals Molecular Physics (2017),115(19), 2315-2372, 10.1080/00268976.2017.1333644

[116] W. Harbich, S. Fedrigo, J. Buttet, The optical absorption spectra of small silver clusters ($n = 5 - 11$) embedded in argon matrices, Chem. Phys. Lett. 195 (1992) 613-617

[117] S. Fedrigo, W. Harbich, and J. Buttet, Collective dipole oscillations in small silver clusters embedded in rare-gas matrices, Phys. Rev. B 47 (1993) 10706–10715.

[118] T. Tabarin, R. Antoine, I. Compagnon, M. Broyer, P. Dugourd, R. Mitrić, J. Petersen and V. Bonačić-Koutecký, Optical absorption of isolated silver cluster-tryptophan: A joint experimental and theoretical study, Eur. Phys. J. D 43 (2007) 275-278.

[119] K. Baishya, J.C. Idrobo, S. Öğüt, M. Yang, K. Jackson, and J. Jellinek, Optical absorption spectra of intermediate-size silver clusters from first principles, Phys. Rev. B 78 (2008) 075439 (9 pages).

[120] M. Harb, F. Rabilloud, D. Simon, A. Rydlo, S. Lecoultre, F. Conus, V. Rodriguex, and C. Félix, Optical absorption of small silver clusters: Ag_n, (n = 4-22), J. Chem. Phys. 129 (2008) 194108 (9 pages).

[121] G.-T. Bae and C.M. Aikens, Time-Dependent Density Functional Theory Studies of Optical Properties of Ag Nanoparticles: Octahedra, Truncated Octahedra, and Icosahedra, J. Phys. Chem. C 116 (2012) 10356-10367.

[122] G.M. Koretsky and M. B. Knickelbein, The reactions of silver clusters with ethylene and ethylene oxide: Infrared and photoionization studies of $Ag_n(C_2H_4)_m$, $Ag_n(C_2H_4O)_m$ and their deuterated analogs, J. Chem. Phys. 107 (1997) 10555-10566.

[123] L.D. Socaciu, J. Hagen, J.L. Roux, D.M. Popolan, T.M. Bernhardt, L. Wöste, Strongly cluster size dependent reaction behavior of CO with O_2 on free silver cluster anions, J. Chem. Phys. 120 (2004) 2078-2081.

[124] A. Fielicke, P. Gruene, G. Meijer, and D.M. Rayner, The adsorption of CO on transition metal clusters: A case study of cluster surface chemistry, Surf. Sci. 603 (2009) 1427-1433.

[125] C.P. Collier, J.R. Heath, S.E. Henrichs, R.J. Saykally and J.J. Shiang, Reversible tuning of silver quantum dot monolayers through the metal-insulator transition, Science 277 (1997) 1978-1981.

[126] S.-H. Kim, G. Medeiros-Ribeiro, D.A.A. Ohlberg, R. Stanley Williams, J.R. Heath, Individual and collective electronic properties of Ag nanocrystals, J. Phys. Chem. B 103 (1999) pg. 10341-10347

[127] K. LaiHing, P.Y. Cheng, and M.A. Duncan, Laser photoionization and spectroscopy of gas phase silver clusters, Z. Phys. D 13 (1989) 161-169.

[128] V.A. Spasov, T.H. Lee, J.P. Maberry, and K.M. Ervin, Measurement of the dissociation energies of anionic silver clusters (Ag_n^-, n = 2-11) by collision-induced dissociation, J. Chem. Phys. 110 (1999) 5208-5217.

[129] T. Diederich, J. Tiggesbäumker, and K.-H. Meiwes-Broer, Spectroscopy on rare gas-doped silver clusters in helium droplets, J. Chem. Phys. 116 (2002) 3263-3269.

[130] A. Przystawik, P. Radcliffe, T. Diederich, T. Döppner, J. Tiggesbäumker, and Karl-Heinz Meiwes-Broer, Photoelectron studies of neutral Ag_3 in helium droplets, J. Chem. Phys. 126 (2007) 184306 (5 pages).

[131] T.M. Bernhardt, J. Hagen, S.M. Lang, D.M. Popolan, L.D. Socaciu-Siebert, and L. Wöste, Binding Energies of O_2 and CO to Small Gold, Silver, and Binary SilverGold Cluster Anions from Temperature Dependent Reaction Kinetics Measurements, J. Phys. Chem. A, 113 (2009) pp 27242733.

[132] Y.-N. Wu, M. Schmidt, J. Leygnier, H.-P. Cheng, A. Masson, and C. Bréchignac, Adsorption of small molecules on silver clusters, J. Chem. Phys. 136 (2012) 024314 (8 pages).

[133] K. Michaelian, N. Rendon, and I. L. Garzon, Structure and energetics of Ni, Ag, and Au nanoclusters, Phys. Rev. B 60 (1999) 2000-2010.

[134] R. Fournier, Theoretical study of the structure of silver clusters, J. Chem. Phys. 115 (2001) 2165-2177.

[135] E. M. Fernández, J. M. Soler, I. L. Garzón, and L. C. Balbás, Trends in the structure and bonding of noble metal clusters, Phys. Rev. B 70 (2004) 165403 (14 pages).

[136] M. Pereiro and D. Baldomir, Determination of the lowest-energy structure of Ag_8 from first-principles calculations, Phys. Rev. A 72 (2005) 045201 (4 pages)

[137] X. Shao, X. Liu, and W. Cai, Structural Optimization of Silver Clusters up to 80 Atoms with Gupta and Sutton-Chen Potentials, J. Chem. Theory Comput. 1 (2005) 762.

[138] M. Yang, K.A. Jackson, and J. Jellinek, First-principles study of intermediate size silver clusters: Shape evolution and its impact on cluster properties, J. Chem. Phys. 125 (2006) 144308 (8 pages).

[139] H. Grönbeck, A. Hellman, A. Gavrin, Structural, Energetic, and Vibrational Properties of NO_x Adsorption on Ag_n, n = 1-8, J. Phys. Chem. A 111 (2007) 6062-6067.

[140] H. Zhang and D. Tian, Structural evolution of Ag_n^v ($v = +/-1, 0; n$ =3-14) clusters using genetic algorithm and density functional theory method Computational Materials Science 42 (2008) 462-469.

[141] W. Zhang, S.-Y. Yan, Z.-X. Zhao, and H.-X. Zhang, Stabilities and fragmentation behaviors of Ag_n clusters (n =2–34), J. Theor. Comput. Chem. 11 (2012) 953-964.

[142] S. Chrétien, M.S. Gordon, and H. Metiu, Density functional study of the adsorption of propene on silver clusters, Ag_m^q ($m = 1$–5; $q = 0, +1$), J. Chem. Phys. 121 (2004) 9925 (6 pages) and references therein.

[143] S. Klacar, A. Hellman, I. Panas, and H. Grönbeck, Oxidation of Small Silver Clusters: A Density Functional Theory Study, J. Phys. Chem. C 114 (2010) 12610-12617.

[144] P. Sazama, L. Capek, H. Drobna, Z. Sobalik, J. Dedecek, K. Arve, and B. Wichterlova, Enhancement of decane-SCR-NOx over Ag/alumina by hydrogen. Reaction kinetics and in situ FTIR and UV-vis study, J. Catal. 232 (2005) 302-317.

[145] Y. Kim and K Seff, Structure of a very small piece of silver metal. The octahedral silver (Ag6) molecule. Two crystal structures of partially decomposed vacuum-dehydrated fully silver(1+) ion-exchanged zeolite A, J. Am. Chem. Soc. 99 (1977) 7055-7057; Y. Kim, and K Seff, The octahedral hexasilver molecule. Seven crystal structures of variously vacuum-dehydrated fully silver(1+)-exchanged zeolite A, J. Am. Chem. Soc. 100 (1978) 6989-6997.

[146] T. Sun and K. Seff, Silver Clusters and Chemistry in Zeolites, Chem. Rev. 94 (1994) 857–870.

[147] Y. Tao, Y. Lin, Z. Huang, J. Ren, and X. Qu, DNA-templated silver nanoclustersgraphene oxide nanohybrid materials: a platform for label-free and sensitive fluorescence turn-on detection of multiple nucleic acid targets, Analyst 137 (2012) 2588-2592, and references therein.

[148] S.S.R. Oemrawsingh, N. Markešević, E.G. Gwinn, E.R. Eliel, and D. Bouwmeester, Spectral Properties of Individual DNA-Hosted Silver Nanoclusters at Low Temperatures, J. Phys. Chem. C 116 (2012) 25568-25575.

[149] S.W. Yang and T. Vosch, Rapid Detection of MicroRNA by a Silver Nanocluster DNA Probe, Anal. Chem. 83 (2011) 6935-6939.

[150] Guo, W.; Yuan, J.; Dong, Q.; and Wang, E., Highly Sequence-Dependent Formation of Fluorescent Silver Nanoclusters in Hybridized DNA Duplexes for Single Nucleotide Mutation Identification, J. Am. Chem. Soc. 132 (2009) 932-934.

[151] Pal, S.; Tak, Y.-K.; and Song, J. M., Does the Antibacterial Activity of Silver Nanoparticles Depend on the Shape of the Nanoparticle? A Study of the Gram-Negative Bacterium Escherichia coli., Appl. Environ. Microbiol. 73 (2007) 1712-1720.

[152] Yan, S.-Y.; Zhang, W.; Zhao, Z.-X.; Lu, W.-C.; Zhang, H.-X., Geometries and stabilities of Ag_n^v ($v = \pm 1$, 0; n = 21-29) clusters, Theoret. Chem. Acc. 131(3) (2012) 1200 (8 pages).

[153] Huda, N.; Ray, A. K.; Electronic structures and magic numbers of small silver clusters: A many-body perturbation-theoretic study, Phys. Rev. A 67 (2003)

013201 (13 pages); N. Huda and A. K. Ray, A correlation study of small silver clusters, Eur. Phys. J. D 22 (2003) 217-227.

[154] J.P. Breen, R. Burch, C. Hardacre, C.J. Hill, Structural Investigation of the Promotional Effect of Hydrogen during the Selective Catalytic Reduction of NOx with Hydrocarbons over Ag/Al_2O_3 Catalysts. J. Phys. Chem. B 109 (2005) 4805-4807.

[155] Z. Zhang , R. C. Patel, R. Kothari , C. P. Johnson, and S. E. Friberg, Stable Silver Clusters and Nanoparticles Prepared in Polyacrylate and Inverse Micellar Solutions, J. Phys. Chem. B 104 (2000) 1176-1182

[156] A. S. Mazheika, T. Bredow, V. E. Matulis, and O. A. Ivashkevich, Theoretical Study of Adsorption of Ag Clusters on the Anatase $TiO_2(100)$ Surface, J. Phys. Chem. C 115 (2011) 17368-17377.

[157] G.A. Arteca, Molecular Shape Descriptors, Rev. Comp. Chem. 9 (1996) 191-253.

[158] V. Aquilanti, A. Lombardi and E. Yurtsever, Global view of classical clusters: the hyperspherical approach to structure and dynamics, Phys. Chem. Chem. Phys., 4 (2002) 5040-5051.

[159] M.-J. Huanga and J. D. Watts, Theoretical study of triatomic silver (Ag_3) and its ions with coupled-cluster methods and correlation-consistent basis sets, Phys. Chem. Chem. Phys. 14 (2012) 6849-6855.

[160] T.L. Haslett, K.A. Bosnick, and M. Moskovits, Ag_5 is a planar trapezoidal molecule, J. Chem. Phys. 108 (1998) 3453-3457.

[161] K.A. Bosnick, T.L. Haslett, S. Fedrigo, M. Moskovits, W.-T. Chan, and R. Fournier, Tricapped Tetrahedral Ag7: a Structural Determination by Resonance Raman Spectroscopy and Density Functional Theory, J. Chem. Phys. 111 (1999) 8867–8870.

[162] S.B.H. Bach, D.A. Garland, R.J. Van Zee, and W. Weltner, Ag_7 cluster: Pentagonal bipyramid, J. Chem. Phys. 87 (1987) 869-872.

[163] S. Lecoultre, A. Rydlo, J. Buttet, C. Félix, S. Gilb, and W. Harbich, Ultraviolet-visible absorption of small silver clusters in neon: Ag_n ($n = 1$–9) J. Chem. Phys. 134 (2011) 184504.

[164] C. Sieber, J. Buttet, W. Harbich, C. Félix, R. Mitrić, V. Bonačić-Kouteckỳ, Isomer-specific spectroscopy of metal clusters trapped in a matrix: Ag_9, Phys. Rev. A 70 (2004) 041201 (4 pages).

[165] J.C. Idrobo, S. Öğüt, K. Nemeth, J. Jellinek, and R. Ferrando, First-principles isomer-specific absorption spectra of Ag_{11}, Phys. Rev. B 75 (2007) 233411 (4 pages)

[166] J.I. Martínez and E.M. Fernández, Optical absorption spectra of Ag_{11} isomers: First-principles theoretical spectroscopy with time-dependent density functional theory, Eur. Phys. J. D 52 (2009) 199-202.

[167] S. Fredrigo, W. Harbich, J. Belyaev, and J. Buttet, Evidence for electronic shell structure of small silver clusters in the optical absorption spectra, Chem. Phys. Lett. 211 (1993) 166-170.

[168] F. Conus, V. Rodrigues, S. Lecoultre, A. Rydlo, and C. Félix, Matrix effects on the optical response of silver nanoclusters, J. Chem. Phys. 125 (2006) 024511 (4 pages).

[169] J. Zhao, Y. Luo, and G. Wang, Tight-binding study of structural and electronic properties of silver clusters, Eur. Phys. J. D 14 (2001) 309-316.

[170] H. M. Lee, M. Ge, B. R. Sahu, P. Tarakeshwar, and K. S. Kim, Geometrical and Electronic Structures of Gold, Silver, and GoldSilver Binary Clusters: Origins of Ductility of Gold and GoldSilver Alloy Formation, J. Phys. Chem. B 107 (2003) 9994-10005.

[171] T. H. Dunning Jr. and P. J. Hay, in Modern Theoretical Chemistry, Ed. H. F. Schaefer III, Vol. 3 (Plenum, New York, 1976) 1-28; P. J. Hay and W. R. Wadt, Ab initio effective core potentials for molecular calculations - potentials for the transition-metal atoms Sc to Hg, J. Chem. Phys., 82 (1985) 270-83; P. J. Hay and W. R. Wadt, Ab initio effective core potentials for molecular calculations - potentials for K to Au including the outermost core orbitals, J. Chem. Phys. 82 (1985) 299-310; W. R. Wadt and P. J. Hay, Ab initio effective core potentials for molecular calculations - potentials for main group elements Na to Bi, J. Chem. Phys. 82 (1985) 284-98.

[172] Gaussian 03, Revision C.02, M. J. Frisch G. W. Trucks, H. B. Schlegel, G. E. Scuseria, M. A. Robb, J. R. Cheeseman, J. A. Montgomery, Jr., T. Vreven, K. N. Kudin, J. C. Burant, J. M. Millam, S. S. Iyengar, J. Tomasi, V. Barone, B. Mennucci, M. Cossi, G. Scalmani, N. Rega, G. A. Petersson, H. Nakatsuji, M. Hada, M. Ehara, K. Toyota, R. Fukuda, J. Hasegawa, M. Ishida, T. Nakajima, Y. Honda, O. Kitao, H. Nakai, M. Klene, X. Li, J. E. Knox, H. P. Hratchian, J. B. Cross, V. Bakken, C. Adamo, J. Jaramillo, R. Gomperts, R. E. Stratmann, O. Yazyev, A. J. Austin, R. Cammi, C. Pomelli, J. W. Ochterski, P. Y. Ayala, K. Morokuma, G. A. Voth, P. Salvador, J. J. Dannenberg, V. G. Zakrzewski, S. Dapprich, A. D. Daniels, M. C. Strain, O. Farkas, D. K. Malick, A. D. Rabuck, K. Raghavachari, J. B. Foresman, J. V. Ortiz, Q. Cui, A. G. Baboul, S. Clifford, J. Cioslowski, B. B. Stefanov, G. Liu, A. Liashenko, P. Piskorz, I. Komaromi, R. L. Martin, D. J. Fox, T. Keith, M. A. Al-Laham, C. Y. Peng, A. Nanayakkara, M. Challacombe, P. M. W. Gill, B. Johnson, W. Chen, M. W. Wong, C. Gonzalez, and J. A. Pople, Gaussian, Inc., Wallingford CT, 2004.

[173] H. Häkkinen and U. Landman, Gold clusters Au_N ($2 \leq N \leq 10$) and their anions, Phys. Rev. B 62 (2000) R2287.

[174] L. Cheng and J. Yang, New insight into electronic shells of metal clusters: Analogues of simple molecules, J. Chem. Phys. 2013,138.

[175] L. Lian, S. A. Mitchell, P. A. Hackett, and D. M. Rayner, Size dependence of mobility on the surface of metal clusters: Ammonia on Ag_{10} and Ag_{16}, J. Chem. Phys. 1996, 104, 5338-5344.

[176] Zhang, W.; Zhao, H.; Wang, L. The Simple Cubic Structure of Ruthenium Clusters. J. Phys. Chem. B. 2004,108(7), 2140-2147, 10.1021/jp035995x

[177] Hu, M, Chen, J. Y., Li, Z.Y.; Au, L; Hartland, G. V., Li, X. D., Marquez, M; Xia, Y. N. Gold nanostructures: engineering their plasmonic properties for biomedical applications, Chem Soc. Rev 2006, 35(11), 1084-1094, 10.1039/b517615h

[178] Khanna, S. N., Jena, P., Atomic clusters: Building blocks for a class of solids, Phys. Rev. B 1995, 51(19), 13705-13716, 10.1103/PhysRevB.51.13705

[179] Leuchtner, R. E., Harms, A. C., Castleman, A. W., Thermal Metal Cluster Anion Reactions: Behavior of Aluminum Clusters with Oxygen, J. Chem. Phys. 1989, 91, 2753-2754, 10.1063/1.456988

[180] Ashman, C., Khanna, S. N., Liu, F., Jena, P., Kaplan, T., Mostoller, M., Phys. Rev. B **55**, 15868(1997).

[181] Duque, F., Manãnes A., Molina L. M., Loȍpez M. J., Alonso J. A., Computer simulation of cluster assembling, Int. J. Quantum Chem. 2002, 86(2), 226-238, 10.1002/qua.1603

[182] Reber, A. C., Khanna, S. N., Castleman A. W. Jr., Superatom Compounds, Clusters, and Assemblies: Ultra Alkali Motifs and Architectures, J. Am. Chem. Soc. 2007, 129(33), 10189-10194, 10.1021/ja071647n

[183] Reis, C. L., Martins, J. L.,Pacheco, J. M., Stability analysis of a bulk material built from silicon cage clusters: A first-principles approach, Phys. Rev.

B-Condensed Matter and Material Physics 2007, 76(23), 233406 10.1103/PhysRevB.76.233406

[184] Heer, W. A., The physics of simple metal clusters: experimental aspects and simple models, Rev. Mod. Phys. 1984, 65, 611, 10.1103/RevModPhys.65.611

[185] Sen P, Aromaticity and Metal Clusters, ed P K Chattaraj (Boca Raton, FL: CRC Press, Taylor and Francis), p 137 .

[186] Krätschmer, W., Lamb, L.D., Fostiropoulos, K., Huffman, D. R., Solid C_{60}: a new form of carbon, Nature 1990, 347, 354-358, 10.1038/347354a0

[187] Pearson, R. G., The principle of maximum hardness, Acc. Chem. Res.1993, 26(5), 250-255, 10.1021/ar00029a004

[188] Saha, R., Pan, S., Chattaraj, P. K., Statistical significance of the maximum hardness principle applied to some selected chemical reactions, Molecules 2016, 21(11), 1477, 10.3390/molecules21111477

[189] Politzer, P., Murray, J. S., Macaveiu, L., The principle of maximum hardness and structural effects of nonbonded interactions in chloronitromethanes, J. Mol. Structure Theochem 2010, 943, 53-58, 10.1016/j.theochem.2009.10.012

[190] L. Vitos, A. V. Ruban, H. L. Skriver and J. Kollar, The surface energy of metals, Surf. Sci. 1998, 411, 186-202, and references therein.

[191] Medel, V. M., Reber, A. C., Chauhan, V., Sen, P., Köster A. M., Calaminici, P., Khanna, S. N., Nature of Valence Transition and Spin Moment in Ag_nV^+ Clusters, J.Am. Chem. Soc. 2014,136(23), 8229-8236, 10.1021/ja412064c

[192] Ekardt, W., Work function of small metal particles: Self-consistent spherical jellium-background model, Phys. Rev. B 1984, 29, 1558, 10.1103/PhysRevB.29.1558

[193] Li, J., Li, X., Zhai, H. J., Wang, L. S., Au_{20}: a tetrahedral cluster, Science, 2003, 299(5608), 864-867, 10.1126/science.1079879

[194] Bonacic-Koutecký, V., Fantucci, P., Koutecký, J., Quantum chemistry of small clusters of elements of groups Ia, Ib, and IIa: fundamental concepts, predictions, and interpretation of experiments, Chem. Rev. 1991, 91(50),1035-1108, 10.1021/cr00005a016

[195] Knickelbein, M. B., Reactions of transition metal clusters with small molecules, Annu. Rev. Phys. Chem. 1999, 50, 79-115, 10.1146/annurev.physchem.50.1.79

[196] Calvayrac, F., Reinhard, P. G., Suraud, E., Ullrich, C. A., Nonlinear electron dynamics in metal clusters", Phys. Rep. 2000, 337, 493-578, 10.1016/S0370-1573(00)00043-0

[197] Hu, H. S., Zhao, Y. F., Hammond, J. R., Bylaska, E. J., Apra, E., van Dam, H. J. J., Li, J., Govind, N., Kowalski, K., Theoretical studies of the global minima and polarizabilities of small lithium clusters", Chem. Phys. Lett. 2016, 644, 235-242, 10.1016/j.cplett.2015.11.049

[198] Fournier, R., Cheng, J. B. Y., Wong, A., Theoretical study of the structure of lithium clusters, J. Chem. Phys. 2003, 119, 9444, 10.1063/1.1615237

[199] Chandrakumar, K. R. S., Ghanty, T. K., Ghosh, S. K., Ab initio studies on the polarizability of lithium clusters: Some unusual results, International Journal of Quantam chemistry, 2005, 105(2),166-173, 10.1002/qua.20678

[200] Blanc, J, Bonačić-koutecký, V., Broyer, M., Chevaleyre, J., Dugourd, Ph., Koutecký, J., Scheuch, C., Wolf, J. P. , Wöste, L., Evolution of the electronic-structure of lithium clusters between 4 and 8 atoms, J Chem Phys 1992, 96(3), 1793-1809, 10.1063/1.462846

[201] Brito, B. G. A., Candido, L., Teixeira, R. J. N., Hai, G. -Q., Binding energies of small lithium clusters: A comparison of different theoretical calculations, Chem Phys Lett., 2014, 616, 212-216, 10.1016/j.cplett.2014.10.044

[202] Paranthaman, S., Hong, K., Kim, J., Kim, D. E., Kim, T. K., Density Functional Theory Assessment of Molecular Structures and Energies of Neutral and Anionic $Al_n(n = 2 - 10)$ Clusters, Journal of Phys Chem A 2013, 117(38), 9293-9303, 10.1021/jp4074398

[203] Das, S., Pal, S., Krishnamurty, S., Understanding the Site Selectivity in Small-Sized Neutral and Charged $Al_n(4 \leqslant n \leqslant 7)$ Clusters Using Density Functional Theory Based Reactivity Descriptors: A Validation Study on Water Molecule Adsorption, J Phys Chem A 2013, 177(36), 8691-8702, 10.1021/jp403109s

[204] Akola, J, Häkkinen, H, Manninen,M, Ionization potential of aluminum clusters, Phys. Rev. B 1998, 58(7), 3601-3604, 10.1103/PhysRevB.58.3601

[205] López-Estrada, O., Orgaz, E., Theoretical Study of the Spin Competition in Small-Sized Al Clusters, J Phys. Chem. A 2015, 119(49), 11941-11948, 10.1021/acs.jpca.5b09871

[206] Duanmu, K., Roberto-Neto, O., Machado, F. B. C., Hansen, J. A., Shen, J., Piecuch, P., Truhlar, D. G., "Geometries, Binding Energies, Ionization Potentials, and Electron Affinities of Metal Clusters: $Mg_n^{(0,+/-1)}, n = 1 - 7$", J Phys. Chem. C 2016,120(24), 13275-13286, 10.1021/acs.jpcc.6b03080

[207] Belyaev, S. N., Panteleev, S. V., Ignatov, S. K., Razuvaev, A. G., Structural, electronic, thermodynamic and spectral properties of $Mg_n(n = 2 - 31)$ clusters. A DFT study, Computational and Theoretical Chemistry 2016, 1079, 34-46 10.1016/j.comptc.2016.01.011

[208] Heidari, I., De, S., Ghazi, S. M., Goedecker, S., Kanhere, D. G., Growth and Structural Properties of $Mg_n(n = 10 - 56)$ Clusters: Density Functional Theory Study, J Phys. Chem. A 2011,115(44), 2307-12314, 10.1021/jp204442e

[209] Iwasa, T., Nakajima, A., Geometric, electronic, and optical properties of a boron-doped aluminum cluster of $B_2Al_21^-$: A density functional theory study, Chem. Phys. Lett. 2013, 582, 100-104, 10.1016/j.cplett.2013.07.034

[210] Ge, GẊ., Yan, H. X., Jing, Q, et al. Structures and properties of $Au_nSc_m(n + m = 6)$ clusters, Eur. Phys. Journal D, 2013, 67, 116, https://doi.org/10.1140/epjd/e2013-30544-5.

[211] Xie, H., Li, X., Zhao, L., Qin, Z., Wu, X., Tang, Z., and Xing, X., Photoelectron Imaging and Theoretical Calculations of Bimetallic Clusters: $AgCu^-$, $AgCu_2^-$, and Ag_2Cu^-", J. Phys. Chem. A 2012, 116(42), 10365-10370, 10.1021/jp307478x

[212] Zheng, B.X., Die, D., Zhu, B, Zhao, Z.Q., Probing the structural, electronic and magnetic properties of small Au_4M, (M = Sc - Zn) clusters, Molecular Physics 2015, 113(22), 3395-3402, 10.1080/00268976.2015.1026294

[213] Zhang, J., Li, X., The geometric and spectroscopic features of (CuSe)(n=2-8) binary nanoclusters: a theoretical study", J Nanopart res, 2018, 20(11), 292, 10.1007/s11051-018-4404-2

[214] Loukhovitski, B.I., Sharipov, A.S., Starik, A.M., Quantum chemical study of small Al_nB_m clusters: Structure and physical properties", Chem Phys 2017, 493, 61-76, 10.1016/j.chemphys.2017.06.006

[215] Bansal, A, Sekhon, J.S., Verma, S.S., Dimensional and compositional dependent analysis of plasmonic bimetallic nanorods, J Modern optics 2015, 62(19),1665-1673, 10.1080/09500340.2015.1063725

[216] Bhatia, P, Verma, S. S., Sinha, M. M., Tuning the optical properties of Fe-Au core-shell nanoparticles with spherical and spheroidal nanostructures, Phys. Lett. A 2019, 383(21), 2542-2550, 10.1016/j.physleta.2019.05.009

[217] Sikorska, C., Skurski, P; The saturation of the excess electron binding energy in $Al_nF_{3n+1}^-$ (n = 1-5) anions, Chem. Phys. Lett 2012, 536, 34-38, 10.1016/j.cplett.2012.03.089

[218] Yang, H., Li, Y., He, H-M, Yu, D; Wu, D, Li, Z. R, Hetero-binuclear superhalogen anions with cyanide and/or isocyanide as ligands, Chem. Phys. Lett. 2018, 713, 203-209, 10.1016/j.cplett.2018.10.039

[219] Düvel, A., Heitjans, P., Fedorov, P., Scholz, G., Cibin, G., Chadwick, A. V., Pickup, D. M., Ramos, S., Sayle, L. W. L., Sayle, E. K. L.; Sayle, T. X. T., SayleIs, D. C., Is Geometric Frustration-Induced Disorder a Recipe for High Ionic Conductivity?, J. Am. Chem. Soc. 2017, 139(16), 5842 - 5848, 10.1021/jacs.7b00502

[220] Fang, H, Jena, P, Sodium Superionic Conductors Based on Clusters, ACS Appl. Mater. Interfaces 2019, 11(1), 963-972, 10.1021/acsami.8b19003

[221] Wilcoxon, J. P., Provencio, P. P., Heterogeneous Growth of Metal Clusters from Solutions of Seed Nanoparticles, J Am Chem Soc. 2004, 126(20), 6402-6408, 10.1021/ja031622y

[222] Hodak, J. H., Henglein, A., Giersig, M., Hartland, G. V., Laser-Induced Inter-Diffusion in AuAg Core-Shell Nanoparticles, J Phys. Chem. B 2000,104, 11708-11718, 10.1021/jp002438r.

[223] Lackner, F, Schiffmann, A, Lasserus, M , Messner, R (Messner, Roman), Schnedlitz, M , Fitzek, H, Polt, P , Knez, D, Kothleitner, G, Ernst, W.E.,

Helium nanodroplet assisted synthesis of bimetallic Ag@Au nanoparticles with tunable localized surface plasmon resonance, European Phys. JD 2019, 73(5), 104, 10.1140/epjd/e2019-90696-8

[224] Norsyuhada, W, Shukri, W. M; Bidin, Noriah, Islam, Shumaila, Krishnan, Ganesan, Synthesis of Au-Ag Alloy Nanoparticles in Deionized Water by Pulsed Laser Ablation Technique, J. Nanoscience and Nanotechnology 2018, 18(7), 4841-4851, 10.1166/jnn.2018.15358

[225] Hay, P. J., Wadt, W. R., Ab initio effective core potentials for molecular calculations, potentials for the transition-metal atoms Sc to Hg, J. Chem. Phys. 1985, 82, 270, 10.1063/1.448799

[226] Wadt, W. R., Hay, P. J., Ab initio effective core potentials for molecular calculations, potentials for main group elements Na to Bi, J. Chem. Phys. 1985, 82, 284, 10.1063/1.448800

[227] Xing, X., Wang, J., Kuang X., Xia, X., Lu, C., Maroulis, G., Probing the low-energy structures of aluminum magnesium alloy clusters: A detailed study, Phys. Chem. 2016, 18, 26177-26183, 10.1039/C6CP05571K

[228] Sun, Y., Fournier, R., Zhang, M., Structural and electronic properties of 13-atom 4d transition-metal clusters, Phys. Rev. A 2009, 79(4), 043202, 10.1103/PhysRevA.79.043202

[229] Li, J., Li, X., Zhai, H. J., Wang, L. S., $Au20$: a tetrahedral cluster, Science 2003, 299(5608), 864-7, 10.1126/science.1079879

[230] Bernardo, E.; Colombo, P.; Pippel, E.; Woltersdorf, J., Novel mullite synthesis based on alumina nanoparticles and a preceramic polymer, J. Am. Ceram. Soc., 89, (2006), 1577-1583

[231] Kim, J. -H.; Yoo, S.-J.; Kwak, D.-H.; Jung, H.-J.; Kim, T.-Y.; Park, K.-H.; Lee, J.-W., Characterization and application of electrospun alumina nanofibers, Nanoscale Res. Lett. 2014 9 (1), 44, 10.1186/1556-276X-9-44

[232] Mukherjee, A.; Sadiq, I. M.; Prathna, T.C.; Chandrasekaran, N., Antimicrobial activity of aluminium oxide nanoparticles for potential clinical applications, Science against microbial pathogens: communicating current research and technological advances.2011;1:245-51

[233] Kresse, G.; Schmid, M.; Napetschnig, E.; Shishkin, M.; Klhler, L.; Varga, P.; Science 2005, 308, 1440 -1442.

[234] Brown, G. E. Jr.; Henrich, V. E. ; Casey, W. H.; Clark, D. L. ; Eggleston, C.; Felmy, A. ; Goodman, D. W.; GrMtzel, M.; Maciel, G. ; McCarthy, M. I.; Nealson, K. H.; Sverjensky, D. A.; Toney, M.F. ; Zachara, J. M., Chem. Rev. 1999, 99, 77 -174.

[235] Magg, N.; Giorgi, J. B.; Schroeder, T.; Bmumer, M. ; Freund, H.-J.; J. Phys. Chem. B 2002, 106, 8756 - 8761.

[236] Posch, T.; Kerschbaum, F.; Mutschke, H.; Fabian, D.; Dorschner, J.; Horn, J; Astron. Astrophys. 1999, 352, 609 - 618.

[237] Dill, K. M. ; R. A. Reed, R. A. ; Calia, V. S.; Schulz, R. J., Propul. Power 1990, 6, 668 - 671; b) Turco, R. P.; Toon, O. B.; R. C. Whitten, R. C. ; Cicerone, R. J., Nature 1982, 298, 830 - 832.

[238] Gu, Y. B.; Xu, N.; Lin, M.; Tan, K., Structures, stabilities and properties of hollow $(Al_2O_3)_n$ clusters ($n = 10, 12, 16, 18, 24 and 33$): Studied with density functional theory, Computational and Theoretical Chemistry, 1063, (2015), 29-34, 10.1016/j.comptc.2015.03.027

[239] R. Li, L.J. Cheng, Structural determination of $(Al_2O_3)_n$, $(n = 1 - 7)$ clusters based on density functional calculation, Comp. Theor. Chem. 996 (2012) 125-131

[240] Gobrechta, D.; Decina, L.; Cristallo, S.; Bromley, S. T., A global optimisation study of the low-lying isomers of the alumina octomer $(Al_2O_3)_8$, Chemical Physics Letters, 711, (2018), 138-147, 10.1016/j.cplett.2018.09.018

[241] A.B. Rahane, M.D. Deshpande, V. Kumar, Structural and electronic properties of $(Al_2O_3)_n$ clusters with $n = 1 - 10$ from first principles calculations, J. Phys. Chem.C 115 (2011) 18111-18121.

[242] Zhang, Q.Y.; Cheng, L. J., Structural Determination of $(Al_2O_3)n$ $(n = 1 - 15)$ clusters Based on Graphic Processing Unit, J. Chem. Inf. Model., 2015, 55, 5,1012-1020 10.1021/acs.jcim.5b00069

[243] Sharipov, A.S.; Loukhovitski, B. I.; Starik, A. M., Theoretical study of structure and physical properties of $(Al_2O_3)_n$ clusters, Phys. Scr. 88, (2013), 058307, 10.1088/0031-8949/88/05/058307

[244] Woodley, S. M., Atomistic and electronic structure of $(X_2O_3)_n$ nanoclusters, n = 1-5, X = B, Al, In, Ga and Tl, Proc. R. Soc. A 467 (2011) 2020-2042.

[245] Karasev, V.V. ; Onischuk, A.A.; Glotov, O.G.; Baklanov, A.M.; Maryasov, A.G.; . Zarko, V.E; Panfilov, V.N.; Levykin, A.I.; Sabelfeld, K.K., Formation of charged aggregates of Al_2O_3 nanoparticles by combustion of aluminum droplets in air, Combust. Flame 138 (2004) 40-54.

[246] Zhong, M. M.; Kuang, X. -Y; Wang, H. -Q; Li, H. -F; Zhao, Y, -R Density functional study of the structural and electronic properties of tetra-aluminum oxide $Al_4O_n^{\lambda}$, $(3 \leq n \leq 8, \lambda = 0, -1)$ clusters Molecular Physics 2011, 109(4), 603-612 10.1080/00268976.2010.542777

[247] Fernandez, E. M.; Balbas, L. C.; Borstel, G.; Soler, J. M., Study of $(Al_2O_3)_n(O_x)$ clusters with $n \leq 16$ and $x = 0, 1, 2$ from first principles calculations, Thin Solid Films 2003, 428, 206.

[248] Fernandez, E. M.; Borstel, G.; Soler, J. M.; Balbas, L. C. Euro. Phys. J. D 2003, 24, 245

[249] Santambrogio, G.; Janssens, E.; Li, S.; Siebert, T.; Meijer, G.; Asmis, K. R.; Dobler, J.; Sierka, M.; Sauer, J. J. Am. Chem. Soc. 2008, 130, 15143.

[250] Linnolahti, M.; Pakkanen, T. A. Inorg. Chem. 2004, 43, 1184.

[251] Peng, Y.; Jian-Hua, G.; Zhen-Yi, J. Chin. Phys. 2007, 16, 1014

[252] Sierka, M.; Dobler, J.; Sauer, J.; Santambrogio, G.; Brummer, M.; Woste, L.; Janssens, E.; Meijer, G.; Asmis, K. R., Angew. Chem., Int. Ed. 2007, 46, 3372.

[253] Sierka, M.; Dobler, J.; Sauer, J.; Zhai, H.-J.; Wang, L.-S. Chem. Phys. Chem. 2009, 10, 2410.

[254] Desai, S. R.; Wu, H.; Rohlfing, C. M.; Wang, L.-S., A study of the structure and bonding of small aluminum oxide clusters by photoelectron spectroscopy: $Al_xO_y^-$, $(x = 1 - 2, y = 1 - 5)$ J. Chem. Phys. 1997, 106, 1309.

[255] Meloni, G.; Ferguson, M. J.; Neumark, D. M., Negative ion photodetachment spectroscopy of the Al_3O_2 , Al_3O_3 , Al_4O_x , $Al_5O_x(x = 3-5)$, Al_6O_5 , and Al_7O_5 clusters, Phys. Chem. Chem. Phys. 2003, 5, 4073-4079, 10.1039/b308119b

[256] Johnson, G. E.; Tyo, E. C.; Castleman, A. W. J. Phys. Chem. A 2008, 112, 4732.

[257] Ying, J. Y.; Benziger, J. B.; Gleiter, H. Phys. Rev. B 1993, 48, 1830.

[258] Wu, H.; Li, X.; Wang, X. B.; Ding, C. F.; and Wang, L. S., J. Chem. Phys. 1998, 109, 449

[259] Rozhanskii, I. L.; Chertikhin, G. V.; Serebrennikov, L. V.; Shevel'kov, V. F., J. Phys. Chem. 1988, 62, 1215

[260] Andrews, L.; Burkholder, T. R. ; Yustein, J. T., J. Phys. Chem. 1992, 96, 10182.

[261] Nemukhin, A. V.; Weinhold, F., Structures of aluminum oxide studied by ab initio methods with natural bond orbital analysis, J. Chem. Phys. 97, 1992, 3420, 10.1063/1.462978

[262] Archibong, E. F.; St-Amant, A., J. Phys. Chem. A 1999,103, 1109

[263] Archibong, E. F.; Seeburrun, N.; Ramasami, P., Geometric and electronic structure of AlO_4 and AlO_4^-, Chem. Phys. Lett. 481 2009, (4-6), 169-172

[264] Gowtham, S.; Lau, K. C.; Deshpande, M.; Pandey, R.; Gianotto, A. K.; Groenewold, G. S.; Structure, Energetics, Electronic, and Hydration Properties of Neutral and Anionic Al_3O_6, Al_3O_7, and Al_3O_8 Clusters J. Phys. Chem. A 2004, 108, 5081-5090

[265] Patzera, A. B. C.; Chang, Ch.; Sedlmayr, E. ; D. Sülzle, A density functional study of small $Al_xO_y(x, y = 1 - 4)$ clusters and their thermodynamic properties, Eur. Phys. J. D, 32, 329-337 (2005) DOI: 10.1140/epjd/e2005-00026-8

[266] Nemukhin, A. V.,; Weinhold, F., Structures of the aluminum oxides studied by ab initio methods with natural bond orbital analysis, J. Chem. Phys. 97 1992, 3420, 10.1063/1.462978.

[267] Solornonik, V. G.; and Sliznev, V. V.; Russ. J. Inorg. Chern. 32, 788 (1987)

[268] Sonchik, S. M. ; Andrews, L.; Carlson, K. D., J. Phys. Chem. 1983, 87, 2004

[269] Kohn, W.; Sham, L. J., Phys. Rev. A 1965,140, 1133

[270] Dekock, R. L.; and Barbachyn, M. R., J. Inorg. Nucl. Chem. 1981, 43, 2645

[271] Zaitsevskii, A. V.; Chertikhin, G. V.; Serebrennikov, L. V.; and Stepanov, N. F.; J. Mol. Struct. (Theochem)1993, 280, 291

[272] Sarker, M.B.M; Kim, C-S; Choi, C. H., Ground and excited states of Al_2O_2 and its anion. Chem Phys Lett 2005, 411, 297- 301

[273] Piecuch, P.; Kucharski, S.A.; Kowalski, K.; Musial, M., Efficient computer implementation of the renormalized coupled-cluster methods: The R-CCSD(T), R-CCSD(T), CR-CCSD[T], and CR-CCSD(T) approaches Computer Phys. Commun. 2002, 149, 71-96, 10.1016/S0010-4655(02)00598-2

[274] Nemukhin, A.V., On the structure of the AlO_2 dimer, Al_2O_4, J. Molecular structure: Theochem 1994 315, 225-227

[275] Ho, P.; Burns, R.P., A mass spectrometric study of the AlO_2 molecule, High Temp. Sci., 1980, 12, 31.

[276] Holmes, D. L., Elements of Physical Geology; Ronald Press: New York, 1969

[277] Desurvire, E.; Phys. Today, 1994, 47, 20.

[278] Morey, G. W., The properties of Glass, 2nd ed.; Reinhold: New York, 1954

[279] Wang, N.; Tang, Y. H.; Zhang, Y. F.; Lee, C. S.; Lee, S. T., Phys. Rev. B, 1998, 58, R16024

[280] Keiichiro, H.; and Makoto, K.; and Toyonobu, Y., High throughput production of nanocomposite SiO_x powders by plasma spray physical vapor deposition for

negative electrode of lithium ion batteries, Science and Technology of Advanced Materials, 2014, 15(2), 025006, 10.1088/1468-6996/15/2/025006

[281] Anderson, J. S.; Ogden, J. S., Matrix Isolation Studies of Group-IV Oxides. I. Infrared Spectra and Structures of SiO, Si_2O_2, and Si_3O_3, J. Chem. Phys. 1969, 51, 4189. 10.1063/1.1671778

[282] Wang, L.S.; Nicholas, J.B.; Dupuis, M.; Wu, H,; Colson, S. D., $Si_3O_y(y = 1-6)$ clusters: Models for oxidation of silicon surfaces and defect sites in bulk oxide materials, Phys. Rev. Lett. 1997, 78(23), 4450-4453.

[283] Wang, L. S.; Wu, H. B.; Desai, S. R.; Small silicon oxide clusters: Chains and rings Conference: 8th International Symposium on Small Particles and Inorganic Clusters (ISSPIC 8), Zeitschrift fur physik d-atoms molecules and clusters 1997, 40(1-4), 36-39

[284] Wang, L.-S; Wu, H.; Desai, H. R.; Fan, J.; Colson, S. D.; A Photoelectron Spectroscopic Study of Small Silicon Oxide Clusters: SiO_2, Si_2O_3 and Si_2O_4, J. Phys. Chem. 1996, 100, 8697

[285] Iraqi, M.; Goldberg, N; Schwarz, H, Neutralization-reionization mass spectrometry experiments confirm the predicted existence of cyclic silicon oxide (Si2O) and silicon nitride (Si2N) cluster molecules J. Phys. Chem., 1993, 97(44), 11371-11372, 10.1021/j100146a004

[286] Laser ablation of silica: Study of induced clusters by Fourier transform ion cyclotron resonance mass spectrometry Lafargue, P. E.; Gaumet, J. J.; Muller, J. F.; Journal of mass spectrometry, 31 (6) , 623-632, 1996

[287] Dzhemilev, N. Kh.; Kovalenko, S. F.; Maksimov, S. E.; Tukfatullin, O. F.; Khozhiev, Sh. T., Study of the Formation and Unimolecular Fragmentation of Clusters under Ion Bombardment, J. Synch. Investig. (2017), 11(3), 490-495, 10.1134/S1027451017010074

[288] Chu, T.S.; Zhang, R.Q.; Cheung, H.F., Geometric and electronic structures of silicon oxide clusters, J. Phys. Chem B, 2001, 105(9), 1705-1709.

[289] Huang, L.; Lambrakos, S. G.; Massa, L, Stable structures and absorption spectra for Si_xO_y molecular clusters using density functional theory Structural Chem, 2017, 28(5),1573-1580

[290] Petrov, A. V.; Murin, I. V.; Ivanov-Schitz, A. K., Geometry and electronic structure of $(SiO_2)_3$ clusters, Russian Journal of general chemistry, 2017, 87(7),1456-1460

[291] Bandyopadhyay, I.; Aikens, C. M.; Structure and Stability of $(TiO_2)_(n)$, $(SiO_2)_(n)$, and Mixed $Ti_mSi_{n-m}O_{2n}$ $[n = 2-5, m = 1to(n-1)]$ Clusters J. Phys. Chem. A , 2011115(5), 868-879, 2011 Hu, S. -X; Yu, J.-G.; Zeng, E. Y., A Density Functional Study of the Structural and Electronic Properties of Silicon Monoxide Clusters, J. Phys Chem A 2010, 114(40), 10769-10774

[292] Tiznado, W; Ona, O. B.; Caputo, M. C.; Theoretical Study of the Structure and Electronic Properties of $Si_3O_n^-$ and $Si_6O_n^-$ $(n = 1 - 6)$ Clusters. Fragmentation and Formation Patterns J. Chem theory and computation 2009, 5(9), 2265-2273

[293] Zhang, Y.; Chen, X. -F.; Qi, K.-T; Density functional theory study of silica clusters $(SiO_2)_(n)^(-)$ $(n <= 7)$ Acta Physica Sinica 2010, 59(7), 4598-4601

[294] Zhang, R. Q.; Chu, T. S.; Cheung, H. F.; Wang , N.; Lee, S. T. , High reactivity of silicon suboxide clusters, Phys. Rev. B, 2001, 64, 113304

[295] Wang, L.S.; Nicholas, J.B.; Dupuis, M.; Wu, H,; Colson, S. D., $Si_3O_y(y = 1-6)$ clusters: Models for oxidation of silicon surfaces and defect sites in bulk oxide materials, Phys. Rev. Lett. 1997, 78(23), 4450-4453.

[296] Creasy, W. R.; O'Keefe, A.; McDonald, J. R., J Phys. Chem. 1987, 91, 2848.

[297] Bergeron, D. E.; Castleman, A. W., Jr. Insights into the stability of silicon cluster ions: Reactive etching with O_2 J. Chem. Phys. 2002, 117, 3219. 10.1063/1.1486439

[298] J.A.W Harkless, D.K. Stillinger, F.H. Stillinger, Structures and Energies of SiO_2 Clusters, J. Phys. Chem. 1996, 100, 1098.

[299] T.S Chu, R.Q. Zhang, H.F. Cheung, J. Phys. Chem. B 105(2001) 1705

[300] Chelikowsky, J. R., Structural and electronic properties of neutral and charged silica like clusters, Phys. Rev. B, 1998, 57, 3333, 10.1103/PhysRevB.57.3333

[301] Nayak, S. K., Rao B. K., Khanna, S. N.; Jena, P. Atomic and electronic structure of neutral and charged Si_nO_m clusters, J Chem Phys, 109(4), 1998, 1245-1250, 10.1063/1.476675

[302] Zang, Q. J.; Su, Z. M.; Lu, W. C.; Wang, C. Z.; and Ho, K. M., Oxidation pattern of small silicon oxide clusters: structures and stability of $Si_6O_n(n = 1 - 12)$, J. Phys. Chem. A 2006, 110, 8151-8157.

[303] Lu, W. C.; Wang, C. Z.; Nguyen, V. Schmidt, M. W.; Gordon, M. S.; Ho, K. M, Structures and Fragmentations of small silicon oxide clusters by ab initio calculations, J. Phys. Chem. A, 2003, 107, 6936-6943

[304] Bromley, S. T.; Zwijnenburg, M. A.; Maschmeyer, Fully Coordinated Silica $(SiO_2)_N$ Nanoclusters: Molecular Rings, Th. Phys. Rev. Lett. 2003, 90, 035502

[305] Bromley S. T.; Flikkema, E., Columnar-to-Disk Structural Transition in Nanoscale $(SiO_2)_N$ Clusters, Phys. Rev. Lett. 2005, 95, 185505, PhysRevLett.95.185505

[306] Zhang, R. Q.; Zhao, M. W.; Lee, S. T., Silicon Monoxide Clusters: The Favorable Precursors for Forming Silicon Nanostructures, Phys. Rev. Lett. 2004, 93, 095503, 10.1103/PhysRevLett.93.095503

[307] Byun, H. -G.; Kim, I.; Kwon, H. -S.; Bae, G. -T., Comparisons of the Functional and Basis Set Combinations for Silicon Oxide Clusters: A Density Functional Theory Study, Bulletin of the Korean Chemical Society, 2017, 38(11), 1310-1315 10.1002/bkcs.11288

[308] Bae, G. T.; Dellinger, B.; Hall, R. W.; Density functional calculation of the structure and electronic properties of $Cu_nO_n, (n = 1 - 8)$ clusters, J Phys Chem A., 2011, 115(11), 2087-2095, 10.1021/jp104177q.

[309] Isoya, J.; Weil, J.A.; Halliburton, L. E, J. Chem Phys. 1981, 74, 5436.

[310] Wang, L.-S; Wu, H.; Desai, H. R.; Fan, J.; Colson, S. D.; A Photoelectron Spectroscopic Study of Small Silicon Oxide Clusters: SiO_2, Si_2O_3 and Si_2O_4, J. Phys. Chem. 1996, 100, 8697

[311] Schmidt, M. W.; Baldridge, K. K.; Boatz, J. A.; Elbert, S. T.; Gordon, M. S.; Jensen, J. H.; Koseki, S.; Matsunaga, N.; Nguyen, K. A.; Su, S. J.; Windus, T. L.; Dupuis, M.; Montgomery, J. A. General atomic and molecular electronic structure system, J. Comput. Chem. 1993, 14, 1347.

[312] Boldyrev, A. I.; Simons, J. Ab initio study of the silicon oxide (Si_2O and Si_3O) molecules, J Chem. Phys. Chem. 1993, 97, 5875

[313] Nakagawa, H.; Asano, M.; Kubo, K., Mass spectrometric study of the vaporization of lithium metasilicate, J. Nucl. Mater., 1981, 102, 292

[314] Fan, J.; Nicholas, J. B.; Price, J. M.; Colson, S. D.; Wang, L. S., $Si_3O_4^-$: vibrationally resolved photoelectron spectrum and ab initio calculations J. Am. Chem. Soc., 1995, 117(19), 5417-5418, 10.1021/ja00124a048

[315] Kresse; G., Hafner; J. Phys. Rev. B 47, 558 (1993).

[316] Kresse; G., Furthmüller, J. Comput. Mater. Sci. 6(15), 1996

[317] Blöchl; P. E. Phys. Rev. B 50, 17953 (1994).

[318] Fabio Finocchi and Claudine Noguera, *Structure and bonding of small stoichiometric lithium oxide clusters*, Physical Review B, Volume 53, number 8,(1996)

[319] Yuan Yuan and Longjiu Cheng, *Theoretical Prediction for the Structures of Gas Phase Lithium Oxide Clusters: $(Li_2O)_n$ (n=1-8)* , International Journal of Quantam Chemistry, 2013, 113, 1264-1271

[320] Prinka Batra, Ritu Gaba, Upasana Issar,Rita Kakkar, *Structures and Stabilities of Alkaline Earth Metal Oxide Nanoclusters: A DFT Study*, Research article, Journal of theoretical chemistry, July 2013

[321] Mingyang Chen, Andrew R. Felmy, and David A. Dixon, *Structures and Stabilities of $(MgO)_n$ Nanoclusters*, Phys. Chem. A, 2014, 118 (17), pp 3136-3146

[322] Recio, J. M.;Pandey, R.; Ayuela, A.; A. B. Kunz, A. B.; Molecular orbital calculations on $(MgO)_n$ and $(MgO)_n^+$ clusters, (n = 1-13), J. Chem. Phys.,98(6), 4783-4792, (1993)

[323] Recio, J.M.; R. Pandey, R.; Ab initio study of neutral and ionized microclusters of MgO, Phy. Rev. A, 47(3), 2075- 2082, 1993.

[324] Huber, K. P.; Herzberg, G.; Molecular Spectra and Molecular Structure, IV. Constants of Diatomic Molecules, van Nostrand Reinhold, New York, NY, USA, 1979.

[325] J. Heyd, J. E. Peralta, and G. E. Scuseria, Energy band gaps and lattice parameters evaluated with the Heyd-Scuseria-Ernzerhof screened hybrid functional, J Chem Phys., 174101 (2005), 123(17), 10.1063/1.2085170

[326] Nemukhin, A. V.,; Weinhold, F., Structures of the aluminum oxides studied by ab initio methods with natural bond orbital analysis, J. Chem. Phys. 97, 3420 (1992), 10.1063/1.462978.

[327] Solornonik, V. G.; and Sliznev, V. V.; Russ. J. Inorg. Chern. 32, 788 (1987)

[328] Sharipov, A.S.; Loukhovitski, B. I.; Starik, A. M., Theoretical study of structure and physical properties of $(Al_2O_3)_n$ clusters, Phys. Scr. 88, (2013), 058307, 10.1088/0031-8949/88/05/058307

[329] Malliavin, M.-J.; Coudray, C., An initio calculations on $(MgO)_n$, $(CaO)_n$, and $(NaCl)_n$ clusters $(n = 1 - 6)$, J. Chem. Phys., 1997, 106(6), 2323, 10.1063/1.474110

[330] Xu, X. L.; Yang, B.; Wei, Z. -Y; Cao, G. -J; Xu, H. -G.; Zheng; W. J; Structural and bonding properties of Cu_3O_3 and Cu_3O_4 clusters: anion photoelectron spectroscopy and density functional calculations, Phys. Chem. Chem. Phys., 2018, 20(31), 20622, 10.1039/c8cp03302a

[331] Wang, L.S.; Wu, H.B.; Desai, S.R.; Lou, L. Electronic structure of small copper oxide clusters: From Cu_2O to Cu_2O_4. Physical Review B. 1996, 53(12), 8028-8031.

[332] Dai, B.; Tian, L.; Yang, J.L.; A theoretical study of small copper oxide clusters: $Cu_2O_x, x = 1 - 4$ J Chem. Physics, 2004,120(6), 2746-2751.

[333] Jadraque, M.; Martín, M.; DFT calculations of $Cu_nO_m^{0/+}$ clusters: Evidence for Cu_2O building blocks, Chemical Physics Lett ,2008,456, 51-54 10.1016/j.cplett.2008.02.114

[334] Al-Sunaidi, A. A; Sokol, A.A; Catlow, C. R. A; Woodley, S. M., Structures of Zinc Oxide Nanoclusters: As Found by Revolutionary Algorithm Techniques, J. Phys. Chem. C 2008, 112(48), 18860-18875, 10.1021/jp805983g

[335] Reber, A. C.;Khanna, S. N; Hunjan, J. S.; Beltran, M. R., Rings, towers, cages of ZnO, Eur. Phys. J. D, 2007, 43, 221-224, 10.1140/epjd/e2007-00087-7

[336] Matxain, J. M.; Fowler, J. E.; Ugalde, Electronic Excitation Energies of Zn_iO_i Clusters, J. Am. Chem. Soc., 2003, 125(31), 9494-9499,

10.1021/ja0264504

[337] Trushina, E. V; I. L. Zilberberga, I. L.; Bulgakov, A. V., Structure and Stability of Small Zinc Oxide Clusters, Physics of the Solid State, 2012, 54(4), 859-865, 10.1134/S1063783412040294

[338] Jain, A; Kumar, V; Kawazoe, Y; Ring structures of small ZnO clusters, Comput Mater Sci., 2006, 36(1-2), 258-262 10.1016/j.commatsci.2005.06.008

[339] Trushin, E. V.; Zilberberg, I., Anion-radical oxygen centers in small $(AgO)_n$ clusters: Density functional theory predictions, Chem. Phys. Lett., 2013, 560, 37-41. 10.1016/j.cplett.2012.12.059

[340] Klacar, S.; Hellman, A.; Panas, I.; Grönbeck, H., Oxidation of Small Silver Clusters: A Density Functional Theory Study, J. Phys. Chem. C, 2010, 114, 12610-12617

[341] Sharma, N.; Kakkar, R.; Recent advancements in warfare agents/metal oxides surface chemistry and their simulant studies, Advanced Materials Letters, 2013.

[342] Kapoor, P. N.; Bhagi, A. K.; Mulukutla, R. S.; and Klabunde, K. J., Dekker Encyclopedia of Nanoscience and Technology, Marcel Dekker, New York, NY, USA, 2004.

[343] John P. Perdew, Kieron Burke, and Matthias Ernzerhof, Generalized Gradient Approximation Made Simple, Phys. Rev. Lett. 78, 1396 (1997)